

Supercurrent Time Division Multiplexing with Solid-State Integrated Hybrid

Superconducting Electronics

Alessandro Paghi^{1*}, Laura Borgogino¹, Simone Tortorella^{1,2}, Giorgio De Simoni¹, Elia Strambini¹, Lucia Sorba¹, and Francesco Giazotto^{1*}

¹Istituto Nanoscienze-CNR and Scuola Normale Superiore, Piazza San Silvestro 12, 56127 Pisa, Italy.

²Dipartimento di Ingegneria Civile e Industriale, Università di Pisa, Largo Lucio Lazzarino, 56122 Pisa, Italy

*Corresponding authors: alessandro.paghi@nano.cnr.it, francesco.giazotto@sns.it

Keywords: Indium Arsenide (InAs); Josephson Field Effect Transistor (JoFET); Superconducting Switch; Superconducting Multiplexer; Hybrid Superconducting Electronics; III-V Heterostructures.

Abstract

Time-division multiplexing of cryogenic signals is a promising approach to reduce space requirements, shorten cooldown times, and increase the number of quantum devices measured per cooldown. We demonstrate time-division multiplexing of non-dissipative supercurrents using voltage-controlled hybrid superconducting demultiplexers. These chips integrate superconducting Josephson Field Effect Transistors including Al superconducting electrodes, proximitized semiconducting InAs channels, and hafnium oxide gate insulators. Each transistor fully suppresses the switching current and increases the resistance 20 times under a gate voltage of -4.5 V. A demultiplexer with one input and eight outputs showed a non-dissipative input range of $\pm 2 \mu\text{A}$, operates up to 100 MHz in signal frequency, and 100 kHz in switching frequency at 50 mK. It achieved near-zero insertion loss in the superconducting state and an $\frac{ON}{OFF}$ ratio of 17.5 dB. By optimizing the signal layout, the operation was extended up to 4 GHz using a demultiplexer with two outputs.

Introduction

In the past decades, there has been tremendous progress in the theoretical and experimental development of a wide range of quantum devices operating at cryogenic temperatures, where phase transitions, reduced thermal noise, and minimized interactions with the surrounding environment can be achieved. Superconducting¹⁻³ and spin qubits^{2,4,5}, parametric amplifiers⁶⁻⁹, diodes¹⁰⁻¹², and single photon detectors¹³⁻¹⁵, are only few examples of the devices proposed and manufactured. Along the same side, cryogenic temperatures are mandatory to study hot topics in quantum physics, such as spin-dependent supercurrent¹⁶, topological phase transitions¹⁷⁻¹⁹, superconductivity-quantum Hall effect interaction²⁰⁻²², and many-body electron systems²³⁻²⁵.

In a conventional cryostat, N signal lines come from (to) room temperature electronics and travel to (from) the low-temperature plates connecting to the N ports of the quantum device under test (QDUT) (Fig. 1a). Each signal line significantly impacts the cryostat's costs, space occupied, and temperature stability. Thus, the number of cables is a significant constraint in testing and using of very-large-scale-integrated (VLSI) quantum devices. For instance, one of the most advanced quantum machines, the quantum computer Google Sycamore, uses more than 200 RF coaxial cables to control only 54 qubits^{26,27}. To reduce the required space, minimize the cooldown time, and increase the number of measurable devices per cooldown, time division multiplexing (TDM) of signal lines is needed to route signals to the QDUT. In a TDM-cryostat, only one signal line reaches the lowest temperature plate to connect 2^N ports of the QPU using N control lines (Fig. 1b).

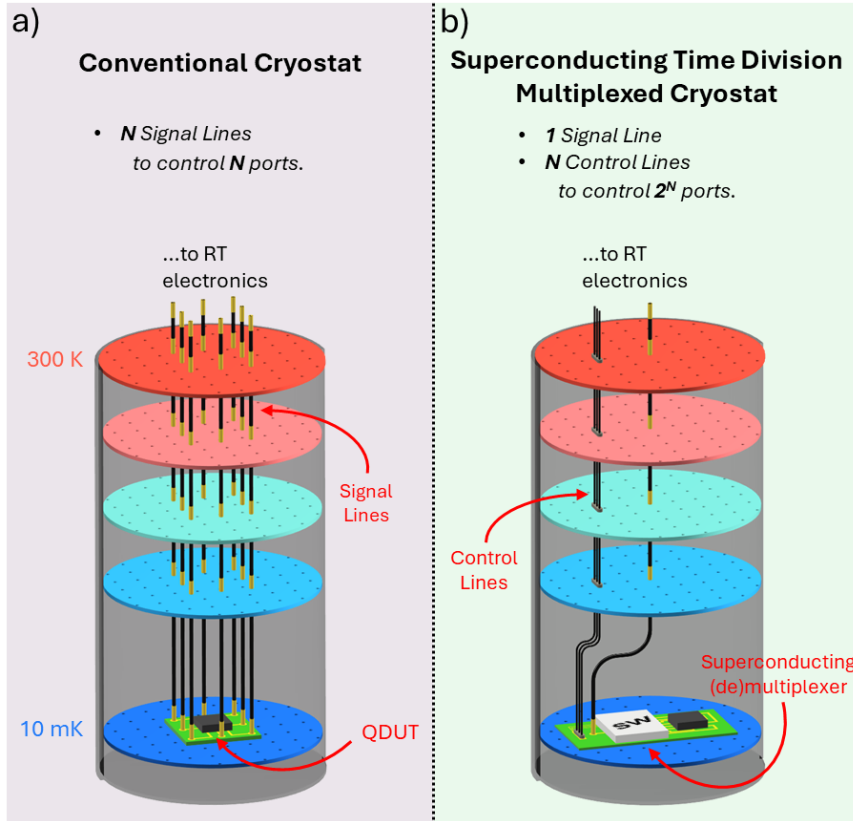


Fig. 1: Comparison between conventional and superconducting TDM cryostats. a) A conventional cryostat needs N signal lines to control N ports of the quantum device under test (QDUT). b) A superconducting TDM-cryostat features N control lines and one signal line to control 2^N ports of the QDUT. The schematic representations are intended to represent the input or the output lines of the QDUT.

Nowadays, electromechanical switches are usually involved in TDM of signals at cryogenic temperatures down to a few mK, with the drawbacks of a large amount of volume occupied ($\sim 100 \text{ cm}^3$), reduced I/O lines, and a high switching time ($\sim 10 \text{ ms}$)^{28,29,30}. Cryo-CMOS solid-state solutions offer the advantage of a reduced volume together with an increased number of I/O lines and faster-switching events ($\sim 1 \text{ ns}$), allowing at the same time to achieve line-to-line isolations of $30 \div 40 \text{ dB}$ s^{31,32,33,34}. On the other hand, static power dissipation accounts for the increase of the temperature of the cold plate of tens of mKs^{31,33}, while an insertion loss of $1 \div 3 \text{ dB}$ s is usual in the ON-state due to the Ohmic behavior of the chip^{33,34}. In quantum computing, it is noteworthy that the deployment of TDM using cryo-CMOS platforms remains incompatible with scalable, high-fidelity control of superconducting transmon qubits. This incompatibility arises from significant thermal radiation emitted by the multiplexer, necessitating the thermalization of signals between the demultiplexer's output and the quantum chip via a well-thermalized attenuator^{33,34}. Along with the previous solutions, more exotic TDM demonstrations are proposed using platforms based on SiGe-2DEG³⁵, GaAs-HEMTs^{36,37}, and InAsNWs³⁸. In this context, TDM with a superconducting solid-state multiplexer promises short downtimes between control switching events, near-to-0W static power dissipation,

negligible heat injection, and a minimized insertion loss. In recent years, few demonstrations of proof-of-concept superconducting switches have been documented³⁹⁻⁴¹. On the other hand, considerable insertion loss and static power required in the ON-state³⁹, reduced operating band^{40,41}, and a limited number of output ports (2 at maximum)³⁹⁻⁴¹, are the major drawbacks highlighted.

Hybrid superconductor-semiconductor architectures enable ideal platforms to develop Josephson Field Effect Transistors (JoFETs) for supercurrent multiplexing^{42,43,44,45,46}. The hybrid super-semi JoFET is the key to implementing a two-state ON/OFF superconducting/normal building block⁴⁷. The gate tunability of the critical current, as well as the gate tunability of the normal-state resistance, are the fundamental aspects involved in the supercurrent multiplexing operation. In the III-V compound group, InAs is the most common semiconductor employed in the manufacturing of JoFETs thanks to the optimal superconducting proximity effect^{42,43,44,48,49,50,51}, which provides the electron gas hosted by the InAs layer the ability to support a supercurrent. Among InAs-based platforms, we recently proposed InAs on Insulator (InAsOI) as a new convenient platform to develop planar hybrid superconducting electronics⁵²⁻⁵⁴. Unlike other InAs architectures, the InAsOI features a InAs epilayer grown onto a cryogenic electrical insulating InAlAs metamorphic buffer. The InAsOI allows the electrical decoupling of surface-exposed adjacent devices together with the capability of achieving the superconducting proximity effect with high critical current density integration. Irrespective of the fabrication methodology customary to GaAs-based heterostructures, the InAsOI epitomizes the counterpart of the silicon-on-insulator (SOI) architecture apt for superconducting technologies, wherein proximitized InAs and the cryogenic electrical insulating InAlAs substitute silicon and silicon oxide layers of SOI, respectively.

Here, we report on the TDM of non-dissipative supercurrents with voltage-actuated hybrid superconducting demultiplexers able to reduce the number of signal lines of a conventional cryostat. As ON-OFF building blocks, we developed InAsOI-based JoFETs featuring Al as superconductor and HfO₂ as gate insulator able to suppress the switching current entirely and to increase the normal-state resistance by 20 times with a gate voltage of -4.5 V. We proposed a superconducting demultiplexer with 1 input and 8 outputs operating at 50 mK up to 100 MHz in signal frequency and 100 kHz in switching frequency, featuring an insertion loss of ~ 0 dB in the superconducting state, and an $\frac{ON}{OFF}$ ratio of ~ 17.5 dB. The operational range of signal frequency was effectively broadened by designing a superconducting demultiplexer with a single input and dual outputs, incorporating an optimized microwave signal transport layout that concurrently mitigates the influence of parasitic electrical elements. The constructed device underwent validation at frequencies reaching up to 4 GHz at 50 mK, demonstrating an insertion loss of approximately 0 dB within the superconducting state

and exhibiting an $\frac{ON}{OFF}$ ratio of ~ 16 dB. The reciprocity of the circuits allows, in principle, reversed operations of the proposed devices as a multiplexer by inverting the I/O ports.

Results and Discussion

InAsOI-Based Josephson Field Effect Transistor Fabrication

The cross-section of a Josephson Field Effect Transistor (JoFET) fabricated on the InAs on Insulator (InAsOI) platform is shown in Fig. 2a.

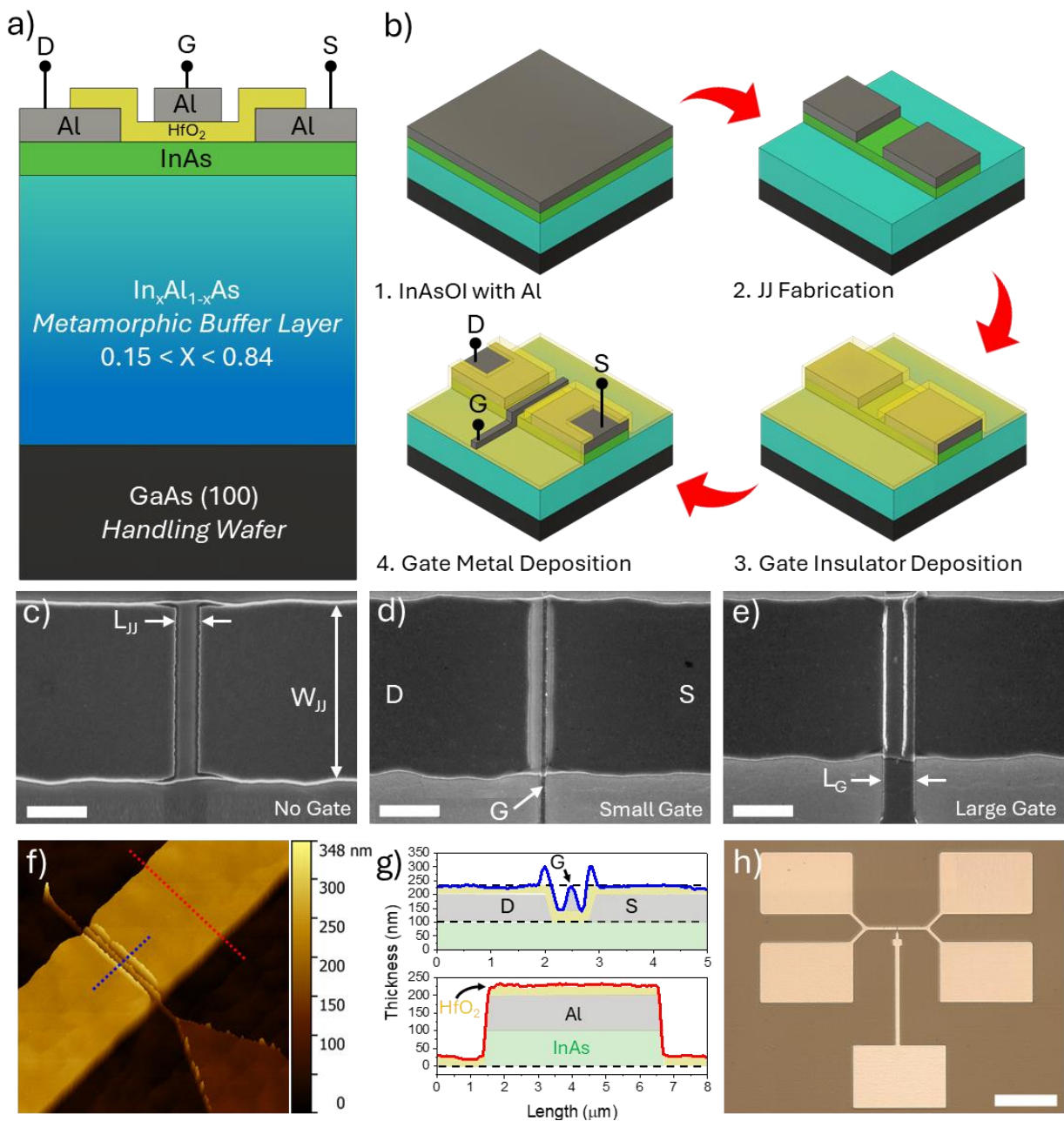


Fig. 2: Josephson Field Effect Transistors with InAsOI: concept, manufacturing process, and morphologic characterization. a) Cross-section structure of a JoFET with InAsOI. b) Fabrication process of a JoFET with InAsOI: 1. Superconductive Al deposition onto InAsOI; 2. JJ fabrication via

MESA and Al wet etching; 3. Gate insulator deposition via ALD; 4. Gate metal deposition. c,d,e) Top-view SEM images ($10k\times$) of JoFETs with $W_{JJ} = 6\ \mu\text{m}$ and $L_{JJ} = 800\ \text{nm}$ before gate fabrication (c), and after small ($L_G = 200\ \text{nm}$) (d) and large ($L_G = 1000\ \text{nm}$) (e) gate manufacturing; the scalebar is $2\ \mu\text{m}$. f) xy-plane tilted AFM z-profile of a JoFET featuring $W_{JJ} = 6\ \mu\text{m}$, $L_{JJ} = 1200\ \text{nm}$, and $L_G = 100\ \text{nm}$. g) AFM thickness profiles extrapolated from the red and blue dashed line in (f). h) Optical microscope image of the 4-terminal JoFET architecture. The scalebar is $100\ \mu\text{m}$.

The JoFET is built upon a Molecular Beam Epitaxy (MBE)-grown InAsOI stack consisting, from bottom to top, of a $500\text{-}\mu\text{m}$ -thick semi-insulating GaAs (001) substrate, a $\sim 1.5\text{-}\mu\text{m}$ -thick step-graded $\text{In}_x\text{Al}_{1-x}\text{As}$ metamorphic buffer with X increasing from 0.15 to 0.84, and a 100-nm -thick InAs semiconductive epilayer⁵². The InAs layer is n -type doped (extrinsically undoped) due to the InAs natural surface electron accumulation layer^{55,56} and deep energy donor levels in the InAlAs band gap⁵⁷. For the InAs epilayer, a sheet electron density (n_{2D}) of $1.35\times 10^{12}\ \text{cm}^{-2}$ and a mobility (μ_n) of $6.7\times 10^3\ \text{cm}^2/\text{Vs}$ were measured at 3K from Hall measurements. The InAlAs metamorphic buffer behaves as an insulator at cryogenic temperatures⁵². Fig. 2b depicts the fabrication process of the JoFET. A 100-nm -thick Al layer was deposited onto InAsOI, which acts as the superconductor of the JoFET (Fig. 2b.1). JoFETs were fabricated via aligned lithographic steps. First, Al and InAs MESA were defined by UV-lithography and manufactured by successive Al and InAs wet etching, setting the Josephson Junction (JJ) width (W_{JJ}) and exposing the InAlAs layer. Then, the JJ length (L_{JJ}) was defined by electron-beam-lithography and Al wet-etching, leaving the underneath InAs unaffected (Fig. 2b.2). A $\sim 30\text{-nm}$ -thick HfO_2 dielectric layer was conformably deposited via Atomic Layer Deposition (ALD) and used as the gate insulator (Fig. 2b.3)⁵⁸. The ALD was performed at an optimized temperature of $130^\circ\ \text{C}$ to preserve the Al/InAs superconducting and transport properties⁵⁹. Eventually, the metal gate was fabricated by electron-beam-lithography and tilted Ti/Al deposition (Fig. 2b.4), which allowed to conformably cover acute angles left by the InAs wet etching (Fig. S1). We realized superconductor-semiconductor-superconductor Al-InAs-Al JoFETs with W_{JJ} of $6\ \mu\text{m}$, L_{JJ} from 500 to $1250\ \text{nm}$, and gate lengths (L_G) from 100 to $1000\ \text{nm}$. Fig. 2c-e show Scanning Electron Microscopy (SEM) images of JoFETs before and after gate fabrication, from which one can appreciate that the metal gate is aligned and deposited in the middle of the JJ with a precision of $\pm 150\ \text{nm}$, regardless of the gate length. SEM analysis of JoFETs with different values of L_{JJ} and L_G is reported in Fig. S2. Fig. 2f,g report the thickness profile of the JoFET surface obtained through Atomic Force Microscopy (AFM) analysis. Finally, an optical microscope photograph of the entire device is shown in Fig. 2h, from which the 4-terminals architecture of the JoFET, meant for the electrical characterization, can be appreciated.

JoFETs were measured in a dilution fridge equipped with a z-axis superconducting magnet and a DC measurement setup (Fig. S3); the electrical characterization was performed at 50 mK. Fig. 3a shows gate-dependent V-I characteristics of a JoFET featuring $W_{JJ} = 6 \mu\text{m}$, $L_{JJ} = 500 \text{ nm}$, and $L_G = 1000 \text{ nm}$. The switching current (I_S) was extracted from the V-I curves as the largest current at 0-voltage drop, while the normal state resistance (R_N) is estimated as the V-I curve slope above I_S .

By decreasing the gate voltage, a reduction of I_S and an increase of R_N is observed. This behavior is confirmed for all the JoFETs tested, regardless of their morphological properties (Fig. S4 left column).

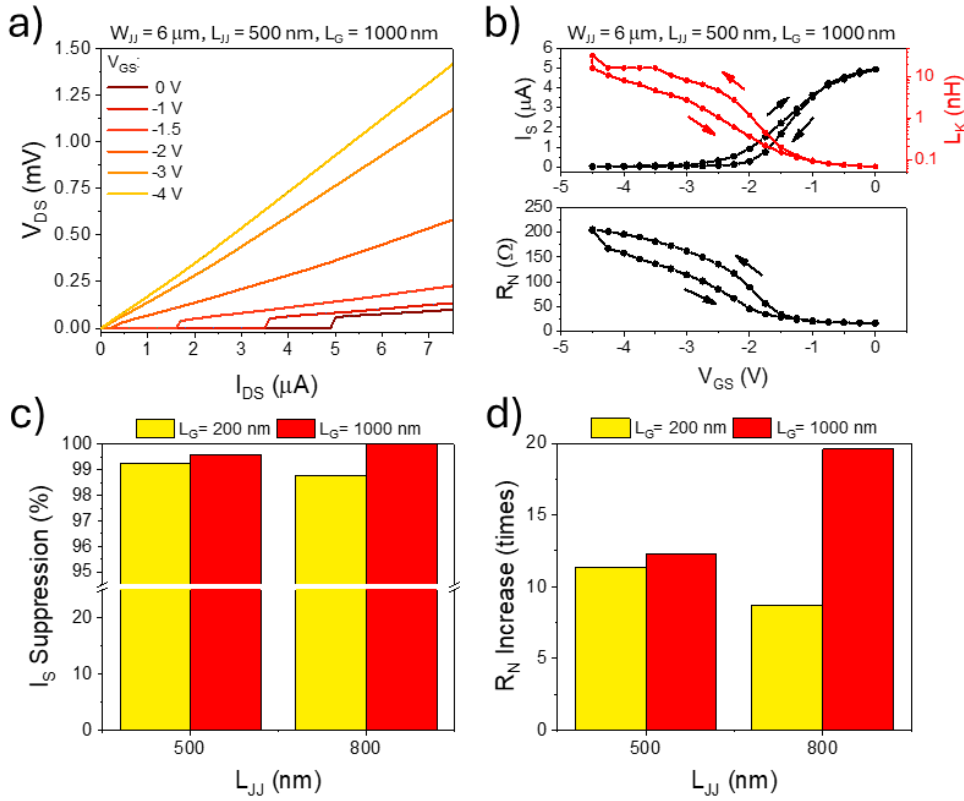


Fig. 3: InAsOI-based Josephson Field Effect Transistors electrical characterization. a) Gate-dependent voltage vs. current characteristics of a JoFET featuring $W_{JJ} = 6 \mu\text{m}$, $L_{JJ} = 500 \text{ nm}$, and $L_G = 1000 \text{ nm}$. b) Upward and downward gate-dependent switching current, kinetic inductance, and normal-state resistance of a JoFET featuring $W_{JJ} = 6 \mu\text{m}$, $L_{JJ} = 500 \text{ nm}$, and $L_G = 1000 \text{ nm}$. c,d) Switching current suppression (c) and normal-state resistance increase (d) of JoFET featuring different L_{JJ} and L_G values.

Fig. 3b shows the I_S and R_N gate dependence extracted from Fig. 3a. Fig. 3b top also reports the resulting kinetic inductance ($L_K = \frac{\hbar}{2e \times I_S}$, where \hbar is the reduced Plank's constant and e is the elementary charge). For all the curves, a sigmoidal behavior was observed with the gate voltage, with an evident hysteresis between the upward and downward scans presumably related to electrical traps

in the insulator or at the InAs/insulator interface^{60,61}. In summary, for all the JoFETs fabricated, the higher the V_{GS} value, the higher the switching current (the lower the normal state resistance), and vice versa (Fig. S4 middle column). The zero-voltage and gate-dependent electrical properties of JoFETs rely on the specific transistor morphology. With the increase of L_{JJ} , a reduction of I_S and an increase of R_N is obtained at $V_{GS} = 0$ V, as expected (Fig. S5). Moreover, at $V_{GS} = 0$ V, the larger the gate length, the lower the switching current (the higher the normal state resistance), regardless of the interelectrode separation (Fig. S5). To quantify the ability of the gate to tune the superconducting and transport properties of the JoFETs, we defined the I_S suppression factor, namely $I_{Sup} = 1 - \frac{I_{S@V_{GS}=-4.5V}}{I_{S@V_{GS}=0V}}$ (Fig. 3c), and the R_N increase factor, namely $R_{Inc} = \frac{R_{N@V_{GS}=-4.5V}}{R_{N@V_{GS}=0V}}$ (Fig. 3d). For both the interelectrode separations tested ($L_{JJ} = 500$ or 800 nm), higher I_{Sup} and R_{Inc} factors were obtained in the case of wider gates compared to the thinner ones, namely $L_G=1000$ nm instead of $L_G=200$ nm. In addition, longer JJs and more extended gates together gave the best I_{Sup} and R_{Inc} . In the case of the JoFET with $L_G=1000$ nm and $L_{JJ}=850$ nm, a 100 % switching current suppression together with ~20 times increase of the normal state resistance was obtained, changing the gate voltage in the range from 0 to -4.5 V. The higher R_{Inc} factor obtained with wider gates is directly related to larger part of InAs tuned in electron density with the applied gate electric field. At the same time, the larger gate decreases uniformly the Fermi velocity in the semiconductor channel resulting in a larger effective barrier between the semiconductor and the superconductor. This leads to a less efficient Andreev conversion at the super/semi interface with a stronger suppression of the supercurrent compared to the narrower gate configuration. Remarkably, a negligible leakage current was collected in the gate voltage operation range (Fig. S4 right column). Additional information about the temperature and magnetic field-dependent electrical behavior of the fabricate JoFETs can be found here⁵⁴. I_{Sup} and R_{Inc} achieved for InAsOI-based JoFETs are on par with the top values obtained in other gate-tunable-critical-current platforms, such as those based on InAs^{59,62,63} and Ge^{45,64,65} quantum wells (QWs), InAs⁴⁴ and metallic⁶⁶ nanowires (NWs), InAs nanosheets (NSs)⁶⁷, and graphene^{46,68} (for a comparison see Fig. S6 and Table S1). This makes InAsOI a valuable candidate for implementing cryogenic hybrid superconducting electronics, and the InAsOI-based JoFET a promising circuitual element acting as a two-state ON/OFF superconducting/normal building blocks.

We now focus on developing a superconducting 1-input-to-8-outputs (1I8O) analog demultiplexer operating at 50 mK. The roles of the I/O ports can be, in principle, reversed to operate the proposed device as a multiplexer. Fig. 4a depicts the schematic diagram of the hierarchical architecture of the demultiplexer, where three signal splitting levels are obtained involving 14 JoFETs (JoFET₀ to JoFET₁₃), one input line (I₀), eight output lines (O₀ to O₇), and six control lines (G₀₀ to G₂₁). Two indexes characterize control lines; the first one, ranging from 0 to 2, refers to the three splitting levels (ranging from left to right in the scheme of Fig. 4a), the second identifying the bottom (value of 0) or top (value of 1) output branch of each splitting node. Signal and control lines in the schematic representation are highlighted with red and blue colors, respectively, to improve the readability of the diagram.

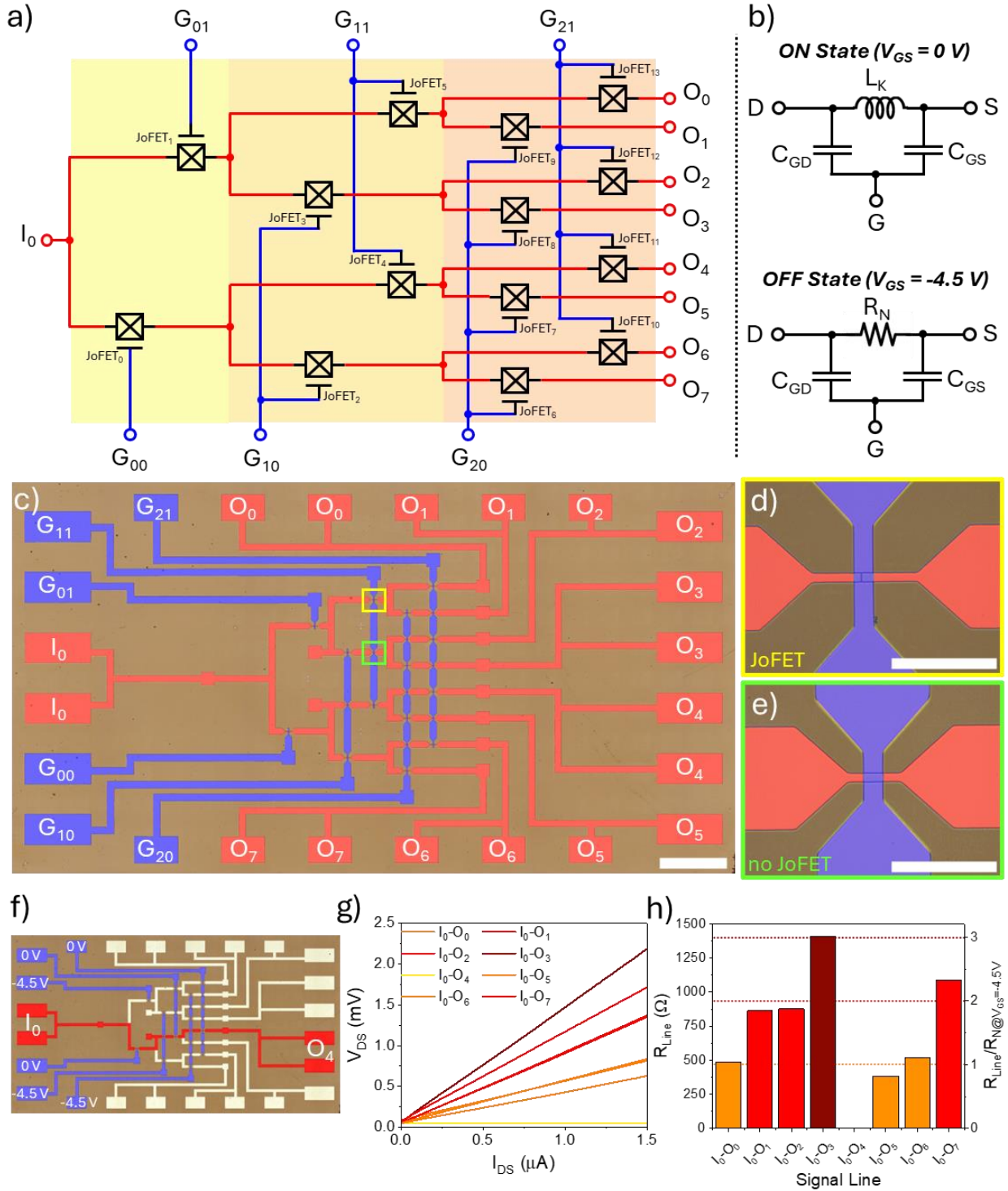


Fig. 4: Concept, morphological, and DC electrical characterization of the superconducting 1-input-8-outputs analog demultiplexer. a) Schematic diagram of the superconducting 1I8O demultiplexer. b) Electrical lumped model of the InAsOI-based JoFET. c) False-color optical microscope image of superconducting 1I8O demultiplexer; the scalebar is 500 μm . d,e) False-colors optical microscope image of an overlap between a signal and a gate control line with (d) or without (e) a JoFET; the scalebar is 50 μm . f) False-color optical microscope image of the superconducting 1I8O demultiplexer highlighting the chosen superconducting path and the gate control configuration. g) V-I characteristics of all the 1I8O demultiplexer signal lines with the gate configuration shown in (f). h) Line resistances (left) and normalized line resistances (right) of all the 1I8O demultiplexer signal lines with the gate configuration shown in (f).

The superconducting signal can be hierarchically divided from the input to one of the two following outputs depending on the gate control settings of each signal-splitting node. The number of required JoFETs (U) increases with the number of splitting levels (M) as $U = \sum_{i=1}^M 2^i = \frac{1-2^{M+1}}{-1} - 1$, while the number of output signals (O) increases with the number of control lines (N) as $O = 2^{\frac{N}{2}}$. Remarkably, the number of outputs can be improved to 2^N by using cold NOT logic gates to invert one of the controls in each signal-splitting level. To effectively accomplish a reduction in control lines, it is imperative that the NOT logic gates, which function at cryogenic temperatures, be situated at the same cold stage as the superconducting demultiplexer.

Fig. 4b depicts the schematic representation of the JoFET in the non-gated superconducting state, i.e., the ON state, and in the gated normal state, i.e., the OFF state. In the ON state ($V_{GS} = 0$ V), the JoFET acts as an inductor with value L_K ; conversely, in the OFF state ($V_{GS} = -4.5$ V), the JoFET works as a resistor with value R_N . The two capacitors between the gate and drain (C_{GD}) and gate and source (C_{GS}) terminals represent the major parasitic elements for both gate settings. The contribution of the JJ capacitance is considered negligible⁶⁹.

In the DC ON state, the current (and the power) through the JoFET totally flows into the inductive branch (**Fig. 4b top**). This trend is suppressed with the increase of the operating frequency by the gate capacitors, providing a path to the AC-grounded gate terminal. We defined the JoFET ON-state maximum operational frequency ($f_{MAX_{ON}}$) as the frequency at which the power provided by the drain to the source decreases by 10% (-0.46 dB) compared to its DC value. Based on the values reported in **Table S2**, $f_{MAX_{ON}} = 6$ GHz was retrieved from the simulations. Similarly, in the OFF state the parasitic gate capacitors limit the maximum operation frequency of the JoFET ($f_{MAX_{OFF}} = 17$ GHz) shunting R_N . The overall maximum operating frequency (f_{MAX}) of the JoFET can be expressed as $\min(f_{MAX_{ON}}, f_{MAX_{OFF}})$, resulting in $f_{MAX} = f_{MAX_{ON}}$. A detailed discussion is provided in **Section 5 of the Supporting Information**. f_{MAX} can be increased to higher frequencies designing JoFETs with a reduced gate capacitance by downsizing the gate capacitor area. Operating JoFETs at higher frequencies also requires considering the wavelength period in GaAs (λ_{GaAs}), namely $25 \div 2.5$ mm for $1 \div 10$ GHz frequencies. If λ_{GaAs} is comparable to the dimension of the fabricated chip, a specific layout with electromagnetic wave transport through waveguides is mandatory to achieve negligible insertion loss.

Fig. 4c shows a false-color optical microscope image of the 1180 demultiplexer fabricated on InAsOI. The chip is 5.5×3 mm² and features two routing levels of 50- μ m-width Al superconducting traces: the underneath for the signal lines (red traces) and the overlying for the gate control lines (blue traces).

A HfO₂ layer with 30 nm thickness was used as a gate and metal trace insulator. Each signal line is provided with two pads to perform 4-terminal electrical measurements (Fig. S7). JoFETs with $W_{JJ} = 4 \mu\text{m}$, $L_{JJ} = 500 \text{ nm}$, and $L_G = 9.5 \mu\text{m}$ were fabricated as ON/OFF building blocks. Fig. 4d shows an overlap between a signal and a gate control line where a JJ is present, i.e., the JoFET. On the other hand, Fig. 4e exhibits an overlap without active elements, which is used to reach positions on the chip with control lines that cannot be reached without two routing levels.

Table S3 reports the 1I8O demultiplexer truth table. For each gate control configuration, only one input-to-output path is fully superconductive, while all the remaining have at least one JoFET in the dissipative state. The signal line resistance is 0Ω in the case of the non-dissipative path or equal to $1 \times R_N$, $2 \times R_N$, or $3 \times R_N$ according to the number of JoFETs in series in the OFF state along the specific input-to-output line. As a case of study, we focused on having the I₀-O₄ line superconductive (Fig. 4f), with gate control lines set to $V_{G_{00}} = V_{G_{11}} = V_{G_{21}} = 0 \text{ V}$ and $V_{G_{01}} = V_{G_{10}} = V_{G_{20}} = -4.5 \text{ V}$. Fig. S8 depicts the schematic lumped element diagram of the demultiplexer with the applied gate settings to clarify the electrical configuration obtained. Fig. 4g shows V-I characteristics of all the 1I8O demultiplexer signal lines. As desired, only I₀-O₄ exhibits a 0Ω resistance path up to the switching current, while all the other lines present a dissipative path. The non-dissipative dynamic input range of the superconducting demultiplexer consequently goes from $-I_S$ to I_S . Line resistances (R_{Line}) are summarized in Fig. 4h, from which we can observe that the $R_{Line}/R_{N@V_{GS}=-4.5V}$ ratio agrees with what is expected (Table S3). By changing the gate control lines setting, the non-dissipative path can be transferred to one of the other signal lines, as reported in Fig. S9 where I₀-O₆ was selected as fully superconductive. This results from the good reproducibility of the electrical properties of both JoFETs and signal lines (Fig. S10). Over the 14 JoFETs integrated, a switching current of $1.98 \pm 0.52 \mu\text{A}$ (average \pm standard deviation) is calculated, leading to a percentage coefficient of variation (CV) of 26.2 % (Fig. S10a). Only the JoFET₇ exhibited a switching current strongly far from the average; by removing this contribution, a switching current of $2.09 \pm 0.31 \mu\text{A}$ (CV = 14.8 %) is obtained. Differently, the signal line resistance for input currents higher than the switching current, which is related to the reliability of the transport properties of the JoFETs, was calculated as $84.2 \pm 3.4 \Omega$ (CV = 4.0 %) (Fig. S10b). The achieved results indicate that by introducing technological steps typical of those of the large-scale integration, a superconducting demultiplexer with a higher number of reliable output lines can be fabricated.

We then evaluated the time-resolved electrical behavior of the superconducting 1I8O demultiplexer. We simultaneously measured signal lines I₀-O₄ and I₀-O₆ while switching between two gating configurations to have only one line in the non-dissipative state at a time. The gate voltages were

switched at a switching frequency (f_{SW}) of 100 Hz from $V_{G_{10}} = -4.5 V$ and $V_{G_{11}} = 0 V$ to cancel the resistance of line I₀-O₄, to $V_{G_{10}} = 0 V$ and $V_{G_{11}} = -4.5 V$, to make the path I₀-O₆ superconductive, while leaving all the other gate control lines to $V_{G_{00}} = V_{G_{21}} = 0 V$ and $V_{G_{01}} = V_{G_{20}} = -4.5 V$ (see **Table S3** and **Fig. 5a top**). The electrical characterization was performed in a dilution fridge equipped with a very-large-frequency (VLF) measurement setup (cut-off frequency ~ 45 kHz) with load resistances (R_L) of $\sim 200 \Omega$ due to the cryostat wire impedance (**Fig. S11**). The signal-line input current (I_{IN}) is $\sim 1.3 \mu A$. The central panel of **Fig. 5a** shows signal line voltages: only one line per time exhibits a zero voltage drop corresponding to the line with all the JoFETs in the ON state. Voltage drops measured for both the lines in the dissipative state are not identical due to the small differences in the gated line resistances (**Fig. 4h, S10c**). Correspondingly, the input current is divided into the two signal lines in agreement with the total line resistance (see **Fig. 5a bottom**). Specifically, the signal line current does not reach 0 A when the line is in the dissipative state due to the cryostat wiring impedance in series to the switch ($R_L \sim 200 \Omega$). This is a remarkable point to consider when selecting the impedance loads that the superconducting switch can drive. We defined the rise (t_r) and fall (t_f) time as the time the signal line voltage takes to go from 10% to 90% of its peak value, and vice versa, for the rise and fall time, respectively. We evaluated $t_r \approx t_f \sim 50-75 \mu s$. Since for a square signal, the contribution of the frequency harmonics higher than the carrier frequency are relevant only in the transition between the peak-to-peak value, the maximum switching frequency ($f_{SW_{MAX}}$) achievable for the TDM can be calculated as $f_{SW_{MAX}} = \frac{1}{t_r} = 15 \div 20 kHz$. The switching speed is indeed limited by the cut-off frequency of the setup used to characterize the fabricated die (**Fig. S11**).

To complete the electrical characterization of the superconducting 1180 demultiplexer, we also evaluated the AC electrical performance. We injected into the signal line I₀-O₄ an AC input current with 1 kHz frequency, collecting the voltage drop across the line. **Fig. 5b** shows the time-resolved signal line voltages measured by changing the peak-to-peak value of the input current from 2 μA to 16 μA . When the input current instantaneously overcomes the minimum switching current of the JoFETs in the I₀-O₄ path (i.e., $I_S = 1.9 \mu A$ of JoFET₄), a finite voltage drop is detected. The higher the peak-to-peak value of the input current, the higher the signal line voltage drop obtained.

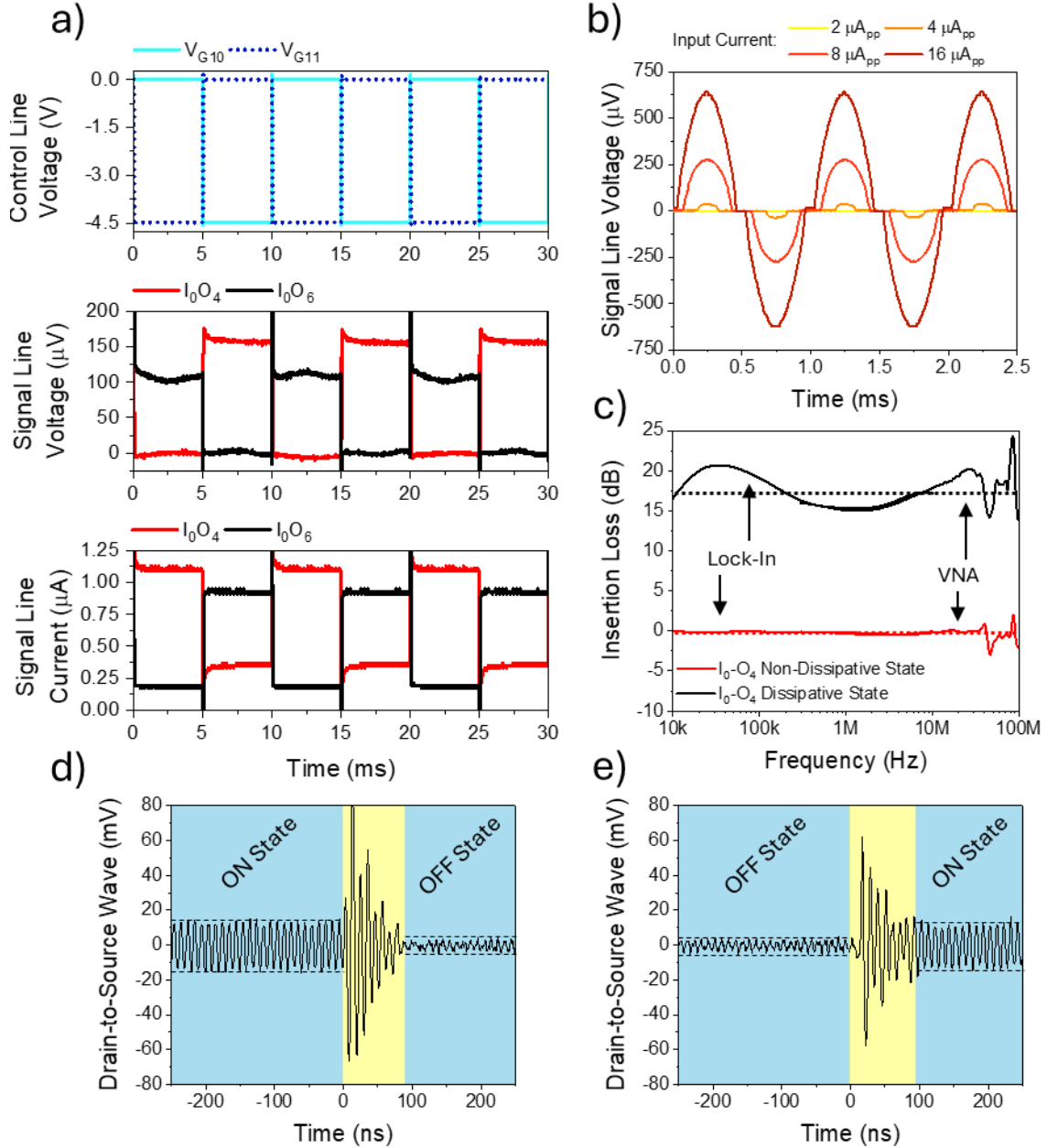


Fig. 5: Time-resolved and AC electrical characterization of the superconducting 1-input-8-outputs analog demultiplexer. a) Time-resolved electrical behavior of the superconducting demultiplexer. Time-dependent control line voltages (top), signal line voltages (middle), and signal line currents (bottom). b) Time-resolved I_0 - O_4 signal line voltage with different peak-to-peak input currents. c) Frequency-resolved insertion loss of signal line I_0 - O_4 in the non-dissipative and dissipative states. Measurements are taken with a lock-in amplifier and a VNA for low and high-frequency ranges, respectively. d,e) Drain-to-source wave voltage ($f=100$ MHz) measured during the ON-to-OFF (d) and OFF-to-ON (e) state transients. The blue areas indicate the steady state behavior while the yellow area indicates the transient.

By applying an AC signal lower than the minimal critical current supported, we then evaluated the electrical behavior of the superconducting 1I8O demultiplexer in the frequency range from 10 kHz to 100 MHz (LF-VHF radio spectrum) in a dilution fridge equipped with a 50Ω -matched cryogenic measurement setup (maximum operation frequency ~ 300 MHz, Fig. S12). A lock-in amplifier and a

vector network analyzer (VNA) were used to measure the magnitude of the forward power gain scattering parameter ($|S_{21}|$) in the 10 kHz - 10 MHz and 300 kHz - 100 MHz ranges, respectively. We simultaneously measured the output powers of signal lines I₀-O₄ and I₀-O₆, injecting an AC input signal with a -80 dBm power level (10 pW, 447 nA_{rms}). Gate settings were chosen to make superconductive only one line at a time. Fig. 5c shows the insertion loss ($IL (dB) = -S_{21}(dB)$) of the signal line I₀-O₄ in the dissipative and non-dissipative states. When the signal line is superconducting, an insertion loss of ~0 dB was measured in the whole frequency range, demonstrating that the input power is efficiently transferred to the output port of the selected signal line without significant dissipation along the path. This is a remarkable improvement compared to the case in which the demultiplexer in ON-state operates above the critical temperature of Al (specifically at 1.65 K) and, therefore, in a fully dissipative configuration. In this case, the insertion loss increases to ~5.5 dB (Fig. S13). The latter result highlights the importance of a fully superconducting path between the input and the output port. Compared with conventional gate-tunable cryogenic non-superconducting solutions, it promises a significant competitive advantage of a switchable superconducting system like the one we proposed. On the other hand, when the line is gated in the dissipative state, the insertion loss increases to ~17.5 dB, which is relatively constant over all the frequency range tested and allow to achieve an $\frac{ON}{OFF}$ ratio of ~ 17.5 dB. Similar results were also obtained for the signal line I₀-O₆ (Fig. S14).

The turn-OFF and turn-ON time-resolved behaviors of a typical JoFET ($L_{JJ} = 500$ nm, $W_{JJ} = 4$ μm, and $L_G = 1000$ nm) were reported in Fig. 5d,e. The electrical characterization was performed in dilution fridge equipped with a very-high-frequency (VHF) measurement setup (cut-off frequency ~ 100 MHz for the gate control lines, cut-off frequency ~ 500 MHz for the drain-to-source signal lines). An AC sinusoidal wave (-80 dBm power and 100 MHz frequency) was used as the drain-to-source signal; a square wave ($t_r=t_f \sim 130$ ns, Fig. S15) was used as the gate control switching signal. Switching from the ON to OFF state (Fig. 5d), the steady-state peak-to-peak voltage value of the drain-to-source wave reduces by ~7.6 times (17.6 dB in power), according to what reported in Fig. 5c. The increased wave amplitude observed during the transient was related to the displacement current generated during the gate capacitor discharge upon application of the square wave control signal. Specifically, this current sums to the drain-to-source signal current increasing the value of the drain-to-source wave voltage measured. A similar trend was observed also for the OFF-to-ON state commutation (Fig. 5e). In this case, $t_r=t_f \sim 100$ ns were achieved and traduced in an improved $f_{SW_{MAX}} = 10$ MHz, as demonstrated by the uncorrelation between t_r and t_f and the gate switching frequency reported in Fig. S16. As previously indicated, $f_{SW_{MAX}}$ is limited by the cut-off frequency of the setup used to drive

the gate control lines of the superconducting demultiplexer (Fig. S15). Fig. S17 depicts the AC drain-to-source wave increasing the JoFET gate control switching frequency from 1 kHz to 100 kHz, from which the amplitude of the drain-to-source wave was reliably and reproducibly modulated as a function of the gate voltage value applied in time.

We then theoretically estimated the static (P_{STAT}) and dynamic (P_{DYN}) power dissipated by the 1180 superconducting demultiplexer. In the DC-to- f_{MAX} range, P_{STAT} is related to the part of the input current flowing in the dissipative OFF branches (see Section 6 of Supporting Information). $P_{\text{STAT}} \sim 700$ fW was evaluated for the superconducting demultiplexer operating in the measurement setup of Fig. 5c, S12. The dynamic power dissipated by the switching activity was calculated by the well-known formula $P_{\text{DYN}} = n \times C_G \times V_{GS}^2 \times f_{SW}$, where $n = 14$ is the number of integrated JoFETs, $C_G = C_{GS} + C_{GD}$ is the gate capacitance, and f_{SW} is the gate control switching frequency (see Section 7 of Supporting Information). Referring to the cooling power of the cryostat we used throughout the experiments at the temperature of 50 mK, namely 16 μW , the 1180 superconducting demultiplexer can operate with control switching frequencies up to 400 kHz without affecting the temperature of the coldest plate. The calculations were performed in the worst-case scenario of the full P_{DYN} dissipated at mixing chamber stage. The switching frequency can be increased by reducing the size of the JoFETs and the gate voltage required to reach the OFF state.

InAsOI-Based μ wave Superconducting 1-Input-2-Outputs Analog Demultiplexer

To envisage TDM of supercurrents in the frequency operational range of transmon qubits, we focused on the development of a μ wave superconducting 1-input-to-2-outputs (1I2O) analog demultiplexer operating at 50 mK. The chip was manufactured with the same InAsOI-based technology previously described and features 2 JoFETs (JoFET₀ and JoFET₁), 1 input line (I₀), 2 output lines (O₀ and O₁), and 2 control lines (G₀ and G₁). On-chip routing of electromagnetic signals in the μ wave regime was performed by using integrated Al superconducting coplanar waveguides (CPWs), to minimize power dissipation along the I/O line in the ON-state due to the comparable values of λ_{GaAs} with the dimension of the chip at higher operating frequencies. Fig. 6a shows a false-color optical microscope image of the fabricated die, with signal and control lines highlighted in red and blue.

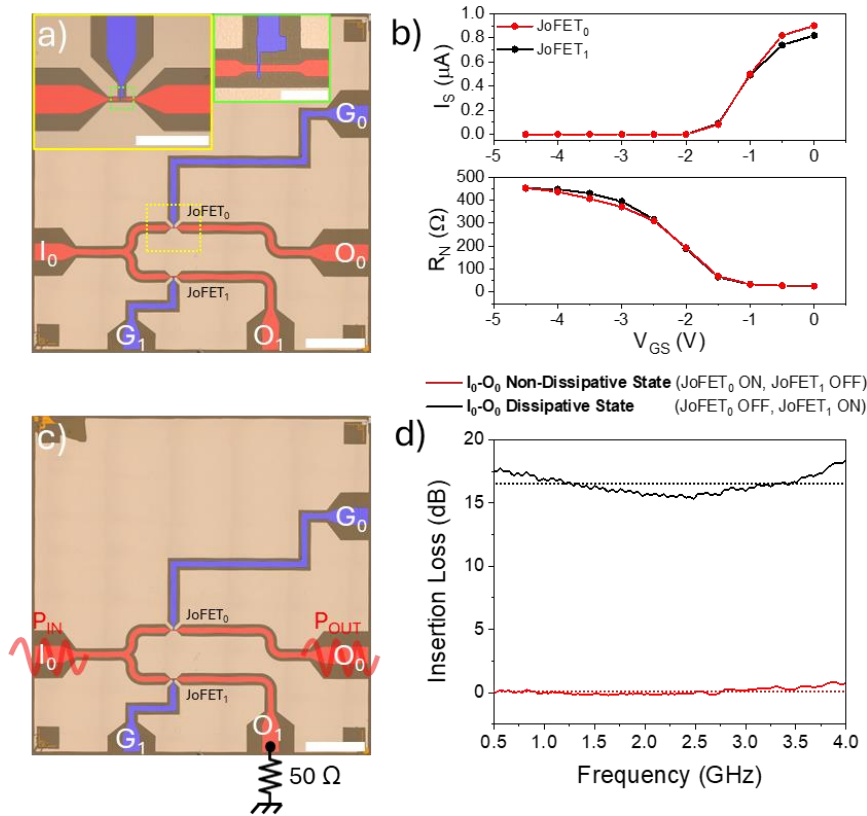


Fig. 6: Morphological, DC, and RF electrical characterization of the μ wave superconducting 1-input-2-outputs analog demultiplexer. a) False-color optical microscope image of the μ wave superconducting 1I2O demultiplexer; the scalebar is 1 mm. Yellow and green insets report false-color optical microscope image of an integrated JoFET; scalebars are 250 μ m and 25 μ m, respectively. b) Downward gate-dependent switching current and normal-state resistance of the integrated JoFETs featuring $W_{JJ} = 6$ μ m, $L_{JJ} = 800$ nm, and $L_G = 1000$ nm. c) False-color optical microscope image of the μ wave superconducting 1I2O demultiplexer highlighting the electrical configuration used to test chip. d) Frequency-resolved insertion loss of signal line I₀-O₀ in the non-dissipative and dissipative states.

The chip is $6 \times 6 \text{ mm}^2$ and embeds two JoFETs with $W_{JJ} = 6 \text{ }\mu\text{m}$, $L_{JJ} = 800 \text{ nm}$, and $L_G = 1000 \text{ nm}$ routed with Al CPWs. The gate extension L_G was reduced compared to that of the JoFETs integrated into the 1I8O superconducting demultiplexer to address the gate capacitance limitation on the OFF-state electrical properties at high frequencies, consequently increasing f_{MAX_OFF} . Both the JoFETs operate as expected, as reported from the I_S and R_N vs. V_{GS} trends depicted in Fig. 6b, from which the full suppression of the switching current as well as ~ 20 times increase of the normal state resistance was achieved in the gate range 0 to -4.5 V . The behavior of the signal line I_0 - O_0 was collected and considered as representative of all the lines of the chip, with gate settings chosen to make superconductive only one signal line at a time (Fig. 6c). An AC signal with amplitude lower than the minimal critical current supported was used to evaluate the electrical behavior of the μ wave 1I2O superconducting demultiplexer in the frequency range from 500 MHz to 4 GHz (VHF-UHF radio spectrum) by involving a dilution fridge equipped with a 50Ω -matched cryogenic measurement setup (maximum operation frequency $\sim 8.5 \text{ GHz}$, Fig. S18). An electromagnetic wave with power $P_{IN} = -80 \text{ dBm}$ (10 pW , $447 \text{ nA}_{\text{rms}}$) was provided to the input port I_0 ; the power of the electromagnetic wave reaching the output port O_0 was collected during while the output port O_1 was connected to a reference load of $50 \text{ }\Omega$. Fig. 6d shows IL of line I_0O_0 in the non-dissipative and dissipative states. In the non-dissipative state, an IL of 0 dB was observed throughout the frequency range, confirming negligible power consumption along the fully superconducting line in the VHF-UHF radio spectrum range. On the other hand, in the dissipative state, the IL increases to $\sim 16 \text{ dB}$, from which an $\frac{ON}{OFF}$ ratio of 16 dB is calculated. The achieved performance are comparable to what was observed for the 1I8O superconducting demultiplexer chip, which allow us to conclude that the proposed architecture can be employed also for operating TDM of non-dissipative supercurrents in the frequency operational range of transmon qubits. Further considerations on the use of superconducting TDM of non-dissipative signals to transmon qubits for a dramatic reduction of the I/O lines of a cryogenic quantum computer are reported in Section 8 of the Supporting Information.

Our work introduces a significant technological advancement in the form of TDM of non-dissipative signals with a voltage-actuated hybrid superconducting demultiplexer. This innovative device is designed to substantially reduce the number of input signal lines required in a conventional cryostat. The key component of this demultiplexer is an InAsOI-based JoFET, which features Al as a superconductor and HfO_2 as a gate insulator. Notably, this JoFET has the capability to completely suppress the switching current and increase the normal-state resistance by 20 times when subjected to a gate voltage of -4.5 V . In this context, the ideal building block should be capable of (i) exhibiting a high switching current in the ON-state, (ii) entirely suppressing the switching current in the OFF-

state, and (iii) exhibiting a high normal-state resistance in the OFF-state. We manufactured a superconducting demultiplexer with 1 input and 8 outputs exhibiting a significant non-dissipative dynamic input range of $-2\div 2\ \mu\text{A}$ and able to operate up to 100 MHz in signal frequency and 100 kHz in switching frequency at 50 mK. The results were remarkable, revealing an insertion loss of approximately 0 dB in the superconducting state and an $\frac{ON}{OFF}$ ratio of approximately 17.5 dB up to 100 MHz in a 50Ω -matched cryogenic measurement setup. These findings vividly illustrate the advantage of superconductivity by establishing a lossless path between the input and output ports. Additionally, the integration of on-chip routing for non-dissipative signals utilizing superconducting coplanar waveguides was employed to expand the operational frequency range of the superconducting demultiplexer. A superconducting demultiplexer with 1 input and 2 outputs was fabricated and validated up to 4 GHz in signal frequency at 50 mK. Also for the latter device, an insertion loss of ~ 0 dB in the superconducting state and an $\frac{ON}{OFF}$ ratio of ~ 16 dB were evaluated. These groundbreaking advancements demonstrate the potential for the practical implementation of superconducting TDM, which could substantially reduce in I/O lines, costs, and space occupation within a cryostat.

Methods

All the methods regarding the sample manufacturing and the cryogenic electric characterization are detailed reported within the Supporting Information file.

InAsOI Heterostructure Growth via Molecular Beam Epitaxy

InAsOI was grown on semi-insulating GaAs (100) substrates using solid-source Molecular Beam Epitaxy. Starting from the GaAs substrate, the sequence of the layer structure includes a 200 nm-thick GaAs layer, a 200 nm-thick GaAs/Al_{0.16}Ga_{0.84}As superlattice, a 200 nm-thick GaAs layer, a 1.250 μm -thick step-graded In_XAl_{1-X}As metamorphic buffer (with X increasing from 0.15 to 0.81), a 400 nm-thick In_{0.84}Al_{0.16}As overshoot layer, and a 100 nm-thick InAs layer. The GaAs layer and GaAs/AlGaAs superlattice are grown at $600\ \text{°C} \pm 5\ \text{°C}$. The metamorphic buffer and the overshoot layers were grown at optimized substrate temperatures of $320\ \text{°C} \pm 5\ \text{°C}$. The InAs epilayer was grown at $480 \pm 5\ \text{°C}$.

InAsOI Josephson Field Effect Transistor Fabrication

InAsOI substrates were cut into square samples and cleaned with organic solvents. The air-exposed InAs surface was etched from native InAs oxide (InAsO_X) and passivated with S-termination by dipping the InAsOI samples in a (NH₄)₂S_X solution (290 mM (NH₄)₂S and 300 mM S in DIW) at

45°C. The S-terminated InAsOI samples were then rinsed in DIW and loaded into an e-beam evaporator where a 100-nm-thick Al layer was deposited. After Al deposition, the mesa geometry was defined via photolithography and subsequent Al etching in Al Etchant Type D at 40 °C and InAs etching with a H₃PO₄:H₂O₂ solution (348 mM H₃PO₄, 305 mM H₂O₂ in DIW). After MESA fabrication, nanometric aligning Ti/Au markers were defined via e-beam lithography, thermal deposition of a 10/50-nm-thick Ti/Au bilayer, and lift-off. Markers were then used to define the Josephson Junction via e-beam lithography and subsequent Al etching in Al Etchant Type D at 40 °C. The 31-nm-thick HfO₂ gate insulator layer was deposited via Atomic Layer Deposition at a temperature of 130 °C. Eventually, markers were again used to define the metallic gate via e-beam lithography, e-beam deposition of a 10/100-nm-thick Ti/Al bilayer, and lift-off.

InAsOI Superconducting 1I8O Demultiplexer Fabrication

The superconducting 1I8O demultiplexer chip was fabricated according to the step previously reported for the InAsOI Josephson Field Effect Transistor Fabrication. Photolithography was used as the patterning technique to define the metallic gate lines aligned with micrometric fabricated at the mesa stage.

InAsOI μ wave Superconducting 1I2O Demultiplexer Fabrication

The μ wave superconducting 1I2O demultiplexer chip was fabricated according to the step previously reported for the InAsOI Josephson Field Effect Transistor Fabrication.

Data Availability

All the data are available upon request from the corresponding author.

Code availability

No code is used in this study.

References

1. Casparis, L. *et al.* Superconducting gatemon qubit based on a proximitized two-dimensional electron gas. *Nat. Nanotechnol.* **13**, 915–919 (2018).
2. Landig, A. J. *et al.* Virtual-photon-mediated spin-qubit–transmon coupling. *Nat. Commun.* **10**, 5037 (2019).
3. Wang, J. I. J. *et al.* Hexagonal boron nitride as a low-loss dielectric for superconducting quantum circuits and qubits. *Nat. Mater.* **21**, 398–403 (2022).
4. Pita-Vidal, M. *et al.* Direct manipulation of a superconducting spin qubit strongly coupled to a transmon qubit. *Nat. Phys.* **19**, 1110–1115 (2023).
5. Pita-Vidal, M. *et al.* Strong tunable coupling between two distant superconducting spin qubits. *Nat. Phys.* **20**, 1158–1163 (2024).
6. Ho Eom, B., Day, P. K., LeDuc, H. G. & Zmuidzinas, J. A wideband, low-noise superconducting amplifier with high dynamic range. *Nat. Phys.* **8**, 623–627 (2012).
7. Sarkar, J. *et al.* Quantum-noise-limited microwave amplification using a graphene Josephson junction. *Nat. Nanotechnol.* **17**, 1147–1152 (2022).
8. Phan, D. *et al.* Gate-Tunable Superconductor-Semiconductor Parametric Amplifier. *Phys. Rev. Appl.* **19**, 064032 (2023).
9. Splitthoff, L. J. *et al.* Gate-tunable kinetic inductance parametric amplifier. *Phys. Rev. Appl.* **21**, 014052 (2024).
10. Ando, F. *et al.* Observation of superconducting diode effect. *Nature* **584**, 373–376 (2020).
11. Baumgartner, C. *et al.* Supercurrent rectification and magnetochiral effects in symmetric Josephson junctions. *Nat. Nanotechnol.* **17**, 39–44 (2022).
12. Margineda, D. *et al.* Back-action supercurrent rectifiers. *Commun. Phys.* **8**, 16 (2025).
13. Marsili, F. *et al.* Efficient Single Photon Detection from 500 nm to 5 μm Wavelength. *Nano Lett.* **12**, 4799–4804 (2012).
14. Korzh, B. *et al.* Demonstration of sub-3 ps temporal resolution with a superconducting nanowire single-photon detector. *Nat. Photonics* **14**, 250–255 (2020).
15. Charaev, I. *et al.* Single-photon detection using high-temperature superconductors. *Nat. Nanotechnol.* **18**, 343–349 (2023).
16. Hart, S. *et al.* Controlled finite momentum pairing and spatially varying order parameter in proximitized HgTe quantum wells. *Nat. Phys.* **13**, 87–93 (2017).
17. Wiedenmann, J. *et al.* 4ϕ -periodic Josephson supercurrent in HgTe-based topological Josephson junctions. *Nat. Commun.* **7**, 1–7 (2016).
18. Laroche, D. *et al.* Observation of the 4π -periodic Josephson effect in indium arsenide nanowires. *Nat. Commun.* **10**, 245 (2019).
19. Dartiailh, M. C. *et al.* Phase Signature of Topological Transition in Josephson Junctions. *Phys. Rev. Lett.* **126**, 1–6 (2021).
20. Amet, F. *et al.* Supercurrent in the quantum Hall regime. *Science (80-.).* **352**, 966–969 (2016).
21. Seredinski, A. *et al.* Quantum Hall–based superconducting interference device. *Sci. Adv.* **5**, 2–7 (2019).
22. Vignaud, H. *et al.* Evidence for chiral supercurrent in quantum Hall Josephson junctions. *Nature* **624**, 545–550 (2023).
23. Bolotin, K. I., Ghahari, F., Shulman, M. D., Stormer, H. L. & Kim, P. Observation of the fractional quantum Hall effect in graphene. *Nature* **462**, 196–199 (2009).
24. Kerelsky, A. *et al.* Maximized electron interactions at the magic angle in twisted bilayer graphene. *Nature* **572**, 95–100 (2019).
25. Fu, H. *et al.* $3/2$ fractional quantum Hall plateau in confined two-dimensional electron gas. *Nat. Commun.* **10**, 4351 (2019).
26. Arute, F. *et al.* Quantum supremacy using a programmable superconducting processor.

- Nature* **574**, 505–510 (2019).
27. Arute, F. *et al.* Hartree-Fock on a superconducting qubit quantum computer. *Science* (80-.). **369**, 1084–1089 (2020).
 28. Yeh, J.-H. & Anlage, S. M. In situ broadband cryogenic calibration for two-port superconducting microwave resonators. *Rev. Sci. Instrum.* **84**, (2013).
 29. Oates, D. E., Slattery, R. L. & Hover, D. J. Cryogenic test fixture for two-port calibration at 4.2 K and above. in *2017 89th ARFTG Microwave Measurement Conference (ARFTG)* 1–4 (IEEE, 2017). doi:10.1109/ARFTG.2017.8000842
 30. Shin, S.-H., Stanley, M., Skinner, J., de Graaf, S. E. & Ridler, N. M. Broadband Coaxial S-Parameter Measurements for Cryogenic Quantum Technologies. *IEEE Trans. Microw. Theory Tech.* **72**, 2193–2201 (2024).
 31. Paquelet Wuetz, B. *et al.* Multiplexed quantum transport using commercial off-the-shelf CMOS at sub-kelvin temperatures. *npj Quantum Inf.* **6**, 43 (2020).
 32. Ruffino, A. *et al.* A cryo-CMOS chip that integrates silicon quantum dots and multiplexed dispersive readout electronics. *Nat. Electron.* **5**, 53–59 (2021).
 33. Potočnik, A. *et al.* Millikelvin temperature cryo-CMOS multiplexer for scalable quantum device characterisation. *Quantum Sci. Technol.* **7**, 015004 (2022).
 34. Acharya, R. *et al.* Multiplexed superconducting qubit control at millikelvin temperatures with a low-power cryo-CMOS multiplexer. *Nat. Electron.* **6**, 900–909 (2023).
 35. Ward, D. R., Savage, D. E., Lagally, M. G., Coppersmith, S. N. & Eriksson, M. A. Integration of on-chip field-effect transistor switches with dopantless Si/SiGe quantum dots for high-throughput testing. *Appl. Phys. Lett.* **102**, (2013).
 36. Al-Taie, H. *et al.* Cryogenic on-chip multiplexer for the study of quantum transport in 256 split-gate devices. *Appl. Phys. Lett.* **102**, (2013).
 37. Hornibrook, J. M. *et al.* Cryogenic Control Architecture for Large-Scale Quantum Computing. *Phys. Rev. Appl.* **3**, 024010 (2015).
 38. Olšteins, D. *et al.* Cryogenic multiplexing using selective area grown nanowires. *Nat. Commun.* **14**, 7738 (2023).
 39. Wagner, A., Ranzani, L., Ribeill, G. & Ohki, T. A. Demonstration of a superconducting nanowire microwave switch. *Appl. Phys. Lett.* **115**, (2019).
 40. Naaman, O., Abutaleb, M. O., Kirby, C. & Rennie, M. On-chip Josephson junction microwave switch. *Appl. Phys. Lett.* **108**, (2016).
 41. Pechal, M. *et al.* Superconducting Switch for Fast On-Chip Routing of Quantum Microwave Fields. *Phys. Rev. Appl.* **6**, 024009 (2016).
 42. Akazaki, T., Takayanagi, H., Nitta, J. & Enoki, T. A Josephson field effect transistor using an InAs-inserted-channel In_{0.52}Al_{0.48}As/In_{0.53}Ga_{0.47}As inverted modulation-doped structure. *Appl. Phys. Lett.* **68**, 418–420 (1996).
 43. Shabani, J. *et al.* Two-dimensional epitaxial superconductor-semiconductor heterostructures: A platform for topological superconducting networks. *Phys. Rev. B* **93**, 155402 (2016).
 44. Doh, Y.-J. *et al.* Tunable Supercurrent Through Semiconductor Nanowires. *Science* (80-.). **309**, 272–275 (2005).
 45. Vigneau, F. *et al.* Germanium Quantum-Well Josephson Field-Effect Transistors and Interferometers. *Nano Lett.* **19**, 1023–1027 (2019).
 46. Generalov, A. A. *et al.* Wafer-scale CMOS-compatible graphene Josephson field-effect transistors. *Appl. Phys. Lett.* **125**, (2024).
 47. Clark, T. D., Prance, R. J. & Grassie, A. D. C. Feasibility of hybrid Josephson field effect transistors. *J. Appl. Phys.* **51**, 2736–2743 (1980).
 48. Amado, M., Fornieri, A., Biasiol, G., Sorba, L. & Giazotto, F. A ballistic two-dimensional-electron-gas Andreev interferometer. *Appl. Phys. Lett.* **104**, 1–5 (2014).
 49. Fornieri, A. *et al.* A ballistic quantum ring Josephson interferometer. *Nanotechnology* **24**, 245201 (2013).

50. Amado, M. *et al.* Electrostatic tailoring of magnetic interference in quantum point contact ballistic Josephson junctions. *Phys. Rev. B* **87**, 134506 (2013).
51. Roddaro, S. *et al.* Hot-electron effects in InAs nanowire Josephson junctions. *Nano Res.* **4**, 259–265 (2011).
52. Paghi, A. *et al.* InAs on Insulator: A New Platform for Cryogenic Hybrid Superconducting Electronics. *Adv. Funct. Mater.* **35**, (2025).
53. Battisti, S. *et al.* Extremely weak sub-kelvin electron–phonon coupling in InAs on Insulator. *Appl. Phys. Lett.* **125**, (2024).
54. Paghi, A. *et al.* Josephson Field Effect Transistors with InAs on Insulator and High Permittivity Gate Dielectrics. *ACS Appl. Electron. Mater.* (2025). doi:10.1021/acsaelm.5c00038
55. Affentauschegg, C. & Wieder, H. H. Properties of InAs/InAlAs heterostructures. *Semicond. Sci. Technol.* **16**, 708–714 (2001).
56. Strickland, W. M., Hatefipour, M., Langone, D., Farzaneh, S. M. & Shabani, J. Controlling Fermi level pinning in near-surface InAs quantum wells. *Appl. Phys. Lett.* **121**, 1–6 (2022).
57. Capotondi, F. *et al.* Two-dimensional electron gas formation in undoped In_{0.75}Ga_{0.25}As/In_{0.75}Al_{0.25}As quantum wells. *J. Vac. Sci. Technol. B Microelectron. Nanom. Struct. Process. Meas. Phenom.* **22**, 702–706 (2004).
58. Paghi, A., Battisti, S., Tortorella, S., De Simoni, G. & Giazotto, F. Cryogenic behavior of high-permittivity gate dielectrics: The impact of atomic layer deposition temperature and the lithographic patterning method. *J. Appl. Phys.* **137**, (2025).
59. Sütő, M. *et al.* Near-surface InAs two-dimensional electron gas on a GaAs substrate: Characterization and superconducting proximity effect. *Phys. Rev. B* **106**, 235404 (2022).
60. Kukli, K. *et al.* Effect of selected atomic layer deposition parameters on the structure and dielectric properties of hafnium oxide films. *J. Appl. Phys.* **96**, 5298–5307 (2004).
61. Baik, M. *et al.* Effects of thermal and electrical stress on defect generation in InAs metal–oxide–semiconductor capacitor. *Appl. Surf. Sci.* **467–468**, 1161–1169 (2019).
62. Akazaki, T., Takayanagi, H., Nitta, J. & Enoki, T. A Josephson field effect transistor using an InAs-inserted-channel In_{0.52}Al_{0.48}As/In_{0.53}Ga_{0.47}As inverted modulation-doped structure. *Appl. Phys. Lett.* **68**, 418–420 (1996).
63. Mayer, W. *et al.* Superconducting proximity effect in epitaxial Al-InAs heterostructures. *Appl. Phys. Lett.* **114**, (2019).
64. Aggarwal, K. *et al.* Enhancement of proximity-induced superconductivity in a planar Ge hole gas. *Phys. Rev. Res.* **3**, L022005 (2021).
65. Tosato, A. *et al.* Hard superconducting gap in germanium. *Commun. Mater.* **4**, 23 (2023).
66. De Simoni, G., Paolucci, F., Solinas, P., Strambini, E. & Giazotto, F. Metallic supercurrent field-effect transistor. *Nat. Nanotechnol.* **13**, 802–805 (2018).
67. Yan, S. *et al.* Supercurrent, Multiple Andreev Reflections and Shapiro Steps in InAs Nanosheet Josephson Junctions. *Nano Lett.* **23**, 6497–6503 (2023).
68. Zhu, M. *et al.* Supercurrent and multiple Andreev reflections in micrometer-long ballistic graphene Josephson junctions. *Nanoscale* **10**, 3020–3025 (2018).
69. Courtois, H., Meschke, M., Peltonen, J. T. & Pekola, J. P. Origin of Hysteresis in a Proximity Josephson Junction. *Phys. Rev. Lett.* **101**, 067002 (2008).

Acknowledgments

We thank Stefan Heun for helping to carry out room-temperature and cryogenic measurements to estimate InAs mobility and two-dimensional charge density. We thank Andrea Ria for the valuable discussion about the JoFET's lumped element model. This work was partially supported by H2020-EU.1.2. - EXCELLENT SCIENCE - Future and Emerging Technologies (FET) under grant 964398 (SuperGate), by HORIZON.3.1 - The European Innovation Council (EIC) – Transition Open Programme under grant 101057977 (SPECTRUM), and by the Piano Nazionale di Ripresa e Resilienza, Ministero dell'Università e della Ricerca (PNRR MUR) Project under Grant PE0000023-NQSTI.

Author Contributions

A.P. and F.G. conceptualized the experiments. A.P. and L.S. fabricated the samples. A.P. and S.T. performed the experiments. A.P., L.B., and S.T. analyzed the data. A.P. performed the electrical simulations. A.P. prepared the figures and wrote the original draft. A.P., L.B., S.T., G.D.S., E.S., L.S., and F.G. discussed the results and contributed to the original draft. A.P. led the review process. L.B., E.S., and F.G. contributed to the review process. F.G. supervised the overall activity.

Ethics Declaration

Competing interests

The authors declare no competing interests.

Supporting Information

Non-Dissipative Supercurrent Time Division Multiplexing with Solid-State Integrated Hybrid Superconducting Electronics

Alessandro Paghi^{1*}, Simone Tortorella¹, Laura Borgongino¹, Giorgio De Simoni¹, Elia Strambini¹, Lucia Sorba¹, and Francesco Giazotto^{1*}

¹Istituto Nanoscienze-CNR and Scuola Normale Superiore, Piazza San Silvestro 12, 56127 Pisa, Italy.

²Dipartimento di Ingegneria Civile e Industriale, Università di Pisa, Largo Lucio Lazzarino, 56122 Pisa, Italy

*Corresponding authors: alessandro.paghi@nano.cnr.it, francesco.giazotto@sns.it

Summary

1. Supporting Tables	1
2. Supporting Figures	7
3. Materials and Manufacturing Methods	25
3.1. Materials and Chemicals	25
3.2. InAsOI Heterostructure Growth via Molecular Beam Epitaxy	25
3.3. InAsOI Josephson Field Effect Transistor Fabrication	26
3.4. InAsOI Superconducting 1180 Demultiplexer Fabrication	29
3.5. InAsOI μ wave Superconducting 1120 Demultiplexer Fabrication	30
3.6. InAsOI Hall Bars Fabrication	31
3.7. Sample Bonding via Wire Wedge Bonding	32
4. Characterization Methods	32
4.1. Morphological Characterization	32
4.2. Electrical Characterization	33
4.2.1. Cryogenic Electrical Characterization of InAsOI Josephson Field Effect Transistors	33
4.2.2. Cryogenic Electrical Characterization of the Superconducting 11800 Demultiplexer	34

4.2.3. Cryogenic Electrical Characterization of the μ wave Superconducting I ₁ I ₂ O Demultiplexer	36
4.2.4. Cryogenic and Room Temperature Electrical Characterization of InAsOI	37
5. Estimation of the JoFET Maximum Operational Frequency	38
6. Estimation of the Static Power Dissipation	40
7. Estimation of the Dynamic Power Dissipation	42
8. Envisage of Superconducting Time Division Multiplexing of Transmon Qubits	44
References	46

1. Supporting Tables

Table S1. State of the art of JoFETs. For each platform, the most representative JoFETs are reported. In the case of NWs, “W” stays for the NW diameter. “*” means that electrical or morphological properties are extrapolated from the figures of the papers and not directly provided by the authors.

InAsOI															
Specs	Super conductor	L _{JJ} [nm]	W _{JJ} [μm]	I _C (V _{GS} =0V) [μA]	I _C /W _{JJ} (V _{GS} =0V) [μA/μm]	I _C Suppr. [%]	R _N (V _{GS} =0V) [Ω]	R _N Incr. [times]	ΔV _{GS} [V]	Gate Type	Gate Insulator	Gate Distance [nm]	T [mK]	Year	Ref.
$n_{2D}=1.35 \times 10^{12} \text{ cm}^{-2}$, $\mu_n=6700 \text{ cm}^2/\text{Vs}$	Al	800	5	1.14	0.274	100	16.8	19.6	-4.5	Top	HfO ₂	30	50	2024	This Work
$n_{2D}=1.35 \times 10^{12} \text{ cm}^{-2}$, $\mu_n=6700 \text{ cm}^2/\text{Vs}$	Al	500	5	4.92	0.826	99.6	28.7	12.3	-4.5	Top	HfO ₂	30	50	2024	This Work
InAs 3D Substrates															
Specs	Super conductor	L _{JJ} [nm]	W _{JJ} [μm]	I _C (V _{GS} =0V) [μA]	I _C /W _{JJ} (V _{GS} =0V) [μA/μm]	I _C Suppr. [%]	R _N (V _{GS} =0V) [Ω]	R _N Incr. [times]	ΔV _{GS} [V]	Gate Type	Gate Insulator	Gate Distance [nm]	T [mK]	Year	Ref.
<i>p</i> -InAs	Nb	400	-	25	-	99.9	158*	316*	-20	Top	SiO ₂ /Nb _x O _y	100/70	20	1995	[1]
<i>p</i> -InAs	Nb	200	50	75*	1.5*	100*	2*	15*	-20	Top	SiO ₂	-	1800	1999	[2]
InAs 2D QWs															
Specs	Super conductor	L _{JJ} [nm]	W _{JJ} [μm]	I _C (V _{GS} =0V) [μA]	I _C /W _{JJ} (V _{GS} =0V) [μA/μm]	I _C Suppr. [%]	R _N (V _{GS} =0V) [Ω]	R _N Incr. [times]	ΔV _{GS} [V]	Gate Type	Gate Insulator	Gate Distance [nm]	T [mK]	Year	Ref.
Buried-QW t=4 nm, $n_{2D}=1.9 \times 10^{12} \text{ cm}^{-2}$, $\mu_n=155000 \text{ cm}^2/\text{Vs}$	Nb	400	80	20.7	0.259	71*	2.5*	2*	-15	Top	SiO ₂ /InAlAs /InGaAs	100/20 /13.5	1000	1995	[3] [4]
Buried-QW t=4 nm, $n_{2D}=2.3 \times 10^{12} \text{ cm}^{-2}$, $\mu_n=111000 \text{ cm}^2/\text{Vs}$	Nb	350	40	5	0.125	100	16	91250	-1.15	Top	InAlAs /InGaAs	20 /13.5	1000	1995	[5] [6] [7]
Buried-QW $n_{2D}=1.1 \times 10^{12} \text{ cm}^{-2}$, $\mu_n=160000 \text{ cm}^2/\text{Vs}$	Nb	600	20	15.6	0.780	100	5.9	-	-25	Top	SiO ₂	300	1700	2002	[8] [9]
Near-Surface-QW t=7 nm, $\mu_n=17700 \text{ cm}^2/\text{Vs}$	Al	200	3	1.45*	0.483*	100*	90*	10*	-3.5	Top	Al ₂ O ₃	40	30	2016	[10]
Near-Surface-QW t=7 nm, $n_{2D}=1.3 \times 10^{12} \text{ cm}^{-2}$ $\mu_n=15600 \text{ cm}^2/\text{Vs}$	Al	250	3	1.85*	0.616*	100	100*	17*	-2.5	Top	Al ₂ O ₃	40	30	2017	[11]

Near-Surface-QW t=4 nm, n _{2D} =7.2×10 ¹¹ cm ⁻² , μ _n =14400cm ² /Vs	Al	100	4	4.87*	1.21*	100*	100*	27*	-10	Top	AlO _x	50	20	2019	[12]
Near-Surface-QW t=7 nm, n _{2D} =8.7×10 ¹¹ cm ⁻² μ _n =52400cm ² /Vs	Al	40	1.5	1.37*	0.913*	100	270*	4*	-2.2	Top	HfO ₂	30	30	2019	[13]
Buried-QW t=4 nm, n _{2D} =6.2×10 ¹¹ cm ⁻² , μ _n =160000cm ² /Vs	Nb	900	0.73	-	-	100	-	-	-3	Side	-	1250	350	2019	[14]
Near-Surface-QW t=4 nm, n _{2D} =3.7×10 ¹¹ cm ⁻² μ _n =200000cm ² /Vs	Nb	900	3.6	0.095*	0.026*	84*	420*	3.6*	-25	Side	-	-	315	2019	[15]
Near-Surface-QW t=4 nm, n _{2D} =7×10 ¹¹ cm ⁻²	Al	100	4	2.25*	0.563*	88*	160*	4*	-2*	Top	h-BN	6	30	2021	[16]
Near-Surface-QW t=7 nm, n _{2D} =9.6×10 ¹¹ cm ⁻² μ _n =16800cm ² /Vs	Al	150	4	1.8	0.45	100	323	6*	-8	Top	Al ₂ O ₃	60	30	2021	[17]
Near-Surface-QW t=4 nm, n _{2D} =3.7×10 ¹² cm ⁻²	Al	250	4	1.9*	0.475*	100*	60*	17.8*	-1.5	Top	Al ₂ O ₃	10	17	2021	[18]
Near-Surface-QW t=4 nm, n _{2D} =7×10 ¹¹ cm ⁻²	Al	100	4	4.85*	1.213*	75*	95*	2.7*	-7.5*	Top	AlO _x	50	30	2021	[16]
NW-QW t=30 nm, μ _n =3200cm ² /Vs	Al	120	0.18 5	0.048*	0.259*	100	1930*	1.9*	-0.3	Top	HfO ₂	15	20	2021	[19]
Near-Surface-QW t=4 nm, n _{2D} =4-6×10 ¹¹ cm ⁻² μ _n =0.9- 1.3×10 ⁵ cm ² /Vs	Al	300	9	1.1	0.122	100	34*	48.5*	-3.5	Top	Al ₂ O ₃	50	20	2022	[20]
Near-Surface-QW t=7 nm, n _{2D} =1.6×10 ¹² cm ⁻² μ _n =12000cm ² /Vs	Al	150	3	0.86*	0.286*	100*	10*	1*	-1	Top	HfO ₂	15	50	2023	[21]
Near-Surface-QW t=8 nm, n _{2D} =8×10 ¹¹ cm ⁻² μ _n =18000cm ² /Vs	Al	100	-	0.280	-	100*	80*	9.8*	-0.8	Top	Al ₂ O ₃ /HfO ₂	3/15	10	2024	[22]

InAs 2D NSs															
Specs	Super conductor	L _{JJ} [nm]	W _{JJ} [μm]	I _C (V _{GS} =0V) [μA]	I _C /W _{JJ} (V _{GS} =0V) [μA/μm]	I _C Suppr. [%]	R _N (V _{GS} =0V) [Ω]	R _N Incr. [times]	ΔV _{GS} [V]	Gate Type	Gate Insulator	Gate Distance [nm]	T [mK]	Year	Ref.
t=15-30 nm, n _{2D} =4×10 ¹¹ cm ⁻² , μ _n =8300cm ² /Vs	Al	90	0.3	0.036*	0.12*	10*	1760*	2.5*	-10	Back	SiO ₂	300	20	2023	[23]
t=15-30 nm, n _{2D} =4×10 ¹¹ cm ⁻² , μ _n =8300cm ² /Vs	Al	90	0.3	0.067*	0.223*	54*	402*	3*	-8	Top	Al ₂ O ₃	30	20	2023	[23]
InAs 1D NWs															
Specs	Super conductor	L _{JJ} [nm]	W _{JJ} [μm]	I _C (V _{GS} =0V) [μA]	I _C /W _{JJ} (V _{GS} =0V) [μA/μm]	I _C Suppr. [%]	R _N (V _{GS} =0V) [Ω]	R _N Incr. [times]	ΔV _{GS} [V]	Gate Type	Gate Insulator	Gate Distance [nm]	T [mK]	Year	Ref.
n-InAs n _{3D} =2÷10×10 ¹⁸ cm ⁻³ , μ _n =200÷2000cm ² /Vs	Al	100-450	0.04 - 0.13	0.0012	-	100	4500	15.5	-71	Back	SiO ₂	250	40	2005	[24]
n-InAs n _{3D} =1.0×10 ¹⁸ cm ⁻³	Nb	70	0.08	0.0028	0.035	100	3800	2.01*	-20	Back	SiO ₂	-	500	2012	[25]
n-InAs	Nb	55	0.08	0.075	0.938	46.7	1523*	1.56*	-7	Back	-	-	15	2021	[26]
n-InAs	Sn	100	-	0.24*	-	83.7*	962*	5.31*	-0.5	Top	HfO ₂	10	40	2023	[27]
Ge 2D QWs															
Specs	Super conductor	L _{JJ} [nm]	W _{JJ} [μm]	I _C MAX [μA]	I _C /W _{JJ} [μA/μm]	I _C Suppr. [%]	R _N min [Ω]	R _N Incr. [times]	ΔV _{GS} [V]	Gate Type	Gate Insulator	Gate Distance [nm]	T [mK]	Year	Ref.
Near-Surface-QW t=16 nm, p _{2D} =6×10 ¹¹ cm ⁻² , μ _h =500000cm ² /Vs	Al	50	1	0.043 (V _{GS} =-4V)	0.043	100	371* (V _{GS} =-4V)	2.70*	2	Top	Al ₂ O ₃	-	10	2019	[28]
Buried-QW t=16 nm, p _{2D} =2÷3×10 ¹¹ cm ⁻² , μ _h ~2÷3×10 ⁵ cm ² /Vs	Al	1000	0.5*	0.006* (V _{GS} =-1.95V)	0.012*	100*	1120* (V _{GS} =-1.95V)	7*	0.95	Top	HfO ₂	40	15	2019	[29]
Buried-QW t=16 nm, p _{2D} =6×10 ¹¹ cm ⁻² , μ _h =5×10 ⁵ cm ² /Vs	Al/Nb	150	-	1 (V _{GS} =-2.5V)	-	94.3*	344* (V _{GS} =-2.5V)	2.90*	1.5	Top	Al ₂ O ₃	20	20	2021	[30]
Buried-QW t=16 nm, p _{2D} =6×10 ¹¹ cm ⁻² , μ _h ~6×10 ⁵ cm ² /Vs	PtSiGe	70	0.04	0.1* (V _{GS} =-2V)	2.5*	100*	510* (V _{GS} =-2V)	-	0.75	Top	Al ₂ O ₃	10	15	2023	[31]

Buried-QW $t=20$ nm, $p_{2D} = 2.7 \times 10^{11}$ cm ⁻² $\mu_h = 8.3 \times 10^5$ cm ² /Vs	PtSiGe	0.3	4	0.93 ($V_{GS}=-1.2V$)	0.2325	100	100 ($V_{GS}=-1.2V$)	>1.2*	0.5	Top	SiO ₂	12	80	2024	[32]	
Buried-QW $t=16$ nm, $p_{2D} = 6 \times 10^{11}$ cm ⁻² $\mu_h = 5 \times 10^5$ cm ² /Vs	PtSiGe	0.3*	-	0.01* ($V_{PG}=-2.22V$, $V_{HS}=-1V$, $V_{LB}=-0.9V^*$, $V_{RB}=-1.5V^*$)	-	100*	-	-	-	Top + Side	Al ₂ O ₃	7	9	2025	[33]	
Graphene																
Specs	Super conductor	L _{JJ} [nm]	W _{JJ} [μm]	I _C [μA]	I _C /W _{JJ} [μA/μm]	I _C Suppr. [%]	R _N [Ω]	R _N Incr. [times]	ΔV _{GS} [V]	Gate Type	Gate Insulator	Gate Distance [nm]	T [mK]	Year	Ref.	
Monolayer <i>p</i> -type regime	Nb	150 0	6	1.59* ($V_{GS}=-60$ V)	0.265*	98.7* ($V_{GS}=0$ V)	52* ($V_{GS}=-60$ V)	12.5*	60	Back	SiO ₂	300	300	2018	[34]	
Monolayer <i>n</i> -type regime $\mu_n = 300000$ cm ² /Vs	Nb	150 0	6	7 ($V_{GS}=60$ V)	1.167	99.7 ($V_{GS}=0$ V)	19* ($V_{GS}=60$ V)	30*	-60	Back	SiO ₂	300	300	2018	[34]	
Monolayer $p_{2D}=5.5 \times 10^{12}$ cm ⁻² $\mu_n = 2100$ cm ² /Vs	Nb	250	80	1.9 ($V_{GS}=-50$ V)	0.024	89	40 ($V_{GS}=-50$ V)	4	113.8 5	Back	SiO ₂	300	320	2019	[35]	
Monolayer	Al	300	20	0.9* ($V_{GS}=10$ V)	0.045*	74*	24.1* ($V_{GS}=10$ V)	3.6*	-21.6	Top	Al ₂ O ₃	30	42	2024	[36]	
Monolayer	Al	350	20	1* ($V_{GS}=10$ V)	0.05*	85*	23.8* ($V_{GS}=10$ V)	5.6*	-22.2	Top	Al ₂ O ₃	30	42	2024	[36]	
Monolayer	Al	250	50	2.34* ($V_{GS}=10$ V)	0.047*	80*	14.4* ($V_{GS}=10$ V)	3*	-22.5	Top	Al ₂ O ₃	30	42	2024	[36]	
Monolayer	Al	300	50	3.15* ($V_{GS}=10$ V)	0.063*	77*	13.3* ($V_{GS}=10$ V)	2.1*	-21.1	Top	Al ₂ O ₃	30	42	2024	[36]	
Metal NWs																
Specs	Super conductor	L _{JJ} [nm]	W _{JJ} [μm]	I _C ($V_{GS}=0V$) [μA]	I _C /W _{JJ} ($V_{GS}=0V$) [μA/μm]	I _C Suppr. [%]	R _N ($V_{GS}=0V$) [Ω]	R _N Incr. [times]	ΔV _{GS} [V]	Gate Type	Gate Insulator	Gate Distance [nm]	T [mK]	Year	Ref.	

NW t = 30 nm	Ti	900	0.2	11	55	100	45	1	40	Back + Side	-	112*	5	2018	[37]
NW t = 11 nm	Al	800	0.03	12.3	410	35	320	1	70	Back	-	112*	5	2018	[37]
DB	Nb	100	0.9	0.03	0.033	90	30	1	40	Side	-	70	30	2020	[38]
DB t = 60 nm	V	160	0.09	1420	15778	100	110	1	15	Side	-	70	2	2020	[39]

1 **Table S2. Theoretical frequency-dependent electrical behavior of the lumped element model**
 2 **of the JoFET fabricated in the superconducting 1180 demultiplexer.**

f [Hz]	L_K [pH]	$ Z_{L_K} $ [Ω] <i>ON-state</i>	R_N [Ω] <i>OFF-state</i>	$C_{GS} = C_{GD}$ [fF]	$ Z_{C_{GS}} = Z_{C_{GD}} $ [Ω]	λ_{GaAs} [mm]
10M	163	0.01	564	90	176839	2500
100M	163	0.10	564	90	17683.9	250
1G	163	1.02	564	90	1768.39	25
10G	163	10.2	564	90	176.839	2.5

3

4 **Table S3. Superconducting 1180 demultiplexer truth table.** The highlighted rows are the gate
 5 settings reported in the paper.

Gate Control Lines						Line Resistance (Referred To I_0)							
G_{00}	G_{01}	G_{10}	G_{11}	G_{20}	G_{21}	O_0	O_1	O_2	O_3	O_4	O_5	O_6	O_7
-4.5 V	0	-4.5 V	0	-4.5 V	0	0	1R _N	1R _N	2R _N	1R _N	2R _N	2R _N	3R _N
-4.5 V	0	-4.5 V	0	0	-4.5 V	1R _N	0	2R _N	1R _N	2R _N	1R _N	3R _N	2R _N
-4.5 V	0	0	-4.5 V	-4.5 V	0	1R _N	2R _N	0	1R _N	2R _N	3R _N	1R _N	2R _N
-4.5 V	0	0	-4.5 V	0	-4.5 V	2R _N	1R _N	1R _N	0	3R _N	2R _N	2R _N	1R _N
0	-4.5 V	-4.5 V	0	-4.5 V	0	1R _N	2R _N	2R _N	3R _N	0	1R _N	1R _N	2R _N
0	-4.5 V	-4.5 V	0	0	-4.5 V	2R _N	1R _N	3R _N	2R _N	1R _N	0	2R _N	1R _N
0	-4.5 V	0	-4.5 V	-4.5 V	0	2R _N	3R _N	1R _N	2R _N	1R _N	2R _N	0	1R _N
0	-4.5 V	0	-4.5 V	0	-4.5 V	3R _N	2R _N	2R _N	1R _N	2R _N	1R _N	1R _N	0

6

7

8

9

10

11

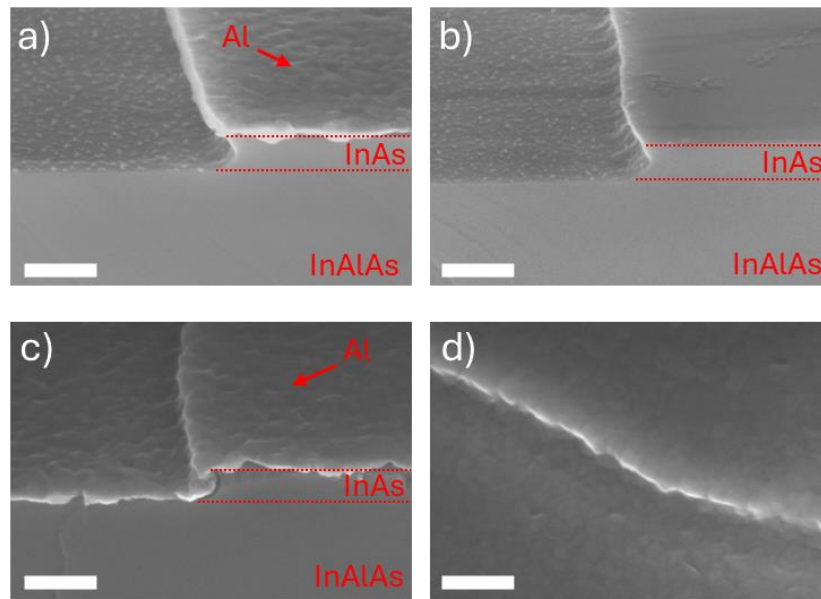
12

13

14

15

16 **2. Supporting Figures**



17

18 **Figure S1: Tilted scanning electron microscopy analysis (100k \times) of InAs MESA edge coating**
19 **by metal gate.** (a) InAs profile after MESA definition via wet etching. (b) InAs profile after Al
20 removal from MESA. (c,d) InAs profile coverage via tilted Ti/Al deposition. The scalebar is 200
21 nm.

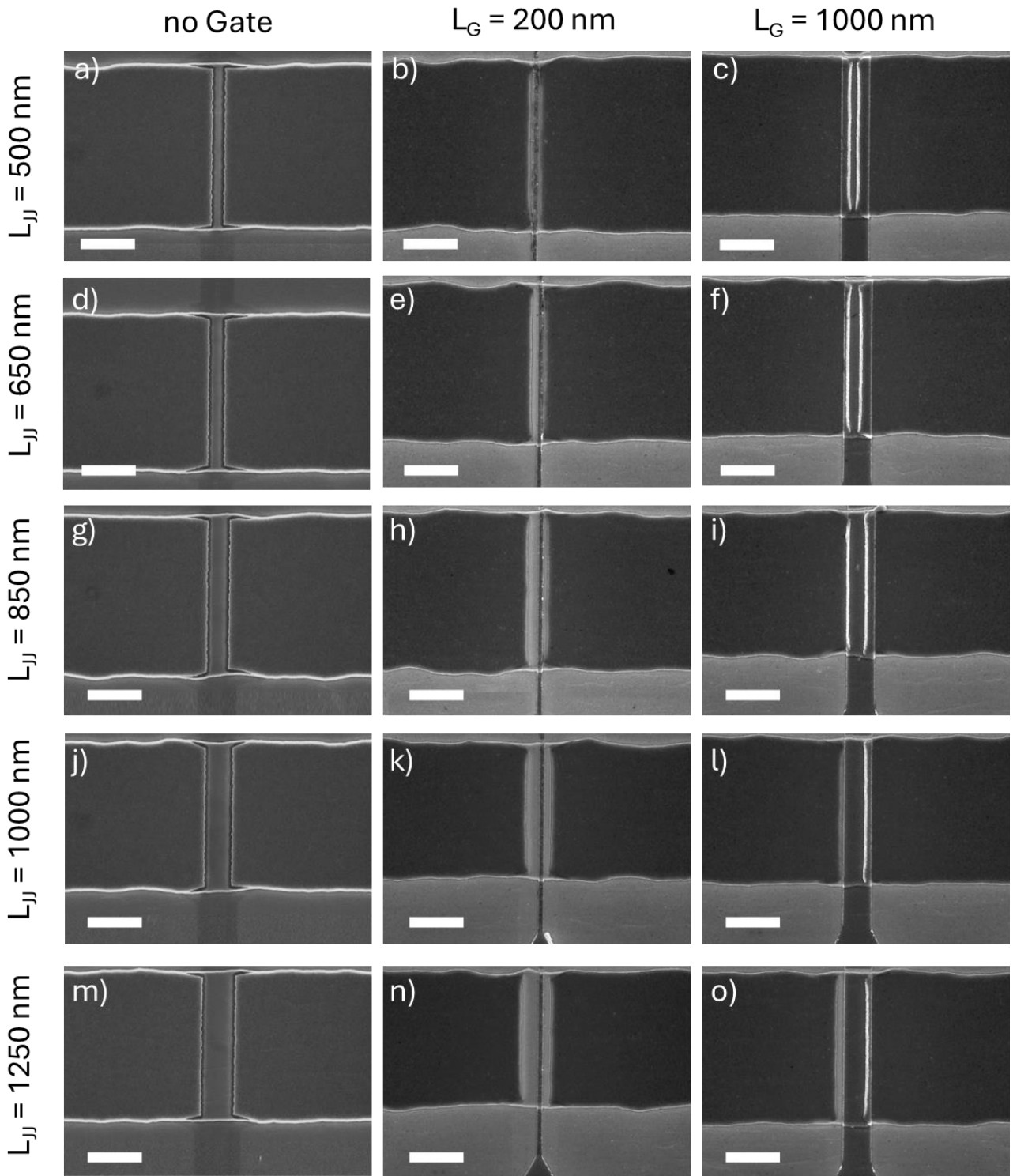
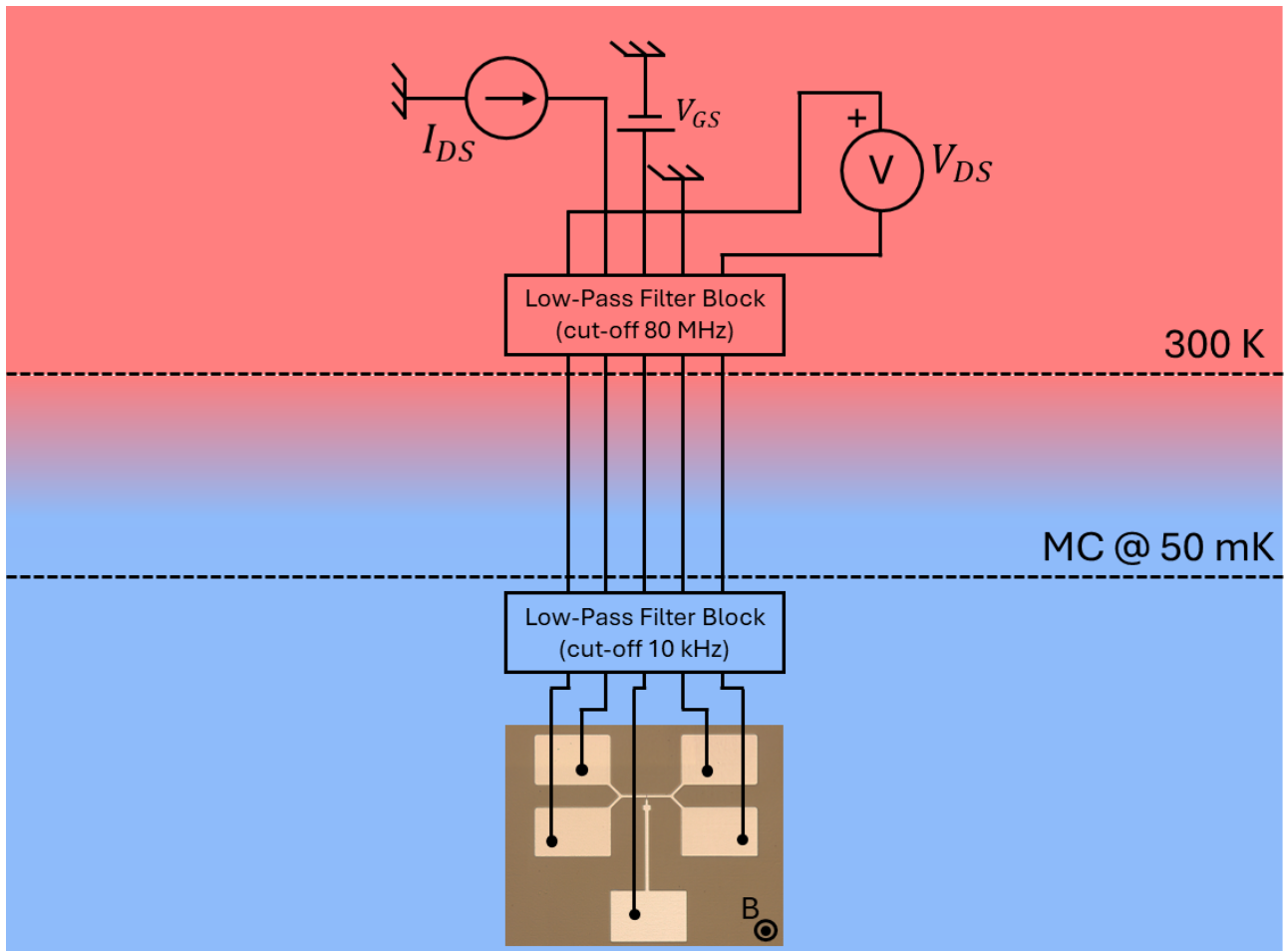


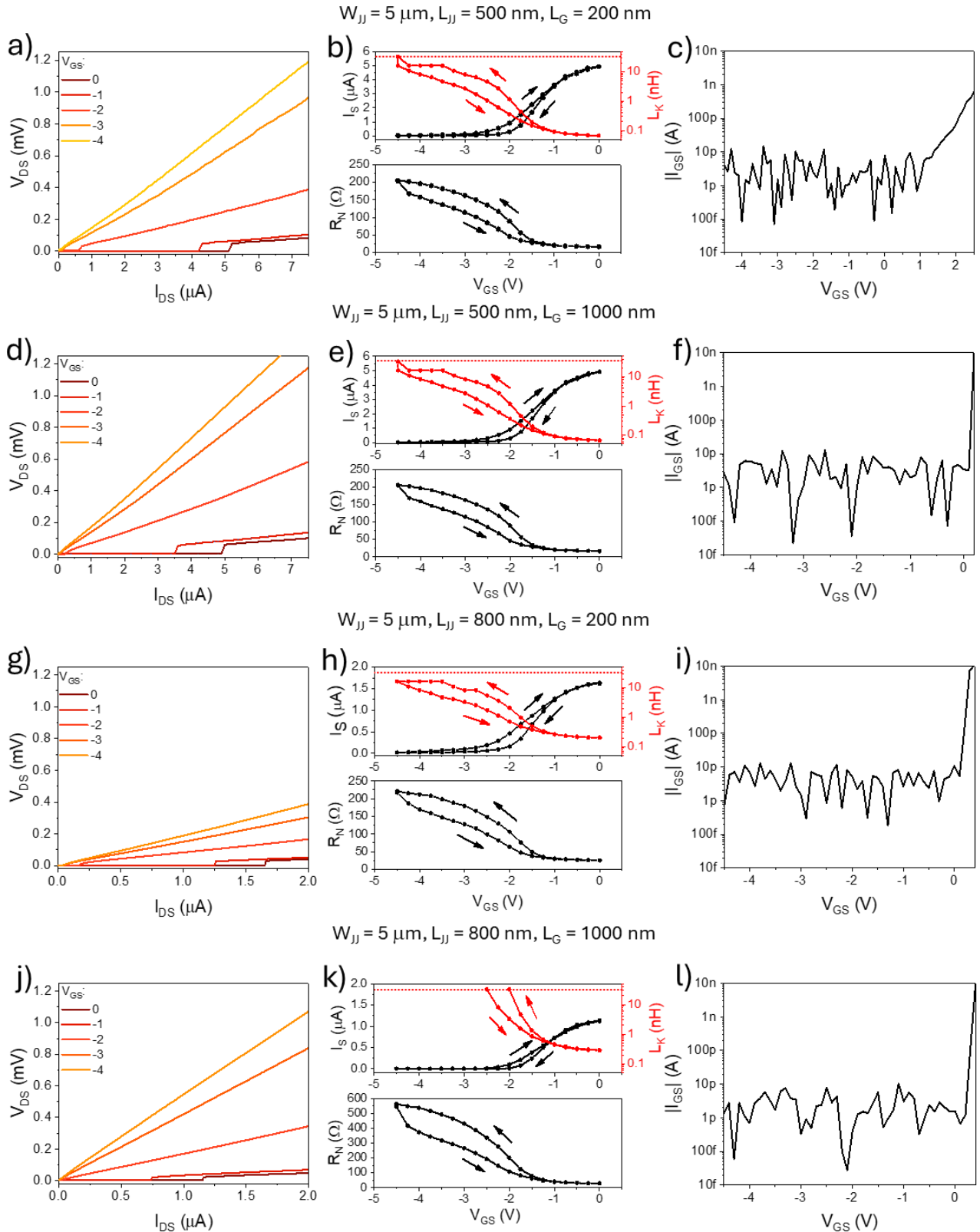
Figure S2: Top-view scanning electron microscopy analysis (10k \times) of JoFETs. a,d,g,j,m) SEM images of JoFETs before gate architecture manufacturing, i.e., Josephson Junctions, with different interelectrode separations. b,e,h,k,n) SEM images of JoFETs featuring $L_G = 200$ nm with different interelectrode separations. c,f,i,l,o) SEM images of JoFETs featuring $L_G = 1000$ nm with different interelectrode separations. The scalebar is 2 μ m.

22
23
24
25
26
27
28
29
30
31
32



33
34
35

Figure S3: DC measurement setup used to characterize the JoFETs in a dilution fridge equipped with a z-axis superconducting magnet.



36
37
38
39
40
41
42
43

Figure S4: InAsOI-based Josephson Field Effect Transistors electrical characterization.

a,d,g,j) Gate-dependent voltage vs. current characteristic of JoFETs. b,e,h,k) Upward and downward gate-dependent switching current, kinetic inductance, and normal state resistance of JoFETs. c,f,i,l) Gate leakage current vs. gate voltage of JoFETs. Measurements were performed at 50 mK.

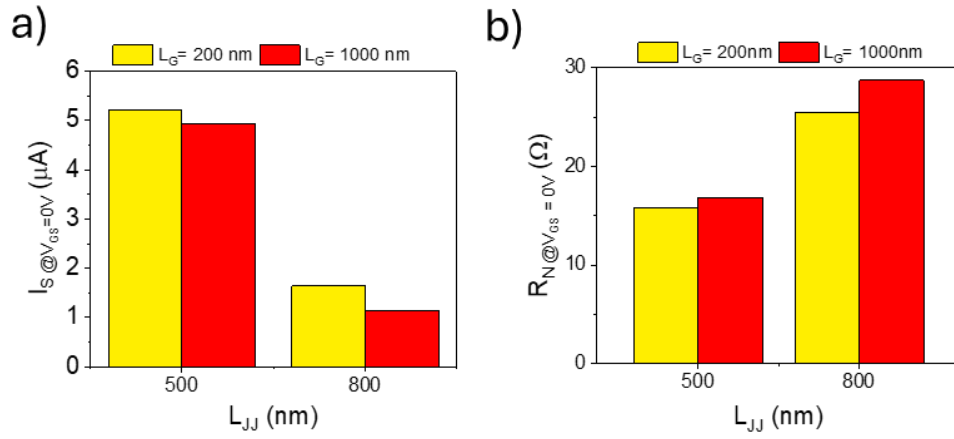
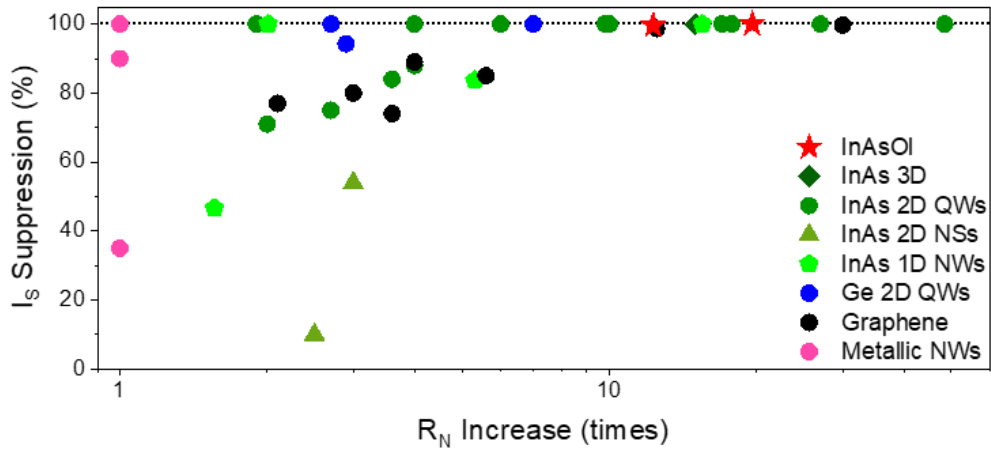


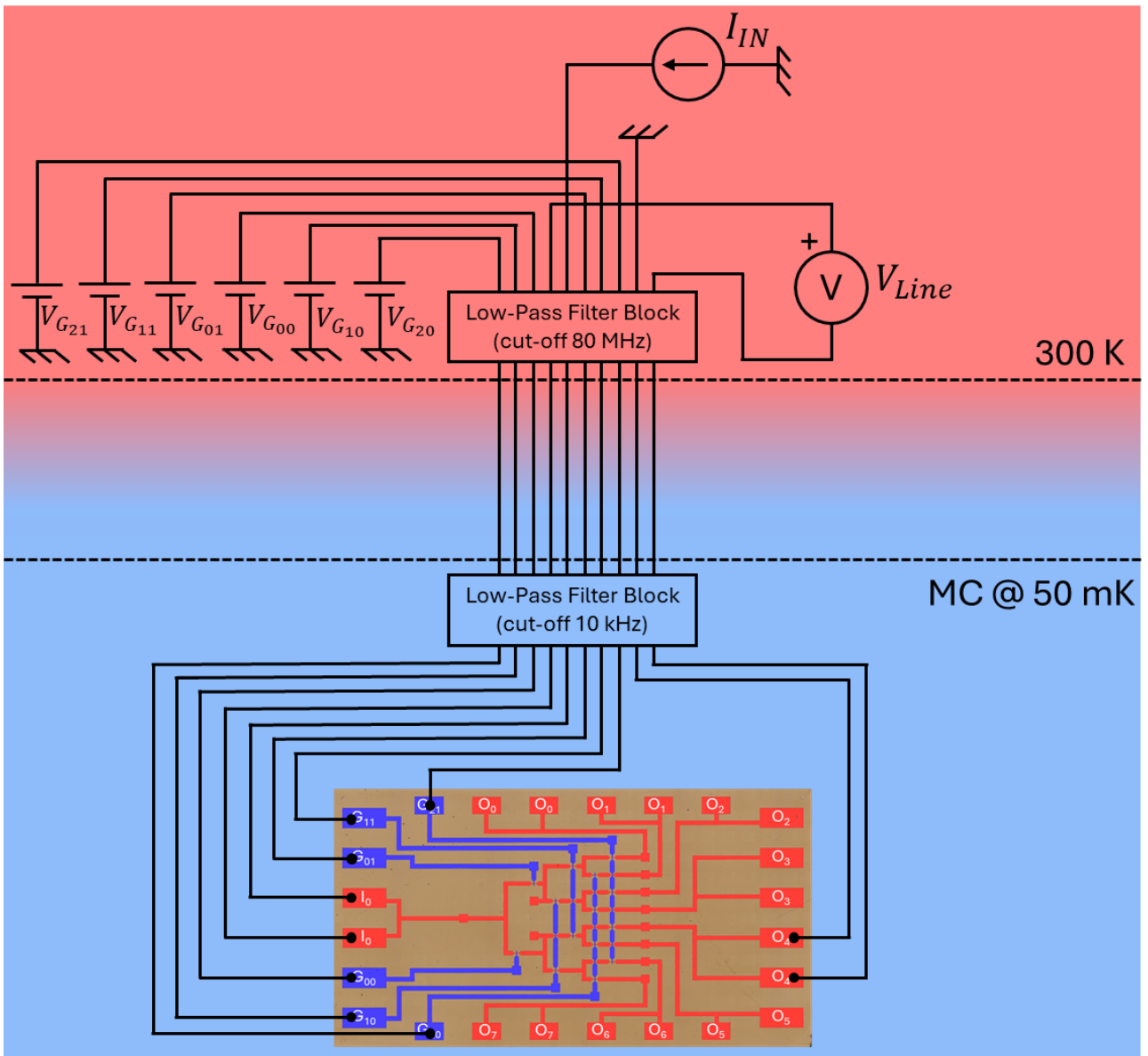
Figure S5: Zero-gate-voltage electrical properties of JoFETs. a,b) Switching current (a) and normal state resistance (b) of JoFETs with different gate lengths and interelectrode separations.

45
46
47
48
49
50
51
52
53
54
55
56
57
58
59
60
61
62
63
64
65
66
67
68
69
70
71
72



73
74
75
76
77
78
79
80
81
82
83
84
85
86
87
88

Figure S6: State of the art of JoFETs. I_s suppression and R_N increase factors achieved for InAsOI-based JoFETs are perfectly in agreement with the top values obtain in the research field.

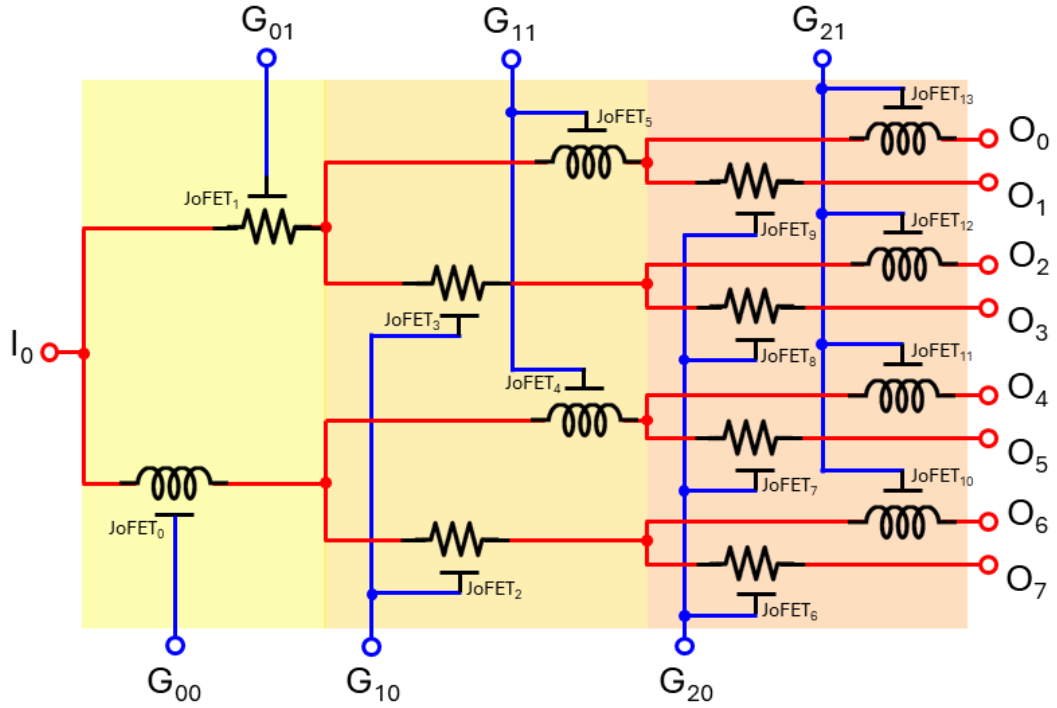


89

90 **Figure S7: DC measurement setup used to characterize the DC electrical behavior of the**
 91 **superconducting 1180 analog demultiplexer.** The input current (I_{IN}) was provided to the
 92 demultiplexer input while the signal line voltage drops (V_{Line}) are measured changing the gate
 93 settings. The figure shows only one line connected.

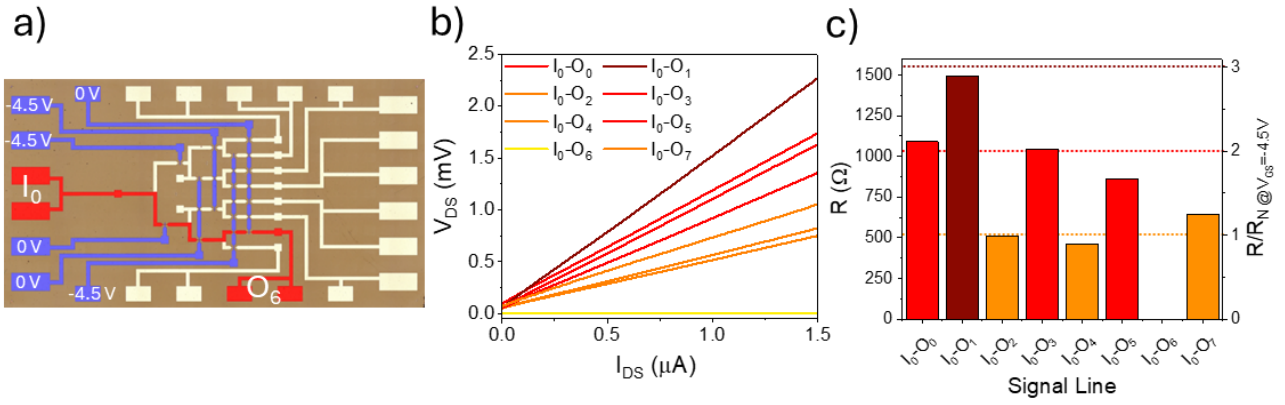
94

95



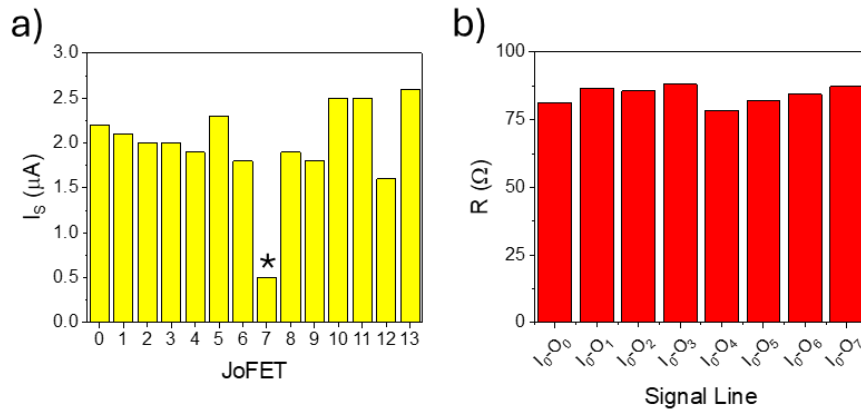
96
 97
 98
 99
 100
 101
 102
 103
 104
 105
 106
 107
 108
 109
 110
 111
 112
 113
 114
 115
 116
 117

Figure S8: Schematic lumped elements diagram of the superconducting 1180 demultiplexer with the signal line I_0 - O_4 in superconducting state. The gate settings are $V_{G00}, V_{G11}, V_{G21} = 0$ V and $V_{G01}, V_{G10}, V_{G20} = -4.5$ V.



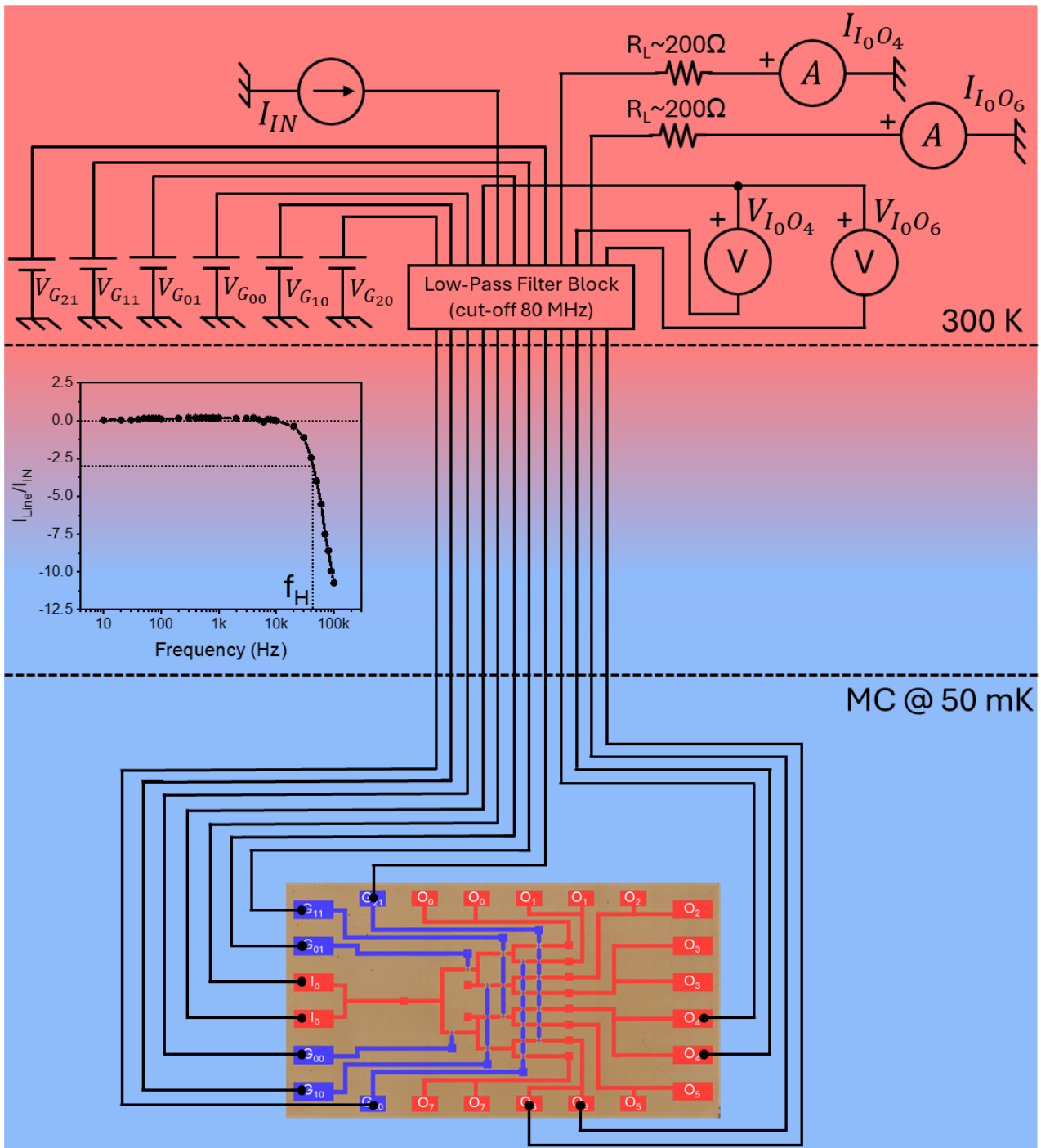
118
 119 **Figure S9: DC electrical characterization of the superconducting 1180 demultiplexer with the**
 120 **signal line I₀-O₆ in superconducting state.** a) False-colors optical microscope image of the
 121 superconducting 1180 demultiplexer highlighting the chosen superconductive path and the gate
 122 control configuration. b) V-I characteristics of all the 1180 switch signal lines with the gate
 123 configuration shown in (a). Line resistances (left) and normalized line resistances (right) of all the
 124 1180 demultiplexer signal lines with the gate configuration shown in (a).

125
 126
 127
 128
 129
 130
 131
 132
 133
 134
 135
 136
 137
 138
 139

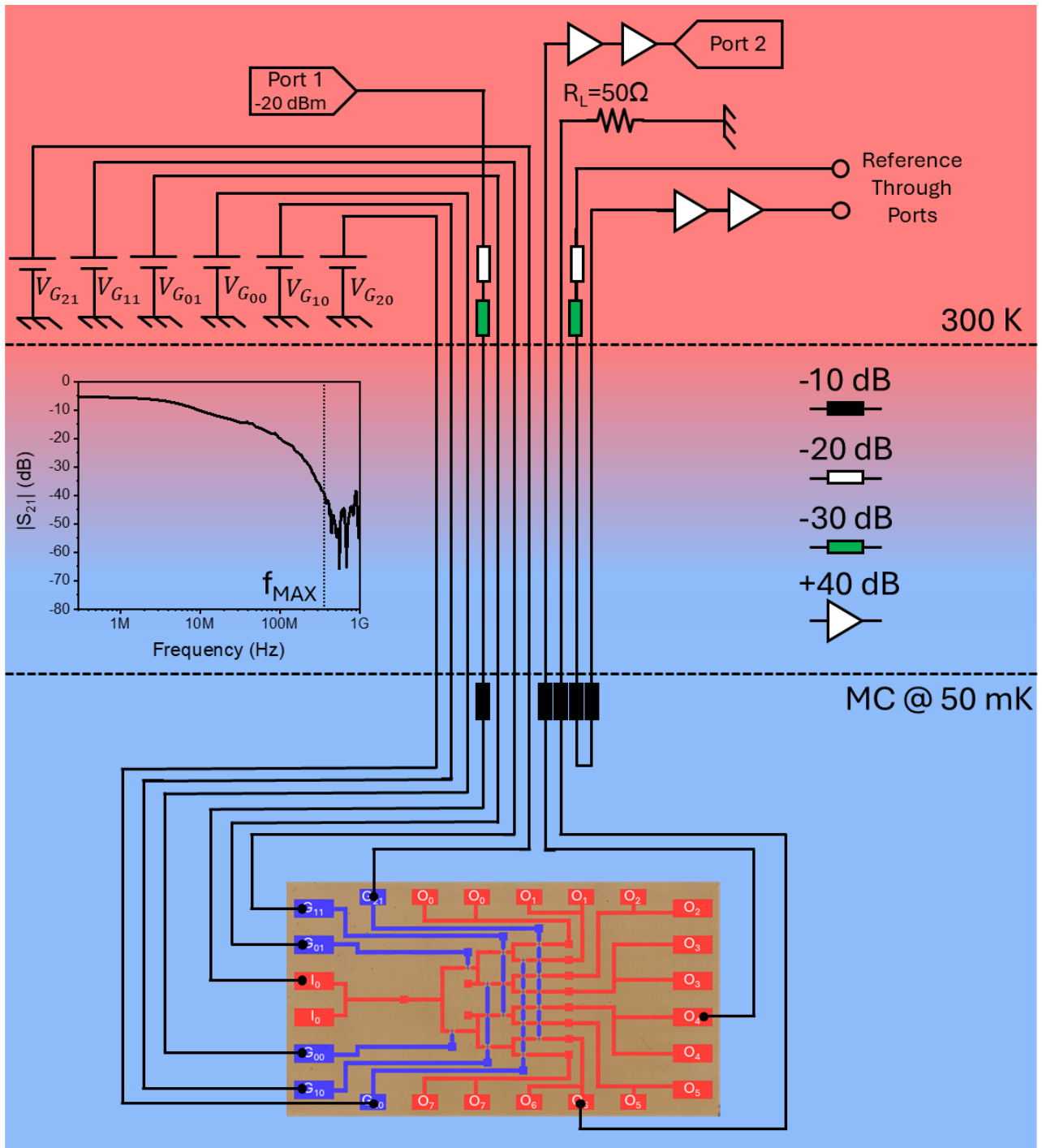


140
 141
 142
 143
 144
 145
 146
 147
 148
 149

Figure S10: Zero-gate-voltage electrical properties of JoFETs and signal lines of the superconducting 1180 analog demultiplexer. a) Zero-gate-voltage switching currents of the JoFETs; only the JoFET₇ exhibits a switching current far from the average. b) Zero-gate-voltage signal line resistances for input currents higher than the switching current.

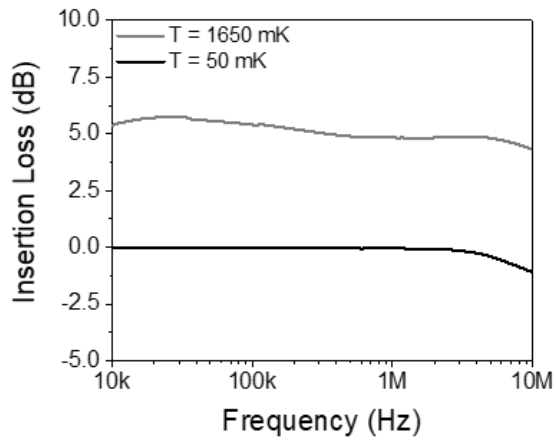


150
 151 **Figure S11: DC-VLF measurement setup used to characterize the real-time electrical**
 152 **behavior of the superconducting 1180 analog demultiplexer.** The input current (I_{IN}) was
 153 provided to the demultiplexer input while the signal line output currents ($I_{I_0O_4}$ and $I_{I_0O_6}$) and the
 154 signal line voltage drops ($V_{I_0O_4}$ and $V_{I_0O_6}$) are measured changing the gate settings. Cryostat's wires
 155 account as a load resistance of 200 Ω . The system exhibits a cut-off frequency of ~ 45 kHz at 300 K.
 156



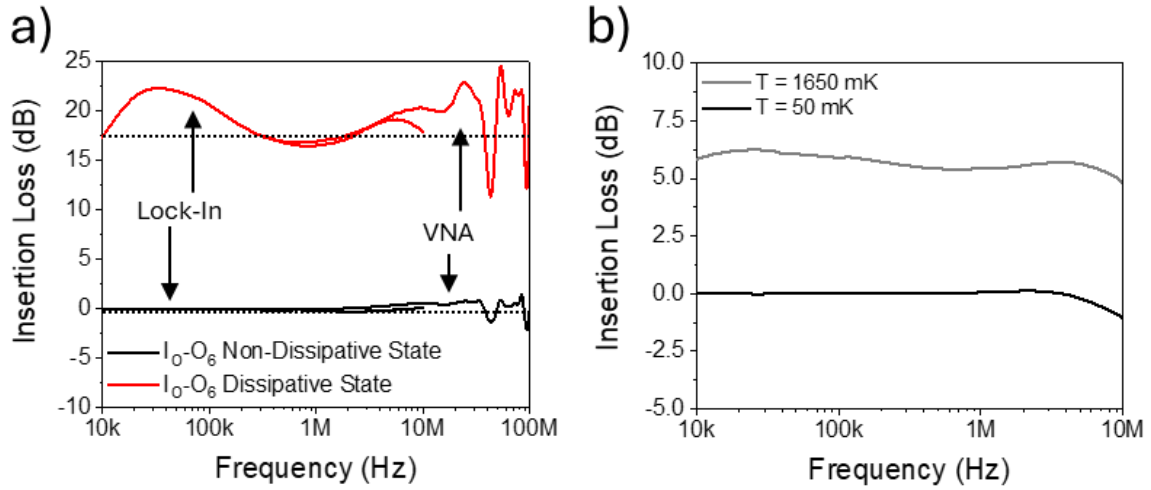
157
158
159
160
161
162
163
164
165
166

Figure S12: LF-VHF measurement setup used to characterize the frequency-resolved electrical behavior of the superconducting 1180 analog demultiplexer. The input power ($P_{IN} = -20 \text{ dBm}$) supplied by the Port₁ was attenuated both at 300 K (-50 dB) and 50 mK (-10 dB) then provided to the demultiplexer input. The line O₄ output power was attenuated at 50 mK (-10 dB) and amplified at 300 K (+80 dB) then provided to the Port₂, while line O₆ was terminated with 50 Ω. The output power was measured by changing the gate settings. The same was performed to check the line O₆ output power. Reference through ports were used to collect the trough calibration data. The system exhibits a maximum operation frequency of $\sim 300 \text{ MHz}$ at 300 K.

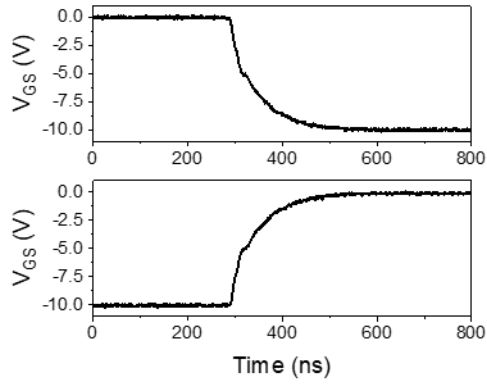


167
 168
 169
 170
 171
 172
 173
 174
 175
 176
 177
 178
 179
 180
 181
 182
 183
 184
 185
 186
 187
 188
 189
 190
 191
 192
 193
 194

Figure S13: Frequency-resolved insertion loss of signal line I₀-O₄ gated in the non-dissipative state measured at 50 mK and 1650 mK. At 1650 mK, the 1I8O demultiplexer is in the normal state which increases the insertion loss of the signal line.



195 **Figure S14: Frequency-resolved insertion loss of signal line I₀-O₄.** a) Frequency-resolved
 196 insertion loss of signal line I₀-O₆ in the non-dissipative and dissipative states at 50 mK. b)
 197 Frequency-resolved insertion loss of signal line I₀-O₆ gated in the non-dissipative state measured at
 198 50 mK and 1650 mK. At 1650 mK, the 118O demultiplexer is in the normal state which increases
 199 the insertion loss of the signal line.
 200
 201
 202
 203
 204
 205
 206
 207
 208
 209
 210
 211
 212
 213
 214
 215
 216
 217



218
219 **Figure S15: Gate control switching voltage during the ON-to-OFF (up) and OFF-to-ON**
220 **(bottom) state transients.** The square wave gate control signal travels into the cryostat and comes
221 out for measurement. The returned room temperature control signal exhibited t_r and t_f of ~ 130 ns.
222

223

224

225

226

227

228

229

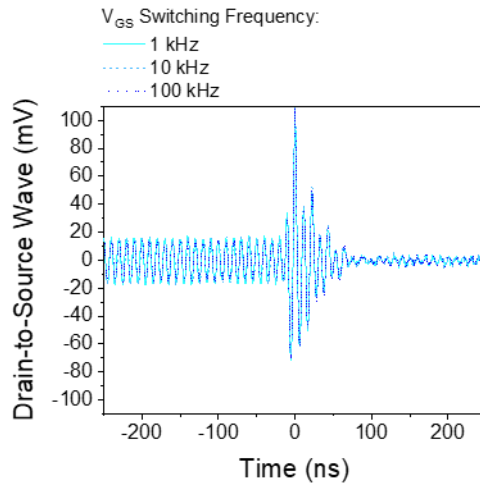
230

231

232

233

234



235
 236 **Figure S16: Drain-to-source wave voltage ($f=100$ MHz) measured during the ON-to-OFF state**
 237 **transient with different JoFET gate control switching frequencies.**
 238

239

240

241

242

243

244

245

246

247

248

249

250

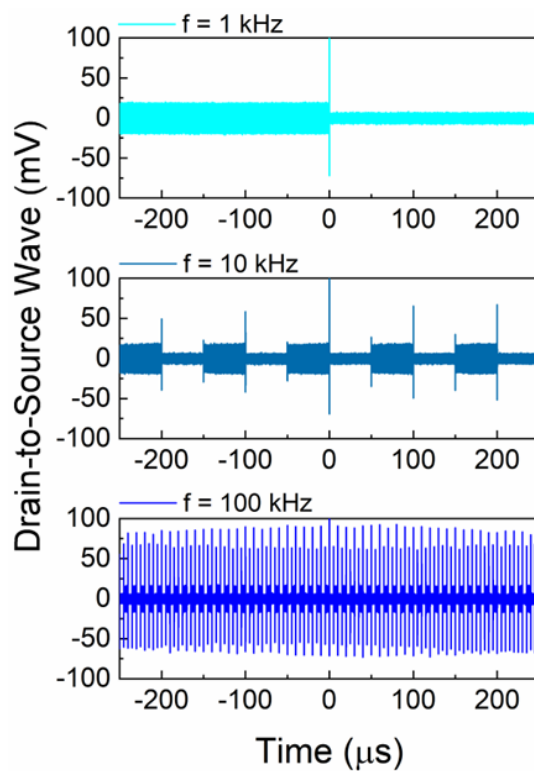
251

252

253

254

255



256
257
258
259

Figure S17: Drain-to-source wave voltage ($f=100 \text{ MHz}$) measured with different JoFET gate control switching frequencies.

260

261

262

263

264

265

266

267

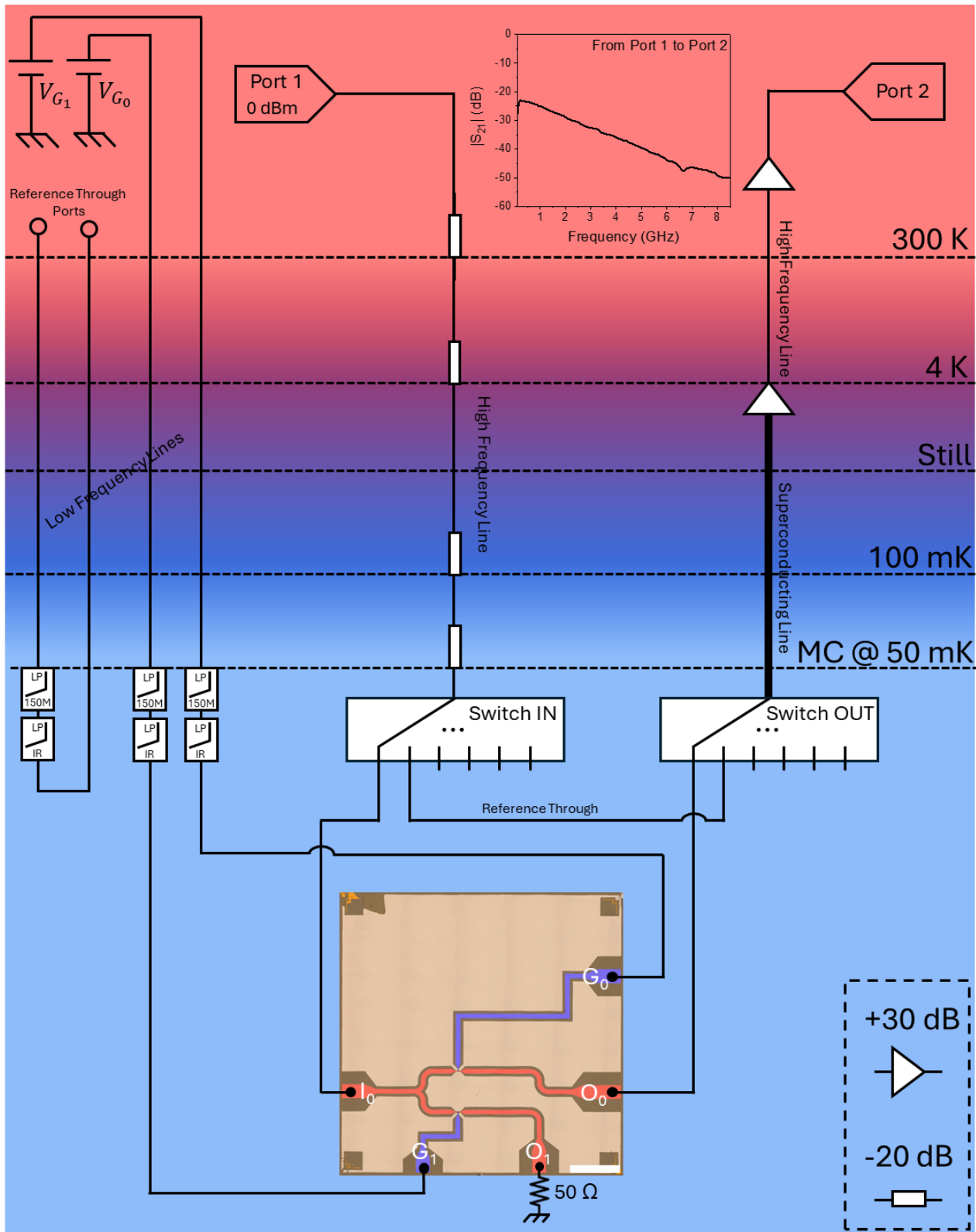
268

269

270

271

272



273

274 **Figure S18: VHF-UHF measurement setup used to characterize the frequency-resolved**
 275 **electrical behavior of the μ wave superconducting 112O analog demultiplexer.** The input power
 276 ($P_{IN} = 0 \text{ dBm}$) supplied by the Port₁ was attenuated by -80 dB then provided to the demultiplexer
 277 input I_0 . The line O_0 output power was amplified at 4 K (+30 dB) and 300 K (+30 dB) then
 278 provided to Port₂, while line O_1 was terminated with 50 Ω . The output power was measured
 279 changing the gate settings. Reference through ports were used to collect the trough calibration data.
 280 The system was operated up to a maximum operation frequency of 8.5 GHz at 50 mK.

281 **3. Materials and Manufacturing Methods**

282 **3.1 Materials and Chemicals**

283 GaAs wafers (2'' diameter, (100) orientation, $\rho=5.9\times 10^7 \Omega\times\text{cm}$) were purchased from Wafer
284 Technology LTD. Materials used for the Molecular Beam Epitaxy growth (Gallium 7N5,
285 Aluminum 6N5, Indium 7N5, and Arsenic 7N5) were purchased from Azelis S.A.. Acetone (ACE,
286 ULSI electric grade, MicroChemicals), 2-propanol (IPA, ULSI electric grade, MicroChemicals),
287 S1805 G2 Positive Photoresist (S1805, Microposit, positive photoresist), AR-P 679.04 (AllResist,
288 positive e-beam resist), MF319 Developer (MF319, Microposit), AR 600-56 Developer (AR 600-
289 56, AllResist), AR600-71 (AllResist, remover for photo- and e-beam resist), Aluminum Etchant
290 Type D (Transene), Phosphoric acid (H_3PO_4 , Sigma Aldrich, semiconductor grade $\geq 85\%$ in water),
291 Hydrogen peroxide (H_2O_2 , Carlo Erba Reagents, RSE-For electronic use-Stabilized, 30% in water),
292 Nitrogen (N_2 , 5.0, Nippon Gases) was provided by the Clean Room Facility of the National
293 Enterprise for nanoScience and nanotechnology (NEST, Pisa, Italy). Diammonium sulfide
294 $(\text{NH}_4)_2\text{S}$, Carlo Erba Reagents, 20% in water) was provided by the Chemical Lab Facility of the
295 NEST. Sulfur pieces (S, Alfa Aesar, 99.999% pure) was purchased from Carlo Erba Reagents S.r.l.
296 Aluminum pellets (99.999% pure) were purchased from Kurt J. Lesker Company. Aqueous
297 solutions were prepared using deionized water (DIW, $15.0 \text{ M}\Omega\times\text{cm}$) filtered by Elix® (Merck
298 Millipore) provided by the Clean Room Facility of the NEST.

299

300 **3.2 InAsOI Heterostructure Growth via Molecular Beam Epitaxy**

301 InAsOI was grown on semi-insulating GaAs (100) substrates using solid-source Molecular Beam
302 Epitaxy (MBE, Compact 21 DZ, Riber). Starting from the GaAs substrate, the sequence of the layer
303 structure includes a 200 nm-thick GaAs layer, a 200 nm-thick GaAs/ $\text{Al}_{0.16}\text{Ga}_{0.84}\text{As}$ superlattice, a
304 200 nm-thick GaAs layer, a 1.250 μm -thick step-graded $\text{In}_x\text{Al}_{1-x}\text{As}$ metamorphic buffer (with X
305 increasing from 0.15 to 0.81), a 400 nm-thick $\text{In}_{0.84}\text{Al}_{0.16}\text{As}$ overshoot layer, and a 100 nm-thick
306 InAs layer. The GaAs layer and the GaAs/ $\text{Al}_{0.16}\text{Ga}_{0.84}\text{As}$ superlattice below the $\text{In}_x\text{Al}_{1-x}\text{As}$ buffer
307 layer are grown to planarize the starting GaAs surface and to reduce surface roughness caused by
308 the oxide desorption process. Both are grown with a group V/III beam flux ratio of 6.

309 The metamorphic buffer consists of two regions with different misfit gradients. The first $\text{In}_x\text{Al}_{1-x}$ -
310 As region is composed of twelve 50 nm-thick layers with X ramping from 0.15 to 0.58. The
311 second $\text{In}_x\text{Al}_{1-x}\text{As}$ region is composed of twelve 50 nm-thick layers with X ramping from 0.58 to
312 0.81. The Al flux was kept constant during the buffer layer growth, while the In flux was increased
313 at each step without growth interruptions. At the end of the buffer, the overshoot layer was grown to
314 increase the strain relaxation of the $\text{In}_x\text{Al}_{1-x}\text{As}$ metamorphic layer [40]. The As flux was adjusted

315 during the growth of the metamorphic buffer and the overshoot layer to keep a constant group V/III
316 beam flux ratio of 8. The InAs layer was growth with a group V/III beam flux ratio of 8 and a
317 growth rate of 0.96 $\mu\text{m}/\text{h}$. The GaAs layer and GaAs/AlGaAs superlattice are grown at $600\text{ }^\circ\text{C} \pm 5$
318 $^\circ\text{C}$. The metamorphic buffer and the overshoot layers were grown at optimized substrate
319 temperatures of $320\text{ }^\circ\text{C} \pm 5\text{ }^\circ\text{C}$. The InAs epilayer was grown at $480 \pm 5\text{ }^\circ\text{C}$.

320

321 In the following, all wetting steps were performed in cleaned glass Beckers using stainless steel
322 tweezers provided with carbon tips. Teflon-coated tweezers were used for all the steps requiring
323 acid or base solutions. The Julabo TW2 was used to heat the solution to a specific temperature.

324

325 **3.3 InAsOI Josephson Field Effect Transistor Fabrication**

326 Superconductor Deposition on InAsOI

327 InAsOI substrates were cut into square samples ($7 \times 7\text{ mm} \times \text{mm}$) and sonicated in ACE and IPA for 5
328 min to remove GaAs dusts. The air-exposed InAs surface was etched from native InAs oxide
329 (InAsO_x) and passivated with S-termination by dipping the InAsOI samples in a $(\text{NH}_4)_2\text{S}_x$ solution
330 ($290\text{ mM } (\text{NH}_4)_2\text{S}$ and 300 mM S in DIW) at 45°C for 90 s. The S-terminated InAsOI samples were
331 then rinsed twice in DIW for 30 s and immediately loaded ($\sim 90\text{ s}$ exposure time in the air) into the
332 load-lock vacuum chamber of an e-beam evaporator (acceleration voltage 7 kV). Samples were
333 transferred into the deposition chamber, where a 100-nm-thick Al layer was deposited at a rate of 2
334 A/s at a residual chamber pressure of $1\text{E}-8 \div 5\text{E}-9\text{ Torr}$.

335 InAsOI MESA Fabrication

336 After Al deposition, a layer of S1805 positive photoresist was spin-coated at 5000 RPM for 60 s
337 (spin coating acceleration of 5000 RPM/s) and soft-baked at $115\text{ }^\circ\text{C}$ for 60 s. The resist was then
338 exposed via direct writing UV lithography (UVL, DMO, ML3 laser writer, $\lambda=385\text{ nm}$) with a dose
339 of 60 mJcm^{-2} , resolution of $0.6\text{ }\mu\text{m}$, high exposure quality, and laser-assisted real-time focus
340 correction to define the MESA geometry. Unless otherwise stated, all the rinsing steps were
341 performed at room temperature (RT, $21\text{ }^\circ\text{C}$). The UV-exposed samples were developed in MF319
342 for 45 s with soft agitation to remove exposed photoresist, then rinsed in DIW for 30 s to stop the
343 development and dried with N_2 . The exposed Al layer was removed by dipping the sample in Al
344 Etchant Type D at $40\text{ }^\circ\text{C}$ for 65 seconds with soft agitation, then rinsed in DIW for 30 seconds to
345 stop the etching and dried with N_2 . The exposed InAs epilayer was etched by dipping the samples in
346 a $\text{H}_3\text{PO}_4:\text{H}_2\text{O}_2$ solution ($348\text{ mM H}_3\text{PO}_4$, $305\text{ mM H}_2\text{O}_2$ in DIW) for 60 s with soft agitation, then
347 rinsed in DIW for 30 s to stop the etching and dried with N_2 . Eventually, the photoresist was

348 removed by rinsing the InAsOI samples in ACE at 60 °C for 5 minutes and IPA for 60 s, then dried
349 with N₂. At the end of this step, the width (W) of the JoFET was set to 5 μm.

350 Markers Deposition for Aligned Steps

351 After MESA fabrication, a layer of AR-P 679.04 positive e-beam resist was spin-coated at 4000
352 RPM for 60 s (spin coating acceleration of 10000 RPM/s) and soft-baked at 160 °C for 60 s. The
353 resist was then exposed via UVL-marker-aligned e-beam lithography (EBL, ZEISS, Ultra Plus)
354 with a dose of 350 μCcm⁻², voltage acceleration of 30 kV, aperture of 7.5 or 120 μm, line step size
355 of 1 nm or 200 nm, to define EBL-markers for the next alignment steps. The electron-exposed
356 samples were developed in AR 600-56 for 90 s with soft agitation to remove the exposed e-beam
357 resist, then rinsed in IPA for 30 s to stop the development and dried with N₂. The samples were
358 loaded into a thermal evaporator (Sistec prototype) where a 10/50-nm-thick Ti/Au bilayer was
359 deposited at a rate of 1 Å/s at a residual chamber pressure of 2E-6 mbar. The deposited film was
360 lifted-off in ACE at 70 °C for 5 min with strong agitation, then rinsed in IPA for 60 s, and dried
361 with N₂.

362 Aligned Josephson Junction Fabrication

363 After EBL marker definition, a layer of AR-P 679.04 positive e-beam resist was spin-coated at 4000
364 RPM for 60 s (spin coating acceleration of 10000 RPM/s) and soft-baked at 160 °C for 60 s. The
365 resist was then exposed via marker-aligned EBL (ZEISS, Ultra Plus) with a dose of 350 μCcm⁻²,
366 voltage acceleration of 30 kV, aperture of 7.5 μm, and line step size of 1 nm to define the Josephson
367 junction length (L_{JJ}). The electron-exposed samples were developed in AR 600-56 for 90 s with soft
368 agitation to remove the exposed e-beam resist, then rinsed in IPA for 30 s to stop the development
369 and dried with N₂. Subsequently, the exposed Al layer was removed by dipping the sample in Al
370 Etchant Type D at 40 °C for 65 seconds with soft agitation, then rinsed in DIW for 30 seconds to
371 stop the etching and dried with N₂. Eventually, the e-beam resist was removed by rinsing the
372 InAsOI samples in ACE at 70 °C for 5 min, IPA for 60 s, and dried with N₂. At the end of this step,
373 we achieved L_{JJ} ranging from 500 to 1250 nm.

374 Gate Insulator Deposition

375 Samples were loaded into the vacuum chamber of an Atomic Layer Deposition system (ALD,
376 Oxford Instruments, OpAL) where the gate insulator was uniformly deposited at a temperature of
377 130 °C. Tetrakis(ethylmethylamino)hafnium (TEMAH) and H₂O were used as HfO₂ precursors,
378 while Ar was used as carrier gas. Ar bubbling was also involved to increase the volatility of
379 TEMAH. After reaching a base pressure of ~3-4 mTorr, the chamber pressure was increased to
380 ~350 mTorr injecting Ar. The deposition process follows 4 steps: (i) TEMAH dose, (ii) TEMAH
381 purge, (iii) H₂O dose, and (iv) H₂O purge:

- 382 (i) TEMAH dose: TEMAH valve on; Ar bubbler: 250 sccm; Ar purge: 10 sccm; step
383 duration: 0.9 s.
- 384 (ii) TEMAH: purge: TEMAH valve off; Ar purge: 250 sccm; step duration: 110 s.
- 385 (iii) H₂O dose: H₂O valve on; Ar purge: 10 sccm; step duration: 0.03 s.
- 386 (iv) H₂O purge: H₂O valve off; Ar purge: 250 sccm; step duration: 90 s.

387 We performed 250 ALD cycles to achieve a total insulator thickness of ~31 nm [41]. Eventually,
388 the chamber was pumped to reach a base pressure of ~3-4 mTorr and then vented using N₂. The
389 entire process takes ~16 h.

390 Aligned Metal Gate Deposition

391 After gate insulator deposition, a layer of AR-P 679.04 positive e-beam resist was spin-coated at
392 4000 RPM for 60 s (spin coating acceleration of 10000 RPM/s) and soft-baked at 160 °C for 60 s.
393 The resist was then exposed via marker-aligned EBL (ZEISS, Ultra Plus) with a dose of 350 μCcm^{-2} ,
394 voltage acceleration of 30 kV, aperture of 7.5 or 120 μm , line step size of 1 or 200 nm, to define
395 the JoFET gate length (L_G). The electron-exposed samples were developed in AR 600-56 for 90 s
396 with soft agitation to remove the exposed e-beam resist, then rinsed in IPA for 30 s to stop the
397 development and dried with N₂. Samples were mounted into an e-beam evaporator (acceleration
398 voltage 7 kV), where a 10/100-nm-thick Ti/Al bilayer was deposited at a rate of 0.5/2 A/s with a tilt
399 angle of 53° at a residual chamber pressure of 1E-8 ÷ 1E-9 Torr. The deposited film was lifted-off
400 in AR600-71 at 80 °C for 5 min with strong agitation, then rinsed in IPA for 30 s, and dried with
401 N₂.

402
403
404
405
406
407
408
409
410
411
412
413
414
415

416 **3.4 InAsOI Superconducting 1180 Demultiplexer Fabrication**

417 Superconductor Deposition on InAsOI

418 This step was performed in accordance with what is reported in Section 3.3 “InAsOI Josephson
419 Field Effect Transistor Fabrication: Superconductor Deposition on InAsOI”.

420 InAsOI MESA Fabrication

421 This step was performed in accordance with what is reported in Section 3.3 “InAsOI Josephson
422 Field Effect Transistor Fabrication: InAsOI MESA Fabrication”.

423 Aligned Josephson Junction Fabrication

424 This step was performed in accordance with what is reported in Section 3.3 “InAsOI Josephson
425 Field Effect Transistor Fabrication: Aligned Josephson Junction Fabrication” using UVL markers
426 defined in the previous step instead of EBL markers.

427 Gate Insulator Deposition

428 This step was performed in accordance with what is reported in Section 3.3 “InAsOI Josephson
429 Field Effect Transistor Fabrication: Gate Insulator Deposition”.

430 Aligned Metal Gate Deposition

431 After the insulator deposition, samples were removed from the ALD system and heated up to 170
432 °C for 180 s to desorb adsorbed water molecules from air. After that, a LOR3A/S1805 bilayer was
433 deposited. LOR3A was spin-coated at 4000 RPM for 60 s (spin coating acceleration of 4000
434 RPM/s) and soft-baked at 170 °C for 180 s. The LOR3A spin coating and soft bake procedure was
435 performed 2 times to increase the LOR3A thickness. Then, S1805 positive photoresist was spin-
436 coated at 5000 RPM for 60 s (spin coating acceleration of 5000 RPM/s) and soft-baked at 115 °C
437 for 60 s. The resist was exposed via direct writing UV lithography (UVL, DMO, ML3 laser writer,
438 $\lambda=385$ nm) with a dose of 60 mJcm⁻², resolution of 0.6 μ m, high exposure quality, and no real-time
439 focus correction to define gate pattern. The UV-exposed samples were developed in MF319 for 120
440 s with soft agitation to remove exposed S1805 and the underlying layer of LOR3A, then rinsed in
441 DIW for 30 s to stop the development and dried with N₂.

442 Samples were mounted into an e-beam evaporator (acceleration voltage 7 kV), where a 10/250-nm-
443 thick Ti/Al bilayer was deposited at a rate of 0.5/2 A/s at a residual chamber pressure of 1E-8 ÷ 1E-
444 9 Torr. The evaporation was performed with the following tilt angles: (i) 0° for 10 nm Ti and 100
445 nm Al; (ii) -45° for 75 nm Al; (iii) 45° for 75 nm Al. The deposited film was lifted-off in AR600-71
446 at 80 °C for 5 min with strong agitation, then rinsed in IPA for 30 s, and dried with N₂.

447 Compared to the electron beam-aligned lithographic process involved in fabrication of the aligned
448 metallic gates in InAsOI-based JoFETs, the use of an UV-aligned lithographic step to fabricate

449 aligned metallic gates and traces in the superconducting demultiplexer allows to reduce the time
450 required for the manufacturing step.

451
452 **3.5 InAsOI μ wave Superconducting 1120 Demultiplexer Fabrication**

453 *Superconductor Deposition on InAsOI*

454 This step was performed in accordance with what is reported in Section 3.3 “InAsOI Josephson
455 Field Effect Transistor Fabrication: Superconductor Deposition on InAsOI”.

456 *InAsOI MESA Fabrication*

457 This step was performed in accordance with what is reported in Section 3.3 “InAsOI Josephson
458 Field Effect Transistor Fabrication: InAsOI MESA Fabrication”.

459 *Aligned Josephson Junction Fabrication*

460 This step was performed in accordance with what is reported in Section 3.3 “InAsOI Josephson
461 Field Effect Transistor Fabrication: Aligned Josephson Junction Fabrication” using UVL markers
462 defined in the previous step instead of EBL markers.

463 *Gate Insulator Deposition*

464 This step was performed in accordance with what is reported in Section 3.3 “InAsOI Josephson
465 Field Effect Transistor Fabrication: Gate Insulator Deposition”.

466 *Aligned Metal Gate Deposition*

467 After gate insulator deposition, a layer of AR-P 679.04 positive e-beam resist was spin-coated at
468 4000 RPM for 60 s (spin coating acceleration of 10000 RPM/s) and soft-baked at 160 °C for 60 s.
469 The resist was then exposed via marker-aligned EBL (ZEISS, Ultra Plus) with a dose of 350 μCcm^{-2} ,
470 voltage acceleration of 30 kV, aperture of 7.5 or 120 μm , line step size of 1 or 200 nm, to define
471 the JoFET gate length (L_G). The electron-exposed samples were developed in AR 600-56 for 90 s
472 with soft agitation to remove the exposed e-beam resist, then rinsed in IPA for 30 s to stop the
473 development and dried with N_2 . Samples were mounted into an e-beam evaporator (acceleration
474 voltage 7 kV), where a 10/250-nm-thick Ti/Al bilayer was deposited at a rate of 0.5/2 A/s at a
475 residual chamber pressure of $1\text{E}-8 \div 1\text{E}-9$ Torr. The evaporation was performed with the following
476 tilt angles: (i) 0° for 10 nm Ti and 100 nm Al; (ii) -45° for 75 nm Al; (iii) 45° for 75 nm Al. The
477 deposited film was lifted-off in AR600-71 at 80 °C for 5 min with strong agitation, then rinsed in
478 IPA for 30 s, and dried with N_2 .

479
480
481
482

483 **3.6 InAsOI Hall Bars Fabrication**

484 *Metal Deposition on InAsOI*

485 This step was performed in accordance with what is reported in Section 3.3 “InAsOI Josephson
486 Field Effect Transistor Fabrication: Superconductor Deposition on InAsOI”.

487 *Metal Pads Fabrication*

488 After Al deposition, a layer of S1805 positive photoresist was spin-coated at 5000 RPM for 60 s
489 (spin coating acceleration of 5000 RPM/s) and soft-baked at 115 °C for 60 s. Then, the photoresist
490 was exposed via direct writing UV lithography (DMO ML3 laser writer, $\lambda=385$ nm) with a dose of
491 60 mJcm^{-2} , resolution of 0.6 μm , high exposure quality, and laser-assisted real-time focus correction
492 to define the Al geometry for fabrication of 6-terminals Hall Bars. Unless stated otherwise, all the
493 rinsing steps were performed at room temperature (RT, 21 °C). The UV-exposed samples were
494 developed in MF319 for 45 s with soft agitation to remove exposed photoresist, then rinsed in DIW
495 for 30 s to stop the development and dried with N_2 . The exposed Al layer was removed by dipping
496 the sample in Al Etchant Type D at 40 °C for 65 seconds with soft agitation, then rinsed in DIW for
497 30 seconds to stop the etching and dried with N_2 . Eventually, the photoresist was removed by
498 rinsing the InAsOI samples in ACE at 60 °C for 5 min and IPA for 60 s, which was then dried with
499 N_2 .

500 *InAsOI MESA Fabrication*

501 A layer of S1805 positive photoresist was spin-coated at 5000 RPM for 60 s (spin coating
502 acceleration of 5000 RPM/s) and soft-baked at 115 °C for 60 s. Then, the photoresist was exposed
503 via a second marker-aligned direct writing UV lithography (DMO ML3 laser writer, $\lambda=385$ nm)
504 with a dose of 60 mJcm^{-2} , resolution of 0.6 μm , high exposure quality, and no real-time focus
505 correction, to define the InAs/InAlAs geometry for fabrication of Hall Bars. The UV-exposed
506 samples were developed in MF319 for 45 s with soft agitation to remove exposed photoresist, then
507 rinsed in DIW for 30 s to stop the development and dried with N_2 . Then, the exposed InAs epilayer
508 was etched by dipping the samples in a $\text{H}_3\text{PO}_4:\text{H}_2\text{O}_2$ solution (348 mM H_3PO_4 , 305 mM H_2O_2 in
509 DIW) for 60 s with soft agitation, then rinsed in DIW for 30 s to stop the etching and dried with N_2 .
510 Eventually, the photoresist was removed by rinsing the InAsOI samples in ACE at 60 °C for 5 min,
511 IPA for 60 s, and drying with N_2 . We fabricated 6-contact Hall bars with a width of 100 μm ,
512 source-to-drain length of 500 μm , and probe-to-probe length of 250 μm .

513

514

515

516

517 **3.7 Sample Bonding via Wire Wedge Bonding**

518 All the fabricated samples were provided with bonding pads ranging from 150×150 to 200×200
519 $\mu\text{m} \times \mu\text{m}$ and then used to connect the device with the chip carrier. Samples were glued using a small
520 drop of AR-P 679.04, then left dry at RT for 1 hour on a 24-pin dual-in-line (DIL) chip carrier.
521 Samples were bonded via wire wedge bonding (MP iBond5000 Wedge) using an Al/Si wire (1%,
522 25 μm wire diameter), leaving the user-bonder and the DIL chip carrier electrically connected to the
523 ground.

524
525 **4. Characterization Methods**

526 **4.1 Morphological Characterization**

527 *via Scanning Electron Microscopy*

528 Top view morphological characterization of JJs was carried out via scanning electron microscopy
529 (SEM, ZEISS Merlin) with 5 kV acceleration voltage, 178 pA filament current, back scattered
530 electron relevator, at different magnifications (2.5k and 50k).

531 *via Optical Microscopy*

532 Optical microscopy (Leica, DM8000 M, provided with LEICA MC190 HD camera) was used to
533 verify all the steps without photoresist. An optical microscope (Nikon, Eclipse ME600, provided
534 with Nikon TV Lens C-0.6 \times and a UV filter) was used to evaluate all the steps involving the
535 photoresist.

536 *via Atomic Force Microscopy*

537 Atomic force microscopy (AFM, Bruker, DIMENSION edge with ScanAsyst provided with an
538 ASYLEC-01-R2 tip - silicon tip Ti/Ir coated, $f_0=75$ kHz, $k=2.8$ N/m - in tapping mode) was used to
539 evaluate the profile of the fabricated JoFETs. All the AFM photos were processed using Gwyddion.

540

541

542

543

544

545

546

547

548

549

550

551 **4.2 Electrical Characterization**

552 ***4.2.1 Cryogenic Electrical Characterization of InAsOI Josephson Field Effect Transistors***

553 *DC Electrical Characterization*

554 Electrical characterization of JoFETs was carried out by measuring 4-wires V-I curves at 50 mK.
555 Out-of-plane magnetic field (B_{\perp}) was used to maximize the switching current at 0 gate voltage, then
556 maintained for all the characterization. The sample was mounted in contact with the mixing
557 chamber (MC) plate of the Leiden CF-CS81-1400 cryostat. Electrical configuration of the
558 measurement setup is shown in **Figure S3**. Source-drain current (I_{DS}) was injected applying an
559 increasing DC voltage (Voltage Source, YOKOGAWA GS200) over an input series resistor ($R=1$
560 $M\Omega$) at least 100 times larger than the total resistance of the remaining measurement setup. The
561 voltage drop across the probe contacts (V_{DS}) was amplified (Voltage Amplifier, DL Instruments
562 1201, Gain = 10k, High pass filter = DC, Low pass filter = 100 Hz) and read (Multimeter, Agilent,
563 34410A, NPLC = 2). The gate-source voltage (V_{GS}) was changed between 0 and -4.5 V (SMU,
564 Keithley, 2400).

565 The switching current (I_S) was estimated as the last applied current in the V-I curve before reading a
566 voltage drop different from the noise floor, while the normal state resistance (R_N) was evaluated as
567 the angular coefficient of the V-I linear best fitting curve for $I > I_S$.

568 Gate current leakage was evaluated measuring the gate I-V curve (with source terminal grounded
569 and the other terminals left open) upon application of an increasing voltage (SMU, Keithley, 2400,
570 absolute voltage step = 100 mV, step delay = 1 s) and collecting the flowing current (TIA, FEMTO,
571 DDPCA-300, gain = 10^{10} V/A, rise time = fast; Multimeter, Agilent, 34410A, NPLC = 2).

572 *Real-Time AC VHF Electrical Characterization*

573 Real-time VHF AC electrical characterization of JoFETs was carried out using a lock-in amplifier
574 (Lock-in, Zurich Instruments, UHF Lock-in Amplifier 600 MHz, 1.8 GSa/s) at 100 mK. The output
575 port of the lock-in (Port1, power 0 dBm, frequency 100 MHz) was attenuated by -20 dB at 300 K, -
576 20 dB at the 4K plate, -20 dB at the 100 mK plate, and -20 dB at the mixing chamber (MC) plate,
577 then low-pass filtered (cut-off frequency of 12 GHz) and IR-filtered with an Ecosorb filter, and
578 provided as input power of the JoFET to the drain terminal. Then, the signal line connected to the
579 source terminal was attenuated amplified by +30 dB at 4 K plate (Low Noise Factory, LNF-
580 LNC03_14A), +30 dB at 300 K (MITEQ, LNA-30-00101200-42-20P), and provided to the input
581 port (Port2, averages = 50) of the lock-in. A wave function generator (Agilent 33220A) was used to
582 provide the control switching signal to the gate terminal of the JoFET. The output port of the signal
583 generator ($V_{DC} = -2.25$ V, $V_{PP} = 4.5$ V, frequency from 1 to 100 kHz) was then low-pass filtered

584 (cut-off frequency of 150 MHz) and IR-filtered with an Ecosorb filter, then provided as control
585 signal of the JoFET to the gate terminal. We collected the voltage measured by the lock-in amplifier
586 in Scope mode at different switching control frequencies.

587 *4.2.2 Cryogenic Electrical Characterization of the Superconducting I180 Analog Demultiplexer*

588 DC Electrical Characterization

589 DC electrical characterization of the signal lines was carried out by measuring 4-wires V-I curves at
590 50 mK. The sample was mounted in contact with the mixing chamber (MC) plate of the Oxford
591 Triton 200. Electrical configuration of the measurement setup is shown in **Figure S7**. Signal line
592 input current (I_{IN}) was injected into the I_0 terminal applying an increasing DC voltage (Voltage
593 Source, YOKOGAWA GS200) over an input series resistor ($R=1\text{ M}\Omega$) at least 100 times larger
594 than the total resistance of the remaining measurement setup. The voltage drop across the probe
595 contacts of the signal line (V_{Line}) was amplified (Voltage Amplifier, DL Instruments 1201, Gain =
596 10k, High pass filter = DC, Low pass filter = 100 Hz) and read (Multimeter, Agilent, 34410A,
597 NPLC = 1). Gate control voltages (V_{Gij}) were changed between 0 and -4.5 V (SMU, Keithley,
598 2400). Terminals of other lines were left open during the measurement.

599 Each signal line features 3 different I_S of the 3 JoFETs along the path. I_S were estimated as the last
600 applied current in the V-I curve before reading a step in the voltage drop, while the signal line
601 resistance (R) was evaluated as the angular coefficient of the V-I linear best fitting curve for input
602 currents larger than the third switching current detected.

603 Gate current leakage was evaluated measuring the gate I-V curve (with I_0 terminal grounded and the
604 other terminals left open) upon application of an increasing voltage (SMU, Keithley, 2400, absolute
605 voltage step = 100 mV, step delay = 1 s) and collecting the flowing current (TIA, DL, 1211,
606 gain= 10^{10} V/A, rise time = 0.3 s; Multimeter, Agilent, 34410A, NPLC = 2).

607 Real-Time Electrical Characterization

608 Real-time electrical characterization of the signal lines I_0O_4 and I_0O_6 was carried out by measuring
609 4-wires V-I curves at 50 mK. Electrical configuration of the measurement setup is shown in **Figure**
610 **S10**. Signal line input current (I_{IN}) of $\sim 1.3\ \mu\text{A}$ was injected into the I_0 terminal applying an DC
611 voltage of 1.3 V (Voltage Source, YOKOGAWA GS200) over an input series resistor ($R=1\text{ M}\Omega$) at
612 least 100 times larger than the total resistance of the remaining measurement setup. Voltage drops
613 across the probe contacts of each signal line (V_{Line}) was amplified (Voltage Amplifier, DL
614 Instruments 1201, Gain = 500, High pass filter = DC, Low pass filter = MAX) and real-time
615 collected (Oscilloscope, Tektronix, TDS2024B, averages = 128). The current flowing in each signal

616 line (I_{Line}) was also measured (TIA, DL, 1211, gain= 10^5 V/A, rise time = min; Oscilloscope,
617 Tektronix, TDS2024B, averages = 128). Gate control voltages (V_{Gij}) were changed between 0 and -
618 4.5 V (SMU, Keithley, 2400). Terminals of other lines were left open during the measurement. The
619 cryostat's wires account as a load resistance of $\sim 200 \Omega$.

620 Real-time VLF AC electrical characterization of the signal line I_0O_4 was carried out by measuring
621 4-wires V-I curves at 50 mK. A signal line input current (I_{IN}) with 1 kHz frequency and peak-to-
622 peak values from 2 to 16 μA was injected into the I_0 terminal applying an AC voltage
623 (Wavefunction Generator, Agilent, 33220A) over an input series resistor ($R=1 \text{ M}\Omega$) at least 100
624 times larger than the total resistance of the remaining measurement setup. Voltage drops across the
625 probe contacts of the signal line I_0O_4 was amplified (Voltage Amplifier, DL Instruments 1201, Gain
626 = 500, High pass filter = DC, Low pass filter = MAX) and real-time collected (Oscilloscope,
627 Tektronix, TDS2024B, averages = 128). Gate control terminals and other signal line terminals were
628 left open during the measurement.

629 VLF-VHF AC Electrical Characterization

630 VLF-HF AC electrical characterization of signal lines I_0O_4 and I_0O_6 was carried using a lock-in
631 amplifier (Lock-in, Zurich Instruments, UHF Lock-in Amplifier 600 MHz, 1.8 GSa/s) at 50 and
632 1650 mK. Electrical configuration of the measurement setup is shown in [Figure S11](#). The output
633 port of the lock-in (Port1, power -20 dBm, frequency 10 kHz - 10 MHz) was attenuated by -50 dB
634 at 300 K and -10 dB on the mixing chamber (MC), then provided as input power of the
635 demultiplexer to the I_0 terminal. Then, the signal line output power was attenuated by -10 dB on the
636 MC, amplified by +80 dB at 300 K (FEMTO, HSA-X-I-2-40), and provided to input port (Port2,
637 averages = 25) of the lock-in. When measuring the signal line I_0O_4 , the I_0O_6 was terminated to 50
638 Ω , and vice versa. To retrieve the “through” calibration file of the measurement system, two
639 cryostat ports were connected with a feed-through connector on the MC and provided with the same
640 attenuation and amplification of the measurement lines. For both the signal line ($r_{line+sys}$) and
641 calibration (r_{sys}) measurements, we collected the magnitude of the voltage measured by the lock-in
642 (r). The forward power gain scattering parameter, i.e., the $|S_{21}|$ (dB), of the signal line was obtained
643 as $|S_{21}| = 20 \log(r_{line+sys}/r_{sys})$. Gate control voltages (V_{Gij}) were changed between 0 and -4.5 V (SMU,
644 Keithley, 2400).

645 MF-VHF AC electrical characterization of signal lines I_0O_4 and I_0O_6 was carried using a vector
646 network analyzer (VNA, PicoTech, PicoVNA 108) at 50 mK. Electrical configuration of the
647 measurement setup is shown in [Figure S11](#). The Port1 of the VNA (power -20 dBm, frequency 300
648 kHz - 100 MHz) was attenuated by -50 dB at 300 K and -10 dB on the mixing chamber (MC), then

649 provided as input power of the demultiplexer to the I_0 terminal. Then, the signal line output power
650 was attenuated by -10 dB on the MC, amplified by +80 dB at 300 K (FEMTO, HSA-X-I-2-40), and
651 provided to the Port2 (bandwidth = 1 kHz) of the VNA. When measuring the signal line I_0O_4 , the
652 I_0O_6 was terminated to 50Ω , and vice versa. To retrieve the “through” calibration file of the
653 measurement system, two cryostat ports were connected with a feed-through connector on the MC
654 and provided with the same attenuation and amplification of the measurement lines. For both the
655 signal line ($|S_{21}|_{\text{line+sys}}$) and calibration ($|S_{21}|_{\text{sys}}$) measurements, we collected the $|S_{21}|$ parameter. The
656 $|S_{21}|$ (dB) of the signal line was obtained as $|S_{21}|_{\text{line}} = |S_{21}|_{\text{line+sys}} - |S_{21}|_{\text{sys}}$. Gate control voltages (V_{Gij})
657 were changed between 0 and -4.5 V (SMU, Keithley, 2400).

658 ***4.2.3 Cryogenic Electrical Characterization of the μ wave Superconducting $1I2O$ Analog***

659 ***Demultiplexer***

660 *DC Electrical Characterization*

661 DC electrical characterization of the signal lines was carried out by measuring 4-wires V-I curves at
662 50 mK. The sample was mounted in contact with the mixing chamber (MC) plate of the Oxford
663 Triton 200. Electrical configuration of the measurement setup is similar to that shown in **Figure S7**.
664 Signal line input current (I_{IN}) was injected into the I_0 terminal applying an increasing DC voltage
665 (Voltage Source, YOKOGAWA GS200) over an input series resistor ($R= 1 \text{ M}\Omega$) at least 100 times
666 larger than the total resistance of the remaining measurement setup. The voltage drop across the
667 probe contacts of the signal line (V_{Line}) was amplified (Voltage Amplifier, DL Instruments 1201,
668 Gain = 10k, High pass filter = DC, Low pass filter = 100 Hz) and read (Multimeter, Agilent,
669 34410A, NPLC = 1). Gate control voltages (V_{Gij}) were changed between 0 and -4.5 V (SMU,
670 Keithley, 2400). Terminals of other lines were left open during the measurement.

671 The switching current (I_S) was estimated as the last applied current in the V-I curve before reading a
672 voltage drop different from the noise floor, while the normal state resistance (R_N) was evaluated as
673 the angular coefficient of the V-I linear best fitting curve for $I > I_S$.

674 Gate current leakage was evaluated measuring the gate I-V curve (with I_0 terminal grounded and the
675 other terminals left open) upon application of an increasing voltage (SMU, Keithley, 2400, absolute
676 voltage step = 100 mV, step delay = 1 s) and collecting the flowing current (TIA, DL, 1211,
677 gain= 10^{10} V/A, rise time = 0.3 s; Multimeter, Agilent, 34410A, NPLC = 2).

678 *VHF-UHF AC Electrical Characterization*

679 VHF-UHF AC electrical characterization of signal line I_0O_0 was carried using a vector network
680 analyzer (VNA, PicoTech, PicoVNA 108) at 50 mK. Electrical configuration of the measurement

681 setup is shown in **Figure S18**. The Port1 of the VNA (power 0 dBm, frequency 300 kHz - 8.5 GHz)
682 was attenuated by -20 dB at 300 K, -20 dB at 4K, -20 dB at 100 mK, and -20 dB on the mixing
683 chamber (MC), then provided as input power of the demultiplexer to the I_0 terminal. The output line
684 O_0 power was amplified by +30 dB at 4 K (Low Noise Factory, LNF-LNC0.3_14A), +30 dB at 300
685 K (MITEQ, LNA-30-00101200-42-20P) and provided to the Port2 (bandwidth = 1 kHz, averages =
686 10) of the VNA. O_6 was terminated to 50Ω at the MC stage. To retrieve the “through” calibration
687 file of the measurement system, a reference “gold standard” through was mounted on the MC and
688 provided with the same attenuation and amplification of the measurement lines thanks to the input
689 and output cryogenic switches mounted at the MC stage. For both the signal line ($|S_{21}|_{\text{line+sys}}$) and
690 calibration ($|S_{21}|_{\text{sys}}$) measurements, we collected the $|S_{21}|$ parameter. The $|S_{21}|$ of the signal line was
691 obtained as $|S_{21}|_{\text{line}} = |S_{21}|_{\text{line+sys}} - |S_{21}|_{\text{sys}}$. Gate control voltages (V_{Gi}) were changed between 0 and -
692 4.5 V (SMU, Keithley, 2400).

693

694 **4.2.4 Cryogenic and Room Temperature Electrical Characterization of InAsOI**

695 Hall measurements were performed on Hall Bars (HBs) with a standard lock-in-amplifier-based
696 technique. The first lock-in amplifier oscillator voltage ($V_{\text{OSC,RMS}} = 1 \text{ V}$, $f = 13.321 \text{ Hz}$) was applied
697 across a series resistor ($R=10 \text{ M}\Omega$) at least 100 times larger than the total resistance of the
698 remaining measurement setup to use the AC current ($I_{\text{OSC,RMS}}$). The AC current is injected into the
699 sample's source contact. In contrast, the flowing current is measured with the drain contact, and the
700 second lock-in amplifier measures the voltage drop's magnitude and phase across two other
701 contacts. The contacts are manually switched to inject the current and measure the voltage. The Hall
702 measurements were performed in three steps. In the first step, the resistivity (ρ) is calculated at zero
703 magnetic fields using the formula $\rho = R_{xx} \times \frac{W \times t}{l}$, where R_{xx} is the resistance measured between
704 longitudinal (same-side) contacts of the HB for a current passing between source and drain, W is the
705 HB width, t is the InAs thickness, and l is the distance between probe contacts. In the second and
706 third steps, the Hall voltage (V_H) is measured by applying positive and negative out-of-plane
707 magnetic fields ($|B| = 250 \text{ mT}$), respectively. V_H is measured between opposite probe contacts of the
708 HB for a current passing through the source and drain. The sheet electron density (n_{2D}) is calculated
709 using the formula $n_{2D} = \frac{n_{2D}^1 + n_{2D}^2}{2}$, with $n_{2D}^i = \frac{I_{\text{OSC,RMS}} \times B_i}{q \times V_H}$, where q is the fundamental charge, and B_i
710 is the magnitude of the applied out-of-plane magnetic field. The electron mobility (μ_n) is calculated
711 using the formula $\mu_n = \frac{\mu_n^1 + \mu_n^2}{2}$, with $\mu_n^i = \frac{1}{n_{2D}^i \times q \times R_{xx}}$.

712

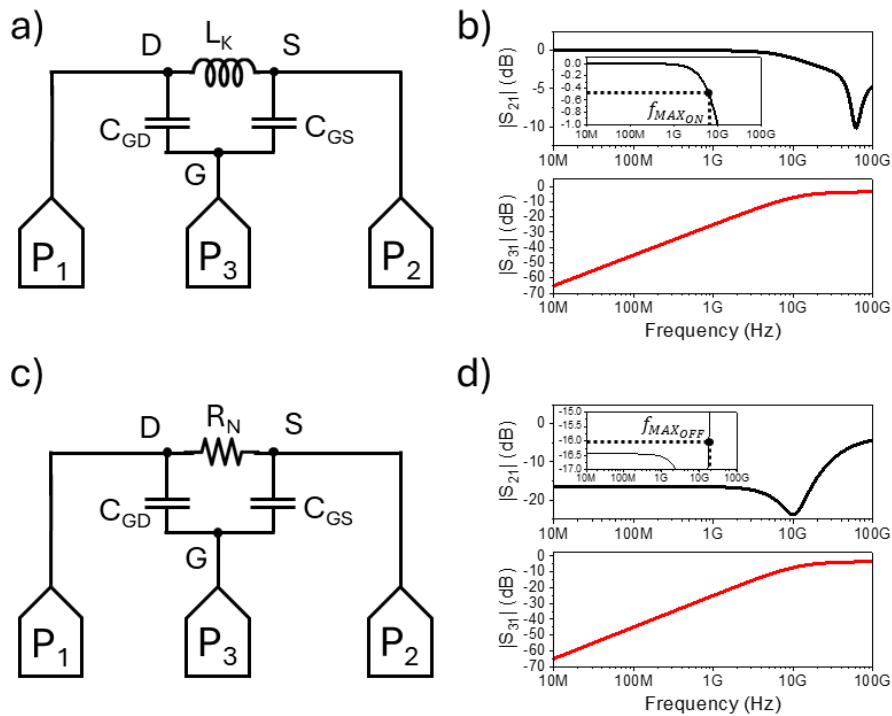
713

714

715 5. Estimation of the JoFET Maximum Operational Frequency

716 The JoFET acts as an inductor with value L_K and as a resistor with value R_N in the ON and OFF
717 state, respectively (see Figure 4b). The capacitors between gate and drain (C_{GD}) and gate and source
718 (C_{GS}) terminals represent the major parasitic elements for both the operating states.

719 Figure S19a reports the usage of the JoFET in the ON state where three simulation ports P_1 , P_2 , and
720 P_3 were involved as the V_{DS} source, R_L load, and V_{GS} source, respectively. Figure S19b shows the
721 frequency-resolved simulations of the transmission scattering parameter magnitudes $|S_{21}|$ and $|S_{31}|$.



722

723 **Figure S19: Theoretical frequency-dependent operating behavior of the JoFET.** a) Usage of
724 the JoFET in the ON state with three simulation ports involved. b) Frequency-resolved simulations
725 of the transmission scattering parameters of the JoFET in the ON state. c) Usage of the JoFET in the
726 OFF state with three simulation ports involved. d) Frequency-resolved simulations of the
727 transmission scattering parameters of the JoFET in the OFF state. a,c) The internal series resistance
728 of the three ports is 50 Ω . Circuitual simulations were computed with LTSpice XVII.
729

730 In the DC ON state, the parasitic capacitors act as open circuits so that the power provided by the
731 input port P_1 is totally provided to the port P_2 , thanks to the negligible impedance of the kinetic
732 inductance represented by the JoFET. In this case, an $|S_{21}| \sim 0$ dB (IL ~ 0 dB) is achieved. With the
733 increase of the operating frequency, the gate capacitors' impedance decreases, linking port P_1 with
734 the AC-grounded gate terminal represented by P_3 . As observed from Figure S19b, $|S_{31}|$ increases
735 with the frequency with the concomitant reduction of $|S_{21}|$. We defined the JoFET ON-state
736 maximum operational frequency (f_{MAXON}) as the frequency at which $|S_{21}|$ decrease of 10% (-0.46

737 dB) compared to its DC value. This is a crucial point from which the gate capacitance significantly
738 sinks the input power to the AC-grounded gate terminal, compared to that achieved at zero-
739 frequency. Based on the values reported in Table S2, $f_{MAX_{ON}} = 6 \text{ GHz}$ was retrieved from the
740 simulations.

741 **Figure S19c** reports the usage of the JoFET in the OFF state where three simulation ports P₁, P₂,
742 and P₃ were involved as the V_{DS} source, R_L load, and V_{GS} source, respectively. **Figure S19d** shows
743 the frequency-resolved simulations of the transmission scattering parameter magnitudes |S₂₁| and
744 |S₃₁|. Also in this case, at low-frequency the parasitic capacitors act as open circuits so that the
745 power provided by the input port P₁ is in large part reflected to the port itself due to the impedance
746 mismatch between R_N and the internal series resistance of P₁, namely 50 Ω. The remaining part
747 flows into the resistive branch reaching the load port P₂, consequently achieving |S₂₁| ~ - 16.5 dB
748 (IL ~ 16.5 dB). Increasing the operating frequency, the gate capacitors start to shunt R_N to both the
749 AC-grounded gate terminal represented by P₃ and the load resistance represented by P₂. As
750 observed from **Figure S19d**, |S₃₁| increases with frequency because of the impedance reduction of
751 the gate capacitors, finally shunting the resistive behavior of the JoFET. At the same time, |S₂₁| first
752 decreases due to the sink from the gate terminal, then increases from the R_N shunt reducing the
753 input-to-output isolation of the JoFET. We defined the JoFET OFF-state maximum operational
754 frequency ($f_{MAX_{OFF}}$) as the frequency at which |S₂₁| increase of 10% (+0.41 dB) compared to the
755 DC value. This is a crucial point from which the gate capacitance significantly shunts the resistive
756 behavior of the JoFET, compared to that achieved at zero-frequency. Based on the values reported
757 in Table S2, $f_{MAX_{OFF}} = 17 \text{ GHz}$ was retrieved from the simulations. The overall maximum
758 operating frequency (f_{MAX}) of the JoFET can be expressed as $\min(f_{MAX_{ON}}, f_{MAX_{OFF}})$, resulting in
759 $f_{MAX} = f_{MAX_{ON}} = 6 \text{ GHz}$.

760

761

762

763

764

765

766

767

768

769

770

771

772

773 **6. Estimation of the Static Power Dissipation**

774 The static power dissipation (P_{STAT}) of a JoFET, which is the power dissipated with no switching
 775 activities, is expressed as:

$$776 \quad (1) P_{STAT} = Re\{Z_{DS}(f)\} \times I_{DS_{RMS}}^2$$

777 where $Re\{Z_{DS}(f)\}$ is the real part of the drain-to-source impedance at the frequency f , $I_{DS_{RMS}} =$

778 $\sqrt{\frac{1}{T} \int_0^T |i_{DS}(t)|^2 dt}$ is the RMS value of I_{DS} , and $T = \frac{1}{f}$ is the signal period. In the DC case, equation 1

779 can be rewritten as the most popular formula:

$$780 \quad (2) P_{STAT} = R \times I^2$$

781 where R is the DC drain-to-source resistance, and I is the DC current.

782 P_{STAT} is equal to 0 W when the JoFET is in the non-dissipative ON state with $I_{DS} < I_S$ (Figure 4b

783 top), while $P_{STAT} = Re\{Z_{DS}(f)\} \times I_{DS_{RMS}}^2 = R_N \times I_{DS_{RMS}}^2$ when the JoFET is in the dissipative

784 OFF state (Figure 4b bottom). The reported OFF-state dissipation is valid until the JoFET

785 maximum operational frequency ($f_{MAX} \sim 700$ MHz), calculated as reported in Section 5: Estimation

786 of the JoFET Maximum Operational Frequency. Specifically, for $f > f_{MAX}$ the gate capacitance Z_{CG}

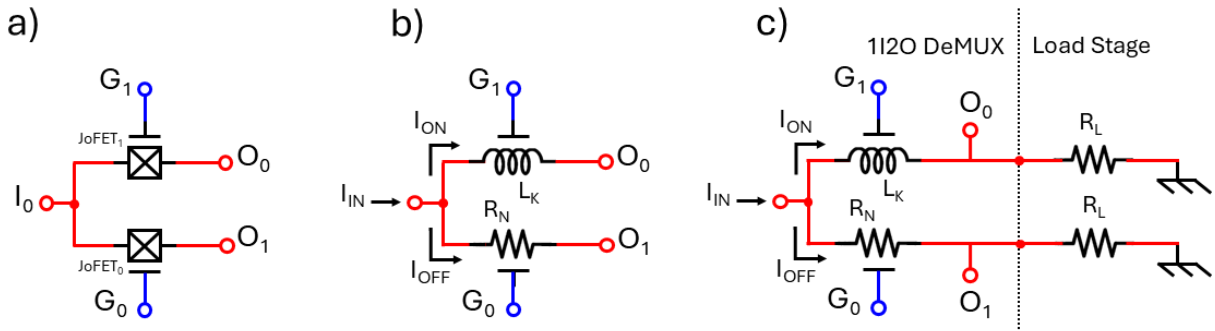
787 theoretically starts to shunt the resistive behavior of the JoFET in the OFF state, consequently

788 reducing the static power dissipated by the JoFET. In conclusion, P_{STAT} remains unchanged from

789 DC to f_{MAX} .

790 Figure S20a reports the representative case of study of a 1I2O superconducting demultiplexer (1I2O

791 DeMUX) featuring 2 JoFETs, the easiest case of study for proposed architecture.



792

793 **Figure S20: 1I2O superconducting demultiplexer architecture.** a) Generic architecture of a 1I2O

794 superconducting demultiplexer employing 2 JoFETs. b) Specific architecture of a 1I2O

795 superconducting demultiplexer with the JoFET₀ in the OFF state and JoFET₁ in the ON state. c)

796 Specific architecture of a 1I2O superconducting demultiplexer with a load stage.

797

798 Figure S20b depicts a specific operation of the proposed circuit with the JoFET₀ and JoFET₁ in

799 OFF and ON states, respectively. The reported lumped element equivalent circuit is valid for

800 $f < f_{MAX} \sim 700$ MHz, which is in the range of measurements of this work. Based on this assumption,
 801 P_{STAT} remains unchanged from DC to f_{MAX} . **Figure S20c** also reports the addition of the load stage
 802 with the load resistances R_L to the 1I2O superconducting demultiplexer. Under the previous
 803 conditions, the static power dissipated by the 1I2O DeMUX is related to the part of the input current
 804 (I_{IN}) flowing in the dissipative OFF branch (I_{OFF}), namely:

$$805 \quad (3) \quad I_{OFF_{RMS}} = I_{IN_{RMS}} \times \frac{R_L}{R_N + 2R_L}.$$

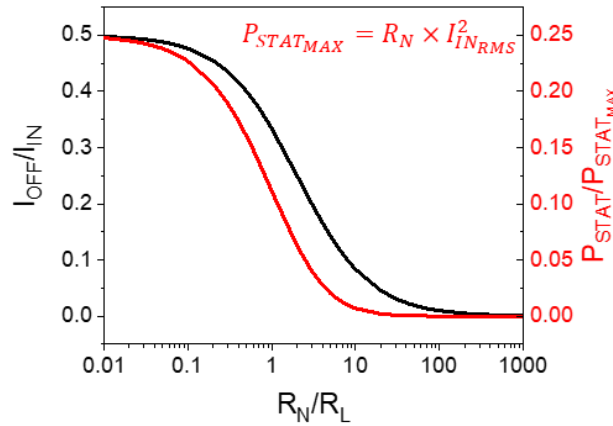
806 Consequently:

$$807 \quad (4) \quad P_{STAT} = R_N \times I_{OFF_{RMS}}^2 = R_N I_{IN_{RMS}}^2 \times \left(\frac{R_L}{R_N + 2R_L} \right)^2.$$

808 We defined $P_{STAT_{MAX}} = R_N I_{IN_{RMS}}^2$ as the maximum static power which can be dissipated in the
 809 resistive OFF branch. By defining a new variable $\alpha = \frac{R_N}{R_L}$, equation 4 becomes:

$$810 \quad (5) \quad \frac{P_{STAT}}{P_{STAT_{MAX}}} = \left(\frac{1}{\alpha + 2} \right)^2$$

811 **Figure S21** reports the I_{OFF}/I_{IN} ratio as well as the static power dissipated normalized to $P_{STAT_{MAX}}$ as
 812 a function of α .



813
 814 **Figure S21. I_{OFF}/I_{IN} and $P_{STAT}/P_{STAT_{MAX}}$ as a function of R_N/R_L .**

815 The higher the R_N/R_L ratio, the lower the current flowing through the resistive OFF branch, and
 816 consequently the lower the static power dissipated. When $R_N \ll R_L$, there is no impact of the
 817 JoFET's state on the supercurrent division so that the input current is perfectly divided into the two
 818 branches with a $P_{STAT}/P_{STAT_{MAX}} = 0.25$. In a different way, when $R_N = R_L$, the input supercurrent
 819 flowing in the dissipative branch is $I_0/3$, with $P_{STAT}/P_{STAT_{MAX}} = 0.1$. Eventually, when $R_N \gg R_L$,
 820 the input supercurrent flows only in the non-dissipative branch with $P_{STAT}/P_{STAT_{MAX}} \sim 0$.

821 Referring to the case of study of:

- 822 • **Figure 5a**, where $R_L = 200 \Omega$, $R_N \sim 500 \Omega$, and $I_{IN} = 1.3 \mu A$, we achieved $P_{STAT}/$
 823 $P_{STAT_{MAX}} \sim 0.05$ with $P_{STAT} \sim 40$ pW in the range 0-to-700 MHz;

824 • **Figure 5c**, where $R_L = 50 \Omega$, $R_N \sim 500 \Omega$, and $I_{IN} = 400 \text{ nA}_{\text{rms}}$, we achieved
825 $P_{STAT}/P_{STAT_{MAX}} \sim 0.007$ with $P_{STAT} \sim 700 \text{ fW}$ in the range 0-to-700 MHz.

826 **7. Estimation of the Dynamic Power Dissipation**

827 The dynamic power dissipation (P_{DYN}) of a FET is expressed as:

$$828 \quad (6) P_{DYN} = C_{eff} \times V_{DD}^2 \times f_{SW}$$

829 where C_{eff} is the sum of the load and parasitic capacitances of the FET, V_{DD} is the supply voltage,
830 and f_{SW} is the switching frequency.

831 For a JoFET, we consider the gate capacitance $C_G = C_{GS} + C_{GD}$ (**Figure 4b**) as the main capacitive
832 element in the evaluation of C_{eff} , as well as V_{DD} equals to the absolute maximum gate voltage
833 applied (V_{GS}). Based on this hypothesis, equation 6 can be written as:

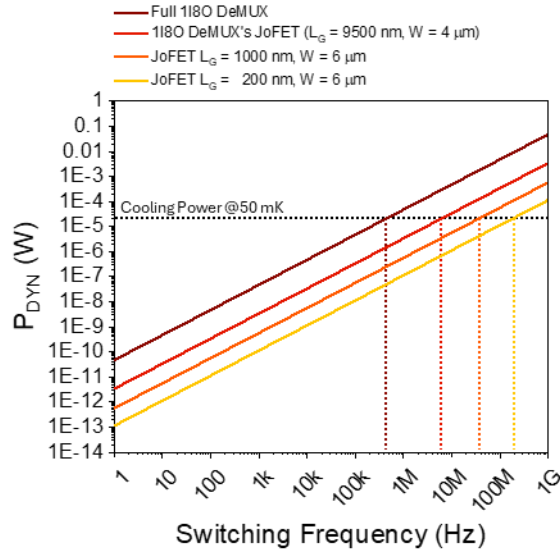
$$834 \quad (7) P_{DYN} = C_G \times V_{GS}^2 \times f_{SW}$$

835 In this context, since both conventional FETs and JoFETs feature charge/discharge of the gate
836 metal-oxide-semiconductor capacitor as the core of the switching activity, no significant
837 improvements are related to the use of superconducting leads instead of conventional metals in
838 reduction of the overall dynamic power dissipation. The improvement of the JoFET compared to
839 the FET can be achieved in “where” the dynamic power is dissipated. Under certain operating
840 conditions, the JoFET and the full chip can be in a non-dissipative state so that the dissipation of the
841 dynamic power happens out from the die. This is a possible gain in using JoFET compared to FET
842 to achieve negligible on-chip dynamic power dissipation and to move the dissipation of power away
843 from the coldest plate.

844 When n JoFETs are taken into account, P_{DYN} can be calculated as:

$$845 \quad (8) P_{DYN} = n \times C_G \times V_{GS}^2 \times f_{SW}$$

846 **Figure S22** reports P_{DYN} estimated for the fabricated JoFETs and the 1I8O superconducting
847 demultiplexer.



848

849 **Figure S22: Dynamic power dissipation vs. frequency of the fabricated JoFETs and the 1180**
 850 **superconducting demultiplexer.**

851 The black dashed line represents the cooling power of the cryostat we used throughout the
 852 experiments at a temperature of 50 mK, namely 16 mW. In the following, we have considered the
 853 full dissipation of P_{DYN} at the coldest plate as worst-case scenario. The red solid line is the dynamic
 854 power dissipated by the typical JoFET integrated in the superconducting 1180 demultiplexer ($L_G =$
 855 9500 nm , $W_{JJ} = 4 \text{ mm}$), while the brown solid line is the dynamic power dissipation of the entire
 856 chip ($n = 14$ JoFETs). The full demultiplexer die can operate until 400 kHz without affecting the
 857 temperature of the coldest plate, while the single JoFET can operate until 6 MHz. From equation 7,
 858 it is immediately apparent that the dynamic power dissipation of the JoFET can be reduced by
 859 reducing both the gate capacitance and the gate voltage. By reducing the size of the JoFET,
 860 consequently reducing the $W_{JJ} \times L_{JJ}$ area and the gate capacitance, the dynamic power dissipation
 861 decreases as reported for the orange and yellow solid lines, where JoFETs with $L_G = 1000 \text{ nm} / W_{JJ}$
 862 $= 6 \text{ mm}$ and $L_G = 200 \text{ nm} / W_{JJ} = 6 \text{ mm}$ were reported, respectively. Along the same path, the
 863 reduction of the gate voltage necessary to switch OFF the JoFET can quadratically reduce the
 864 dynamic power requirements.

865

866

867

868

869

870

871

872

873
874
875
876
877
878
879
880
881
882
883
884
885
886
887
888
889
890
891
892
893
894
895
896
897
898
899
900
901
902
903
904
905

8. Envisioning of Superconducting Time Division Multiplexing of Transmon Qubits

Superconducting Time Division Multiplexing (TDM) can be performed to read and control a specific transmon qubit of the Quantum Processing Unit (QPU) to reduce the number of cables required for the Quantum Computer (QC). In a transmon, microwave pulses are applied to the qubit drive line to modify the state of the transmon itself. A flux bias line is used to dynamically tune the operating frequency of the transmon. The recognition of the transmon's state, e.g., ground or excited state, can be performed via microwave transmission measurements made between the two readout ports. In this context, TDM can be applied to:

1. Perform microwave transmission measurements to a specific read-out line.
2. Route the non-dissipative supercurrent to a specific qubit flux bias line.
3. Route the microwave control pulses to a specific qubit drive line.

Usually, Frequency Division Multiplexing (FDM) of the operating frequencies of a series of transmons present on the same superconducting read-out line was applied to reduce the number of read-out cables. Each transmon operates at a specific frequency so that a selective read-out can be performed by FDM. This technique is the standard way used to increase the transmon integration in a QC. Superconducting TDM of several superconducting read-out lines embedding building blocks with arrays of qubits operating at the same frequencies represents a promising way to scale-up superconducting QCs.

At the same time, each transmon is provided with a superconducting flux bias line used to tune its operating frequency. Superconducting TDM promises to reduce the number of flux bias lines linked to the 300 K-located electronics.

906 Eventually, the superconducting TDM of control pulses to a specific qubit drive line can drastically
 907 reduce the number of control cables linked to the 300 K-located electronics. Unlike the previous
 908 applications, where a superconducting non-dissipative line is driven by the superconducting
 909 demultiplexer, in this case TDM signals need to be routed to high-impedance capacitive loads
 910 represented by the control ports of the transmons, from which a desired ON/OFF ratio is required.
 911 In conclusion, superconducting TDM of transmons requires a superconducting demultiplexer able
 912 to:

- 913 • Operates at a temperature of 50 mK.
- 914 • Operates with a signal frequency in the 4÷8 GHz range.
- 915 • Operates with control switching signals in the qubit coherence time range to run quantum
 916 algorithms (from a few ns to a few ms).
- 917 • Exhibits an ON-state insertion loss of 0 dB to preserve static power dissipation.
- 918 • Exhibits an ON/OFF ratio of 30÷40 dBs to route the control signal to the desired qubit.

919
 920 To date, the proposed superconducting demultiplexers can operate at the mixing chamber base
 921 temperature of 50 mK with a suitable frequency operating range, but an increased port-to-port
 922 isolation and a reduced switching time need to be reached to perform TDM with transmon qubits.
 923 The reduced ON/OFF ratio of the fabricated chip is related to the ability of the InAsOI-based JoFET
 924 to reach a high normal state resistance value when gated in the OFF state. The reduced normal state
 925 resistance increase is related to the poor ability in depleting the InAs epilayer from charge carriers
 926 applying negative gate voltages. To overpass this limit, engineering the InAsOI platform to improve
 927 the gate tunable electrical properties is mandatory. As a walk-around of the InAsOI-related poor
 928 gate-tunable performance, JoFETs embedding n ($n>1$) Josephson Junctions (JJs) can be
 929 manufactured to reach a higher JoFET's ON/OFF ratio. This allows to reach a normal state
 930 resistance in the OFF state n times higher than that of the JoFET with a single JJ.
 931 **Table S4** reports the specs required for TDM of superconducting transmon qubits ² and the
 932 performance achieved by the proposed superconducting demultiplexer and achievable in the near
 933 future by improving the JoFET and the entire chip.

934
 935 **Table S4. Specs required for TDM of superconducting transmon qubits ² and performance**
 936 **achieved by the proposed superconducting demultiplexer and achievable in the near future by**
 937 **improving the JoFET and the entire chip.**

Specs	Required Value ²	Achieved With This Work	Achievable With a Proper Design
-------	-----------------------------	-------------------------	---------------------------------

<i>Operating Temperature</i>	50 mK and lower	50 mK and lower	50 mK and lower
<i>Maximum Full Power Consumption</i>	<20 mW for the entire chip	Static Power Consumption for the single JoFET: 700 fW Dynamic Power Consumption for the single JoFET: 20 mW @ 5 MHz	Static Power Consumption for the single JoFET: 100 fW Dynamic Power Consumption for the single JoFET: 20 mW @ 200 MHz
<i>Frequency Operating Range</i>	4÷8 GHz	4 GHz	4÷8 GHz
<i>Input Signal Dynamic Range</i>	-60÷-120 dBm	< -70 dBm	< -60 dBm
<i>Switching Time</i>	1 ns	100 ns	1 ns
<i>Port-to-Port Isolation</i>	>30 dB	17.5 dB	30 dB

938

939

940

941

References

- 942 [1] H. Takayanagi, J.B. Hansen, J. Nitta, Localization Effects on the Critical Current of a
943 Superconductor—Normal-Metal—Superconductor Junction, *Phys. Rev. Lett.* 74 (1995) 162–
944 165. <https://doi.org/10.1103/PhysRevLett.74.162>.
- 945 [2] A. Chrestin, R. Kürsten, K. Biedermann, T. Matsuyama, U. Merkt,
946 Superconductor/semiconductor nanostructures on p-type InAs, *Superlattices Microstruct.* 25
947 (1999) 711–720. <https://doi.org/10.1006/spmi.1999.0719>.
- 948 [3] T. Akazaki, J. Nitta, H. Takayanagi, K. Arai, Superconducting junctions using a 2DEG in a
949 strained InAs quantum well inserted into an InAlAs/InGaAs MD structure, *IEEE Trans.*
950 *Applied Supercond.* 5 (1995) 2887–2891. <https://doi.org/10.1109/77.403195>.
- 951 [4] H. Takayanagi, T. Akazaki, J. Nitta, T. Enoki, Superconducting Three-Terminal Devices
952 Using an InAs-Based Two-Dimensional Electron Gas, *Jpn. J. Appl. Phys.* 34 (1995) 1391.
953 <https://doi.org/10.1143/JJAP.34.1391>.
- 954 [5] H. Takayanagi, T.A. Tatsushi Akazaki, Submicron Gate-Fitted Superconducting Junction
955 Using a Two-Dimensional Electron Gas, *Jpn. J. Appl. Phys.* 34 (1995) 6977.
956 <https://doi.org/10.1143/JJAP.34.6977>.
- 957 [6] T. Akazaki, H. Takayanagi, J. Nitta, T. Enoki, A Josephson field effect transistor using an
958 InAs-inserted-channel In_{0.52}Al_{0.48}As/In_{0.53}Ga_{0.47}As inverted modulation-doped
959 structure, *Appl. Phys. Lett.* 68 (1996) 418–420. <https://doi.org/10.1063/1.116704>.
- 960 [7] T. Akazaki, J. Nitta, H. Takayanagi, T. Enoki, Superconducting transistors using InAs-
961 inserted-channel InAlAs/InGaAs inverted HEMTs, *Supercond. Sci. Technol.* 9 (1996) A83–
962 A86. <https://doi.org/10.1088/0953-2048/9/4A/022>.
- 963 [8] A. Richter, M. Koch, T. Matsuyama, U. Merkt, Transport properties of Nb/InAs(2DEG)/Nb
964 Josephson field-effect transistors, *Supercond. Sci. Technol.* 12 (1999) 874–876.
965 <https://doi.org/10.1088/0953-2048/12/11/354>.

- 966 [9] A. Richter, P. Baars, U. Merkt, Supercurrents in two-dimensional electron systems, *Phys. E*
 967 *Low-Dimensional Syst. Nanostructures*. 12 (2002) 911–917. [https://doi.org/10.1016/S1386-](https://doi.org/10.1016/S1386-9477(01)00408-8)
 968 [9477\(01\)00408-8](https://doi.org/10.1016/S1386-9477(01)00408-8).
- 969 [10] J. Shabani, M. Kjaergaard, H.J. Suominen, Y. Kim, F. Nichele, K. Pakrouski, T. Stankevic,
 970 R.M. Lutchyn, P. Krogstrup, R. Feidenhans'l, S. Kraemer, C. Nayak, M. Troyer, C.M.
 971 Marcus, C.J. Palmstrøm, Two-dimensional epitaxial superconductor-semiconductor
 972 heterostructures: A platform for topological superconducting networks, *Phys. Rev. B*. 93
 973 (2016) 155402. <https://doi.org/10.1103/PhysRevB.93.155402>.
- 974 [11] M. Kjaergaard, H.J. Suominen, M.P. Nowak, A.R. Akhmerov, J. Shabani, C.J. Palmstrøm, F.
 975 Nichele, C.M. Marcus, Transparent Semiconductor-Superconductor Interface and Induced
 976 Gap in an Epitaxial Heterostructure Josephson Junction, *Phys. Rev. Appl.* 7 (2017) 034029.
 977 <https://doi.org/10.1103/PhysRevApplied.7.034029>.
- 978 [12] W. Mayer, J. Yuan, K.S. Wickramasinghe, T. Nguyen, M.C. Dartiailh, J. Shabani,
 979 Superconducting proximity effect in epitaxial Al-InAs heterostructures, *Appl. Phys. Lett.* 114
 980 (2019). <https://doi.org/10.1063/1.5067363>.
- 981 [13] J.S. Lee, B. Shojaei, M. Pendharkar, A.P. McFadden, Y. Kim, H.J. Suominen, M.
 982 Kjaergaard, F. Nichele, H. Zhang, C.M. Marcus, C.J. Palmstrøm, Transport Studies of Epi-
 983 Al/InAs Two-Dimensional Electron Gas Systems for Required Building-Blocks in
 984 Topological Superconductor Networks, *Nano Lett.* 19 (2019) 3083–3090.
 985 <https://doi.org/10.1021/acs.nanolett.9b00494>.
- 986 [14] S. Guiducci, M. Carrega, G. Biasiol, L. Sorba, F. Beltram, S. Heun, Toward Quantum Hall
 987 Effect in a Josephson Junction, *Phys. Status Solidi – Rapid Res. Lett.* 13 (2019) 1–5.
 988 <https://doi.org/10.1002/pssr.201800222>.
- 989 [15] S. Guiducci, M. Carrega, F. Taddei, G. Biasiol, H. Courtois, F. Beltram, S. Heun, Full
 990 electrostatic control of quantum interference in an extended trenched Josephson junction,
 991 *Phys. Rev. B*. 99 (2019) 235419. <https://doi.org/10.1103/PhysRevB.99.235419>.
- 992 [16] F. Barati, J.P. Thompson, M.C. Dartiailh, K. Sardashti, W. Mayer, J. Yuan, K.
 993 Wickramasinghe, K. Watanabe, T. Taniguchi, H. Churchill, J. Shabani, Tuning Supercurrent
 994 in Josephson Field-Effect Transistors Using h-BN Dielectric, *Nano Lett.* 21 (2021) 1915–
 995 1920. <https://doi.org/10.1021/acs.nanolett.0c03183>.
- 996 [17] B.H. Elfeky, N. Lotfizadeh, W.F. Schiela, W.M. Strickland, M. Dartiailh, K. Sardashti, M.
 997 Hatefipour, P. Yu, N. Pankratova, H. Lee, V.E. Manucharyan, J. Shabani, Local Control of
 998 Supercurrent Density in Epitaxial Planar Josephson Junctions, *Nano Lett.* 21 (2021) 8274–
 999 8280. <https://doi.org/10.1021/acs.nanolett.1c02771>.
- 1000 [18] F. Wen, J. Yuan, K.S. Wickramasinghe, W. Mayer, J. Shabani, E. Tutuc, Epitaxial Al-InAs
 1001 Heterostructures as Platform for Josephson Junction Field-Effect Transistor Logic Devices,
 1002 *IEEE Trans. Electron Devices*. 68 (2021) 1524–1529.
 1003 <https://doi.org/10.1109/TED.2021.3057790>.
- 1004 [19] A. Hertel, L.O. Andersen, D.M.T. van Zanten, M. Eichinger, P. Scarlino, S. Yadav, J.
 1005 Karthik, S. Gronin, G.C. Gardner, M.J. Manfra, C.M. Marcus, K.D. Petersson, Electrical
 1006 Properties of Selective-Area-Grown Superconductor-Semiconductor Hybrid Structures on
 1007 Silicon, *Phys. Rev. Appl.* 16 (2021) 044015.
 1008 <https://doi.org/10.1103/PhysRevApplied.16.044015>.
- 1009 [20] M. Sütő, T. Prok, P. Makk, M. Kirti, G. Biasiol, S. Csonka, E. Tóvári, Near-surface InAs

- 1010 two-dimensional electron gas on a GaAs substrate: Characterization and superconducting
1011 proximity effect, *Phys. Rev. B.* 106 (2022) 235404.
1012 <https://doi.org/10.1103/PhysRevB.106.235404>.
- 1013 [21] C. Ciaccia, R. Haller, A.C.C. Drachmann, T. Lindemann, M.J. Manfra, C. Schrade, C.
1014 Schönenberger, Gate-tunable Josephson diode in proximitized InAs supercurrent
1015 interferometers, *Phys. Rev. Res.* 5 (2023) 033131.
1016 <https://doi.org/10.1103/PhysRevResearch.5.033131>.
- 1017 [22] M. Coraiola, A.E. Svetogorov, D.Z. Haxell, D. Sabonis, M. Hinderling, S.C. ten Kate, E.
1018 Cheah, F. Krizek, R. Schott, W. Wegscheider, J.C. Cuevas, W. Belzig, F. Nichele, Flux-
1019 Tunable Josephson Diode Effect in a Hybrid Four-Terminal Josephson Junction, *ACS Nano.*
1020 18 (2024) 9221–9231. <https://doi.org/10.1021/acsnano.4c01642>.
- 1021 [23] S. Yan, H. Su, D. Pan, W. Li, Z. Lyu, M. Chen, X. Wu, L. Lu, J. Zhao, J.-Y. Wang, H. Xu,
1022 Supercurrent, Multiple Andreev Reflections and Shapiro Steps in InAs Nanosheet Josephson
1023 Junctions, *Nano Lett.* 23 (2023) 6497–6503. <https://doi.org/10.1021/acs.nanolett.3c01450>.
- 1024 [24] Y.-J. Doh, J.A. van Dam, A.L. Roest, E.P.A.M. Bakkers, L.P. Kouwenhoven, S. De
1025 Franceschi, Tunable Supercurrent Through Semiconductor Nanowires, *Science* (80-.). 309
1026 (2005) 272–275. <https://doi.org/10.1126/science.1113523>.
- 1027 [25] H.Y. Günel, I.E. Batov, H. Hardtdegen, K. Sladek, A. Winden, K. Weis, G. Panaitov, D.
1028 Grützmacher, T. Schäpers, Supercurrent in Nb/InAs-nanowire/Nb Josephson junctions, *J.*
1029 *Appl. Phys.* 112 (2012). <https://doi.org/10.1063/1.4745024>.
- 1030 [26] P. Perla, H.A. Fonseca, P. Zellekens, R. Deacon, Y. Han, J. Kölzer, T. Mörstedt, B.
1031 Bennemann, A. Espiari, K. Ishibashi, D. Grützmacher, A.M. Sanchez, M.I. Lepsa, T.
1032 Schäpers, Fully in situ Nb/InAs-nanowire Josephson junctions by selective-area growth and
1033 shadow evaporation, *Nanoscale Adv.* 3 (2021) 1413–1421.
1034 <https://doi.org/10.1039/D0NA00999G>.
- 1035 [27] A. Goswami, S.R. Mudi, C. Dempsey, P. Zhang, H. Wu, B. Zhang, W.J. Mitchell, J.S. Lee,
1036 S.M. Frolov, C.J. Palmström, Sn/InAs Josephson Junctions on Selective Area Grown
1037 Nanowires with in Situ Shadowed Superconductor Evaporation, *Nano Lett.* 23 (2023) 7311–
1038 7318. <https://doi.org/10.1021/acs.nanolett.3c01320>.
- 1039 [28] N.W. Hendrickx, M.L. V. Tagliaferri, M. Kouwenhoven, R. Li, D.P. Franke, A. Sammak, A.
1040 Brinkman, G. Scappucci, M. Veldhorst, Ballistic supercurrent discretization and micrometer-
1041 long Josephson coupling in germanium, *Phys. Rev. B.* 99 (2019) 075435.
1042 <https://doi.org/10.1103/PhysRevB.99.075435>.
- 1043 [29] F. Vigneau, R. Mizokuchi, D.C. Zanuz, X. Huang, S. Tan, R. Maurand, S. Frolov, A.
1044 Sammak, G. Scappucci, F. Lefloch, S. De Franceschi, Germanium Quantum-Well Josephson
1045 Field-Effect Transistors and Interferometers, *Nano Lett.* 19 (2019) 1023–1027.
1046 <https://doi.org/10.1021/acs.nanolett.8b04275>.
- 1047 [30] K. Aggarwal, A. Hofmann, D. Jirovec, I. Prieto, A. Sammak, M. Botifoll, S. Martí-Sánchez,
1048 M. Veldhorst, J. Arbiol, G. Scappucci, J. Danon, G. Katsaros, Enhancement of proximity-
1049 induced superconductivity in a planar Ge hole gas, *Phys. Rev. Res.* 3 (2021) L022005.
1050 <https://doi.org/10.1103/PhysRevResearch.3.L022005>.
- 1051 [31] A. Tosato, V. Levajac, J.-Y. Wang, C.J. Boor, F. Borsoi, M. Botifoll, C.N. Borja, S. Martí-
1052 Sánchez, J. Arbiol, A. Sammak, M. Veldhorst, G. Scappucci, Hard superconducting gap in
1053 germanium, *Commun. Mater.* 4 (2023) 23. <https://doi.org/10.1038/s43246-023-00351-w>.

- 1054 [32] M. Hinderling, S.C. ten Kate, M. Coraiola, D.Z. Haxell, M. Stiefel, M. Mergenthaler, S.
 1055 Paredes, S.W. Bedell, D. Sabonis, F. Nichele, Direct Microwave Spectroscopy of Andreev
 1056 Bound States in Planar Ge Josephson Junctions, *PRX Quantum*. 5 (2024) 030357.
 1057 <https://doi.org/10.1103/PRXQuantum.5.030357>.
- 1058 [33] L. Lakic, W.I.L. Lawrie, D. van Driel, L.E.A. Stehouwer, Y. Su, M. Veldhorst, G. Scappucci,
 1059 F. Kuemmeth, A. Chatterjee, A quantum dot in germanium proximitized by a
 1060 superconductor, *Nat. Mater.* 24 (2025) 552–558. [https://doi.org/10.1038/s41563-024-02095-](https://doi.org/10.1038/s41563-024-02095-5)
 1061 [5](https://doi.org/10.1038/s41563-024-02095-5).
- 1062 [34] M. Zhu, M. Ben Shalom, A. Mishchenko, V. Fal’ko, K. Novoselov, A. Geim, Supercurrent
 1063 and multiple Andreev reflections in micrometer-long ballistic graphene Josephson junctions,
 1064 *Nanoscale*. 10 (2018) 3020–3025. <https://doi.org/10.1039/C7NR05904C>.
- 1065 [35] T. Li, J.C. Gallop, L. Hao, E.J. Romans, Scalable, Tunable Josephson Junctions and DC
 1066 SQUIDS Based on CVD Graphene, *IEEE Trans. Appl. Supercond.* 29 (2019) 1–4.
 1067 <https://doi.org/10.1109/TASC.2019.2897999>.
- 1068 [36] A.A. Generalov, K.L. Viisanen, J. Senior, B.R. Ferreira, J. Ma, M. Möttönen, M. Prunnila,
 1069 H. Bohuslavskyi, Wafer-scale CMOS-compatible graphene Josephson field-effect transistors,
 1070 *Appl. Phys. Lett.* 125 (2024). <https://doi.org/10.1063/5.0203515>.
- 1071 [37] G. De Simoni, F. Paolucci, P. Solinas, E. Strambini, F. Giazotto, Metallic supercurrent field-
 1072 effect transistor, *Nat. Nanotechnol.* 13 (2018) 802–805. [https://doi.org/10.1038/s41565-018-](https://doi.org/10.1038/s41565-018-0190-3)
 1073 [0190-3](https://doi.org/10.1038/s41565-018-0190-3).
- 1074 [38] G. De Simoni, C. Puglia, F. Giazotto, Niobium Dayem nano-bridge Josephson gate-
 1075 controlled transistors, *Appl. Phys. Lett.* 116 (2020). <https://doi.org/10.1063/5.0011304>.
- 1076 [39] C. Puglia, G. De Simoni, N. Ligato, F. Giazotto, Vanadium gate-controlled Josephson half-
 1077 wave nanorectifier, *Appl. Phys. Lett.* 116 (2020). <https://doi.org/10.1063/5.0013512>.
- 1078 [40] O. Arif, L. Canal, E. Ferrari, C. Ferrari, L. Lazzarini, L. Nasi, A. Paghi, S. Heun, L. Sorba,
 1079 Influence of an Overshoot Layer on the Morphological, Structural, Strain, and Transport
 1080 Properties of InAs Quantum Wells, *Nanomaterials*. 14 (2024) 592.
 1081 <https://doi.org/10.3390/nano14070592>.
- 1082 [41] A. Paghi, S. Battisti, S. Tortorella, G. De Simoni, F. Giazotto, Cryogenic Behavior of High-
 1083 Permittivity Gate Dielectrics: The Impact of the Atomic Layer Deposition Temperature and
 1084 the Lithography Patterning Method, Prepr. [Http//Arxiv.Org/Abs/2407.04501](http://Arxiv.Org/Abs/2407.04501). (2024).
 1085 <http://arxiv.org/abs/2407.04501>.
- 1086 [42] R. Acharya, S. Brebels, A. Grill, J. Verjauw, T. Ivanov, D.P. Lozano, D. Wan, J. Van
 1087 Damme, A.M. Vadiraj, M. Mongillo, B. Govoreanu, J. Craninckx, I.P. Radu, K. De Greve,
 1088 G. Gielen, F. Catthoor, A. Potočnik, Multiplexed superconducting qubit control at millikelvin
 1089 temperatures with a low-power cryo-CMOS multiplexer, *Nat. Electron.* 6 (2023) 900–909.
 1090 <https://doi.org/10.1038/s41928-023-01033-8>.

1091

1092